The influence of transition metal addition on lithium stabilized Na-β″-alumina electrolytes

Dissertation

Zur Erlangung des akademischen Grades doctor rerum naturalium

(Dr. rer. nat.)

vorgelegt dem Rat der Chemisch-Geowissenschaftlichen Fakultät der

Friedrich-Schiller-Universität Jena

von M. Sc. Cornelius Leopold Dirksen

Geboren am 14.06.1993 in Ingolstadt

Gutachter:

1. Prof. Dr. Michael Stelter, Friedrich-Schiller-Universität Jena
2. Prof. Dr. Phillipp Adelhelm, Humboldt-Universität Berlin

Tag der Verteidigung: 03.05.2023

Danksagung

Mein besonderer Dank gilt Prof. Dr. Michael Stelter, Dr. Matthias Schulz und Dr. Karl Skadell, die mir als Hochschul- beziehungsweise Fachbetreuer die Promotion an der Friedrich-Schiller-Universität in Zusammenarbeit mit dem Fraunhofer IKTS ermöglicht haben und mich durch die Zeit der Promotion begleiteten.

Mein Dank gilt auch allen anderen Mitarbeiten des Fraunhofer IKTS und insbesondere der OE 454: Artur, Carsten, Hagen, Hannes, Heidi, Karl, Lutz, Martin B., Martin G., Martin H., Matthias, Micha, Roland, Ronny und Timmy die mir ebenfalls immer zur Seite standen und stets für ein tolles Arbeitsklima sorgten. Außerdem möchte ich mich bei Detlef Rohländer und Anja Harpf für zahlreiche Messungen und deren Einordnung bedanken.

Bei Prof. Adelhelm möchte ich mich herzlich für die Anfertigung des Zweitgutachtens bedanken.

Bei der Arbeitsgruppe von Dirk Enke an der Universität Leipzig und insbesondere bei Antonia möchte ich mich für die erfolgreiche Zusammenarbeit in den letzten drei Jahren bedanken.

Zuletzt möchte ich mich bei meinen Freunden, meinen Eltern Elisabeth und Martin, meinen Großeltern Christa und Poldi, meiner Schwester Lydia und bei meiner weiteren Verwandtschaft bedanken, die mich alle stets in jeder Hinsicht unterstützen.

Table of Contents

Table of Contents

List of Abbreviations

AMTEC   Alkali-metal thermal to electric converter

DFT   Discrete *Fourier* transformation

DSC   Differential scanning calorimetry

DTA   Differential thermal analysis

EBSD   Electron backscatter diffraction

E.g.   Exempli gratia

EPR   Electron paramagnetic resonance

Etc.   Et Cetera

IKTS   Institute for Ceramic Technologies

NAS   Sodium-sulfur battery

NASICON   Na super ionic conductor

NiMH   Nickel-metal hydride battery

NMR   Nuclear magnetic resonance

m.p.   Melting point

EDX   Energy-dispersive X-ray spectroscopy

LIB   Lithium-ion battery

PC   *Peukert* constant

PDF   Powder diffraction file

PEIS   Potentiostatic electrochemical impedance spectroscopy

SEM   Scanning electron microscopy

SoC   State of charge

VPC   Vapor phase conversion

XPS   X-ray photoelectron spectroscopy

List of Abbreviations

XRD   X-ray diffraction

ZEBRA   Zero Emission Battery Research Activities

List of Symbols

Symbol	Unit / Value	Meaning
A	-	Pre-exponential factor
A_{cs}	cm²	Cross-sectional area
C	mAh	Capacity
d	cm	Diameter
E_a	eV	Activation energy
I	A	Current
l	cm	Length
k_B	eV K^{-1}	Boltzmann's constant
m	g	Mass
M	g mol^{-1}	Molar mass
n	n	Mole
R	Ohm	Ohmic resistance
R_b	Ohm	Bulk resistance
R_{gb}	Ohm	Grain boundary resistance
P	%	Porosity
t	° C	Temperature
T	K	Temperature
th	cm	Thickness
V	cm³	Volume
V_P	cm³ g^{-1}	Pore volume
ρ	g cm^{-3}	Volumetric mass density
σ	S cm^{-1}	Conductivity

List of Symbols

σ_s	MPa	Fracture strength
σ_0	MPa	Characteristic fracture strength
ω	-	Mass fraction
χ	-	Mole fraction

1. Introduction and Objectives

1.1 Introduction

Volatile sources of electric power such as solar and wind power are the backbone of the trajectory to a carbon-neutral energy supply. A very significant challenge for using such volatile power sources is the storage of electrical energy. This storage is necessary because of the temporal mismatches of electricity production and consumption inevitable with volatile power sources. These mismatches can last seconds, hours or even days. [1–3] It is only possible to overcome long-lasting shortfalls in power generation, such as periods when neither wind nor solar generation is possible [Dunkelflaute], by technologies like thermal or chemical energy storage such as power from gas. Shorter imbalances can be peak shaved, valley filled, or frequency regulated by electrochemical batteries. [4–6] The electrochemical batteries used for this purpose are frequently Lithium-ion batteries (LIBs) but, in addition, sodium-based batteries, such as NAS® and Na/NiCl$_2$-batteries (also known as ZEBRA Battery), are already used on an industrial scale. [7–9] Neither of the sodium-based cell systems requires critical resources such as cobalt or lithium and are, therefore, promising candidates for the central pillar of domestic and industrial battery storage systems. An application in the automotive sector is less attractive since both systems operate at high temperatures of 250 °C to 300 °C. The core compound of both technologies - NAS® and the Na/NiCl$_2$ - is a sodium-ion conductive Na-β″-alumina solid electrolyte. This material class was first described in 1916 by *Rankin* and *Merwin*. [10] Fifty-one years later, *Weber* and *Kummer* [11] published the first concept of the NAS®-battery, while the first patent on Na/NiCl$_2$-batteries was obtained in 1978. [12] The novel battery concepts kick started research on ceramic Na-β″-alumina electrolytes in the following years. Production methods, the phase formation of Na-β″-alumina, and different applications have been thoroughly investigated. [13–24] The two main material characteristics of the focus of interest are the ionic conductivity and the characteristic fracture strength of the Na-β″-alumina electrolytes. A high ionic and negligible electronic conductivity are essential to guarantee high round trip efficiency and a sufficient cycling rate of the battery. The second parameter is critical because the brittle ceramic electrolytes have to withstand mechanical stresses from a pressure of several atmospheres while the cells are heating up or undergoing cycling. [25] A sufficient characteristic fracture strength enables the usage of thinner Na-β″-alumina electrolytes, so reducing the electrolyte resistance within a cell.

The ionic conductivity and the fracture strength are very sensitive to the manufacturing process. In particular, the sintering temperature and the dwell time required to obtain a dense structure significantly impact both material properties. By 3d transition metal doping, the sintering behavior and the coupled material properties can be adjusted [26–28], as further described in chapter 2.4.2. However, there is yet no similar and comprehensive study of different 3d transition metal dopants or clarification of the mechanism behind the improved ionic conductivity, characteristic fracture strength, and reduced sintering temperature. Therefore, I identified 3d transition metal doping of Na-β''-alumina electrolytes as a tool for increasing the performance of Na-β''alumina-based battery storage systems as well as reducing production costs and thereby improving their market position.

1.2   Objectives and strategy

This thesis aims to systematically investigate and clarify the mechanism and effects of 3d transition metal doping of Na-β″-alumina electrolytes. In addition, the functionality of such modified electrolyte materials is demonstrated in two application cases.

For this purpose, three dopants, namely TiO_2, Mn_3O_4, and NiO, were chosen from candidates identified from an extensive literature review. The selection criteria applied were a positive impact on the ionic conductivity and the characteristic fracture strength with simultaneous sintering temperature reduction. The influences of the dopants were investigated systematically by applying different doping amounts and sintering temperatures. To structure the fields of research, four main objectives and fulfillment strategies were identified:

1.) The first objective of this work was to gain knowledge about the doping mechanism of the different dopants. Methods like XRD (X-ray diffraction), EDX (Energy-dispersive X-ray spectroscopy), and DSC (Differential scanning calorimetry) were used to clarify whether the dopants are incorporated into the crystal lattice or if they form a secondary phase.

2.) The second objective was the characterization of microstructure dependency on dopant, doping level, and sintering temperature. The microstructure of Na-β″-alumina electrolytes strongly influences the ionic conductivity and characteristic fracture strength. SEM (Scanning electron microscopy) imaging was the primary characterization technique for fulfilling this objective.

3.) The sample matrix was analyzed to complete the third objective of finding the optimum combination of sintering temperature, dopant type, and doping amount for obtaining Na-β″-alumina electrolytes with the desired characteristics of high ionic conductivity and characteristic fracture strength.

4.) The final objective was to use transition metal doped Na-β″-alumina electrolytes in practical applications. I used two different cell setups to demonstrate the functionality and stability of the electrolytes:

- The first application was a $Na/NiCl_2$-cell and showed the possible improvements in cell resistance and round-trip efficiency by using doped Na-β″-alumina electrolytes. Furthermore, the mechanical, the chemical, and the electrochemical stability were demonstrated.

- The second application was to show the novel possibilities of doped Na-β″-alumina electrolytes based on a bilayer electrolyte with a porous support and a dense layer. The porous bulk provides mechanical strength and is infiltrated with the liquid and highly conductive salt $NaAlCl_4$, while the dense layer, made from doped Na-β″-alumina, prevents short circuits. A low sintering temperature was particularly important while producing the bilayer electrolytes in order to avoid a reduction of porosity within the porous support.

The characterization of Na-β″-alumina electrolytes doped with three different 3d transition metals provided comparable and comprehensive data on this field. I investigated the key characteristics of ionic conductivity and characteristic fracture strength of TiO_2, Mn_3O_4, and NiO doped Na-β″-alumina electrolytes at different doping amounts and sintering temperatures. In contrast to previous studies, various dopants, doping amounts, and sintering temperatures were tested. Density, SEM-EDX, and XRD studies have been carried out to investigate the mechanisms of 3d transition metal doping of Na-β″-alumina that, so far, have been poorly examined. And, again unlike in previous research, the most promising doped electrolyte was practically tested in a cell application.

2. Literature Overview

2.1   Fundamentals of Na-β″-alumina

Na-β″-alumina is one of several similar Na-ion conductive sodium polyaluminate crystal phases. These phases fall into two groups. One of these groups has the rhombohedral space group R$\bar{3}$m (Na-β″-alumina or Na-β″″-alumina). [19,29] The other group contains phases like Na-β-alumina or Na-β‴-alumina and is assigned to the hexagonal space group $P\,6_3/mmc$. [19,29] The crystal phase most frequently discussed and used in cell systems is Na-β″-alumina (Figure 1). Conduction slabs occupied by mobile Na-ions enable ionic conductivity. The slabs are separated by alternately close-packed oxide blocks with Al-ions in the octahedral and tetrahedral interstices. The blocks are linked to each other by bridging oxygen atoms.

The chemical composition of Na-β″-alumina electrolytes is not strictly stoichiometric and is often given as $(Na_2O) \cdot x\ Al_2O_3$ (5 < x < 7). [30–32] The variability is caused by different occupation ratios of Na-ions within the conduction slabs. [33] The number of Na-ions is influenced by the amount of sodium in the reactant mixture, and the temperature applied during synthesis. [33] High temperatures over a long period lead to increased sublimation of Na_2O (sublimation point 1275 °C [34]) and a reduced Na-content within the electrolyte. A high Na-content increases the ionic conductivity of Na-β″-alumina. [22,35,36] The sodium ions gather in the conduction slab, lowering the activation energy of Na^+-hopping, thereby enhancing the ionic conductivity. *Baffier et al.* [36] reported a lower activation energy (0.22 eV) for Na-ion rich Na-β″-alumina single crystals than in Na-ion poor crystals (0.17 eV).
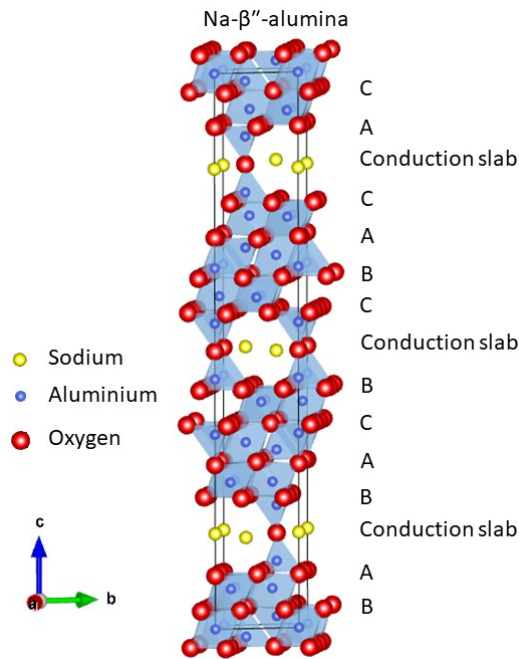
Figure 1. Idealized crystal structure of Na-β″-alumina. The figure is based on [37].

An idealized conduction slab with an occupation ratio of 1 is presented in Figure 2. Here, vacancies occurring in real crystals are not displayed. Within the slab, Na-ions can hop from one position to another; since the slab spreads in the ab-plain, the crystals are non-Na-ion-conductive in the c-direction (Figure 1).
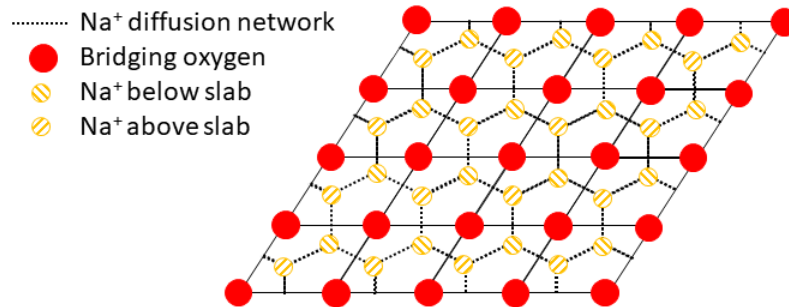

Figure 2. Idealized conduction slab of Na-β″-alumina. The figure is based on [37].

Compared to other conductive materials containing Na-ions, Na-β″-alumina has a higher ionic conductivity (Figure 3). Na-β″-alumina single crystals reach an ionic conductivity of 1.0 S cm^{-1} at $300\,°C$ along the conductive planes. Single crystals are not suitable for practical applications due to their complex synthesis and small size. [38–40] Instead, polycrystalline electrolytes with a statistically distributed spatial orientation of the crystallites are used. These electrolytes typically have a conductivity of 0.15 S cm^{-1} to 0.30 S cm^{-1} at $300\,°C$. [38–41] This conductivity is higher than NASICON-type (Na super

ionic conductor) electrolytes. [42–47] Electrolytes like $Na_5SmSi_4O_{12}$ or $Na_5ScSi_4O_{12}$ have greater ionic conductivity than Na-β''-alumina. However, they have the drawback of requiring rare-earth elements and a low chemical stability against sodium. [48–50] Na-β''-alumina electrolytes, in contrast, have proven their long-term stability in NAS® and Na/NiCl₂-battery systems over many years. [12,51–55] The main drawback as far as chemical stability is concerned, is the sensitivity to moisture of Na-β''-alumina-electrolytes. Within one hour of exposition to moist air, the surface of Na-β''-alumina-electrolytes is saturated with water. [56] This process is reversible by heating the electrolyte at 100 °C to 250 °C. [57] The second and subsequent process in moist air is the diffusion of H_3O^+ into the lattice by exchanging with Na-ions. This process takes several days. The exact time is dependent on the composition of the Na-β''-alumina-electrolyte and the reaction conditions. [57–59]
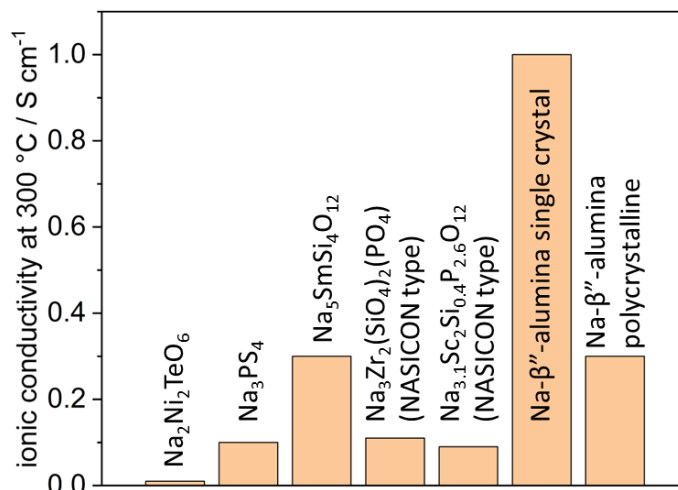

Figure 3. Ionic conductivity of different solid state Na-ion conductors: $Na_2Ni_2TeO_6$ [60]. Na_3PS_4 [61], $Na_5SmSi_4O_{12}$ [48], $Na_3Zr_2(SiO_4)_2(PO_4)$ [62], $Na_{3.1}Sc_2Si_{0.4}P_{2.6}O_{12}$ [63], Na-β''-alumina (single crystal) [39] and Na-β''-alumina (polycrystalline) [64] at 300 °C.

2.2   Manufacturing processes for Na-β"-alumina electrolytes

The production of Na-β″-alumina electrolytes can be carried out by various methods. They depend on the geometry of the electrolyte and the number of electrolytes that are to be produced. Figure 4 gives a general flow schema of the production process.
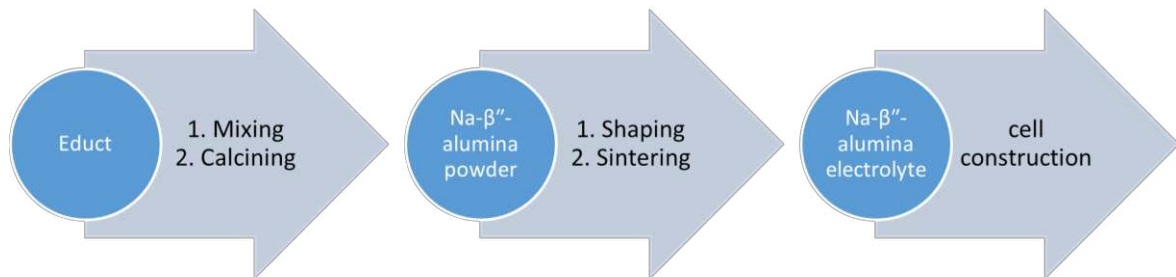

Figure 4. Schematic diagram of the Na-β″-alumina electrolyte manufacturing process.

First, the reactants containing at least one Al- and one Na-source are mixed, mainly through dry mixing. [37,64,65] At the laboratory scale sol-gel processes are also used. [66–68] The reactant mixture is then calcined at 1000 °C to 1300 °C to form Na-β″-alumina powder. This step is essential for two reasons [37,69]:

- It prevents deformation of the electrolyte due to a phase transition while sintering

- Na-β″-alumina powder is not soluble in water or ethanol but can be suspended, which is crucial for several production techniques discussed in the next paragraph

The first step in obtaining a solid electrolyte from the Na-β″-alumina-powder is to shape the powder into a green body. A green body has the same shape as the final electrolyte but shrinks during sintering. Several methods are used to shape the Na-β″-alumina powder.

The most common shaping method is isostatic or uniaxial pressing. [22,37,70,71] To obtain defect-free green bodies, granulation of the powders with an organic binder is required. The granulation can be performed by dry granulation or spray drying Na-β″-alumina slurry. [64,72,73]

Alternative methods for producing a green body from a Na-β″-alumina slurry are slip casting [18,74], tape casting [75,76], plastic extrusion [37,77] or electrophoretic deposition. [78–80]

The final step in the production chain of Na-β″-alumina electrolytes is the sintering step. Sintering is defined as solidifying packed particles by particle growth and pore elimination

at high temperatures. [69] The main driving force of this process is the minimization of the high surface and interfacial energy of a powder. The high temperatures are necessary to enable the material transport needed for particle growth and pore elimination. Sinter regimes for Na-β''-alumina ceramics have a typical peak temperature of about 1600 °C. [37,73] This high temperature is necessary to guarantee a densely sintered Na-β''-alumina ceramic of low porosity. The peak temperature is applied for a short time of several minutes to avoid the formation of large crystallites and to minimize the sublimation of Na_2O. Another step for avoiding Na_2O sublimation is encapsulating the green bodies while sintering. Crucibles made from MgO are used at an industrial scale, while crucibles made from platinum are used for small samples at the laboratory scale. [37,70,73] Lower sintering temperatures applied for a more extended period are unsuitable for bypassing the Na_2O evaporation problem because they lead to an unequal distribution of Na-ions within the ceramic. [37]

A final production technique differs clearly from those already mentioned. This technique is VPC (Vapor phase conversion) of conventional Al_2O_3 ceramics (typically sintered at about 1400 °C) [69] to Na-β''-alumina. [81,82] For this purpose, Al_2O_3-ceramics are produced and sintered. Afterward, the ceramic body gets covered in a Na-source (mostly Na-rich Na-β''-alumina powder) and thermally treated at about 1400 °C. At this temperature, Na_2O sublimates from the Na-rich powder into the Al_2O_3-ceramic and forms a Na-β''-alumina electrolyte. VPC enables the production of Na-β''-alumina without temperature steps as high as 1600 °C. However, it is unsuitable for mass production since the Na-source can be used only once, and an additional costly thermal process is necessary.

2.3 Material-process-interactions and derived properties of Na-β''-alumina electrolytes

In addition to low porosity, a high phase content of the Na-β''-alumina crystal phase is crucial while developing a manufacturing chain for electrolytes. In addition to the Na-β''-alumina crystal phase, small amounts of secondary phases such as Na-β-alumina and $NaAlO_2$ can be found in Na-β''-alumina-electrolytes. [37] Both phases are unwanted and should be minimized by a carefully tuned sintering regime and chemical composition. The phase diagram Na_2O/Al_2O_3 system is highly complex, where the hatched region corresponds to the coexistence of Na-β-alumina and Na-β''-alumina Figure 5. The experimental approach to gain a reliable phase diagram of the chemical system is difficult

due to several metastable and non-stoichiometric crystal phases. Also, Na-β''-alumina is metastable if synthesized without any dopants. [21] Those problems result in several slightly different Na_2O/Al_2O_3-phase diagrams depending on the measuring setup chosen. [21,37,83,84]
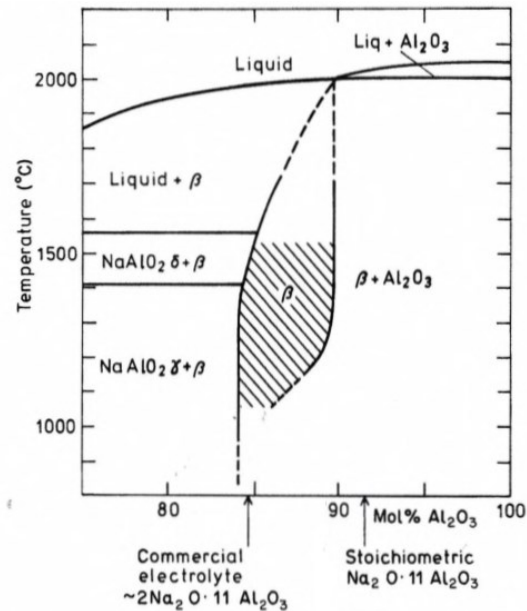

Figure 5. Phase diagram of the Na_2O/Al_2O_3 system. The hatched region corresponds to the coexistence of Na-β-alumina and Na-β''-alumina. Reprinted with permission from [37].

The Na-β-alumina crystal phase $(Na_2O) \cdot x\ Al_2O_3$ ($8 < x < 11$) is, in comparison to Na-β''-alumina $(Na_2O) \cdot x\ Al_2O_3$ ($5 < x < 7$), poor in Na, shows a lower conductivity for Na-ions and should therefore be avoided when synthesizing a Na-β''-alumina electrolyte. [30,85] One key to minimize the Na-β-alumina phase content is the addition of Li- or Mg-ions, as elucidated in chapter 2.4.

$NaAlO_2$ is also a common impurity of Na-β''-alumina-electrolytes and occurs when Na-β''-alumina decompose to Na-β-alumina [83], or the Na-content of the reactant mixture is too high. $NaAlO_2$ can often be found along the grain boundaries of Na-β''-alumina grains and, furthermore, increases the moisture sensitivity of Na-β''-alumina-electrolytes. [70,85]

2.4 Impacts from doping of Na-β″-alumina on the physical properties and the mineral composition

2.4.1 Stabilization of the Na-β″-alumina phase by Li^+ and Mg^{2+} doping

As mentioned, stabilizing the Na-β″-alumina crystal phase by the addition of Li- or Mg-ions is crucial if the decomposition of the Na-β″-alumina crystal phase at temperatures above 1500 °C is to be avoided. [21,83] Since sintering Na-β″-alumina electrolytes takes temperatures of about 1600 °C, Na-β″-alumina phase decomposition inevitably occurs during electrolyte production. Use of stabilizing agents is therefore essential for obtaining high-quality electrolytes. In consequence, there is little literature on Na-β″-alumina electrolytes without Li^+- or Mg^{2+} doping. [37,70,86] According to *Imai* and *Harata* [87], stabilized Na-β″-alumina crystal phases are stable up to temperatures of 1700 °C. Since the present work uses lithium stabilized Na-β″-alumina, the ternary phase diagram of Li_2O-Na_2O-Al_2O_3 is presented in Figure 6. The diagram underlines the difficulty synthesizing a pure Na-β″-alumina crystal phase, which only occurs in a minimal window at the mass fraction: 8.5 % Na_2O, 0.8 % Li_2O, and 90.7 % Al_2O_3 [34]. Other researchers confirm this result with only small deviations. [88,89]
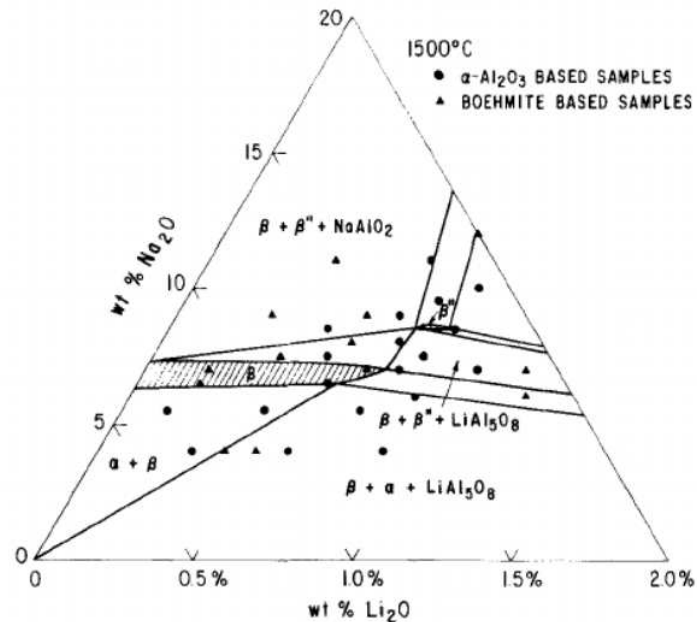

Figure 6. Ternary phase diagram of Li_2O-Na_2O-Al_2O_3. Reprinted with permission from [34].

Zyl et al. [90] proposed a widely accepted [70,91,92] mechanism for forming lithium stabilized Na-β″-alumina synthesized from Al-sources like boehmite, gibbsite, or other aluminum hydroxides. The mechanism and intermediate products vary depending on the

educts used, *e.g.*, α-Al$_2$O$_3$ or Al(NO$_3$)$_3$, but since the present work used boehmite as an educt, the mechanism proposed by *Zyl et al.* [90] is presented.

Boehmite decomposes to cubic-close-packed γ-Al$_2$O$_3$ when heated up to around 500 °C. Further heating enables the incorporation of bridging oxygen, originating from Na$_2$O, Li$_2$O, or similar compounds, between the fourth and fifth layer of the γ-Al$_2$O$_3$ lattice. To preserve electric neutrality, Na$^+$ and Li$^+$ diffuse into the layer. The close packing remains during this transition due to shearing of the spinel blocks (Figure 7 a). Although sodium ions are too large to diffuse further, lithium ions can diffuse into the spinel blocks and occupy cation sites (Al^{3+}-sites) (Figure 7 b). This occupation stabilizes the cubic closely-packed oxygen spinel blocks and prevents the decomposition of Na-β″-alumina to Na-β-alumina. This proposed mechanism is supported by the fact that the diffusion of lithium ions into spinel blocks occurs in manganese spinel [93].
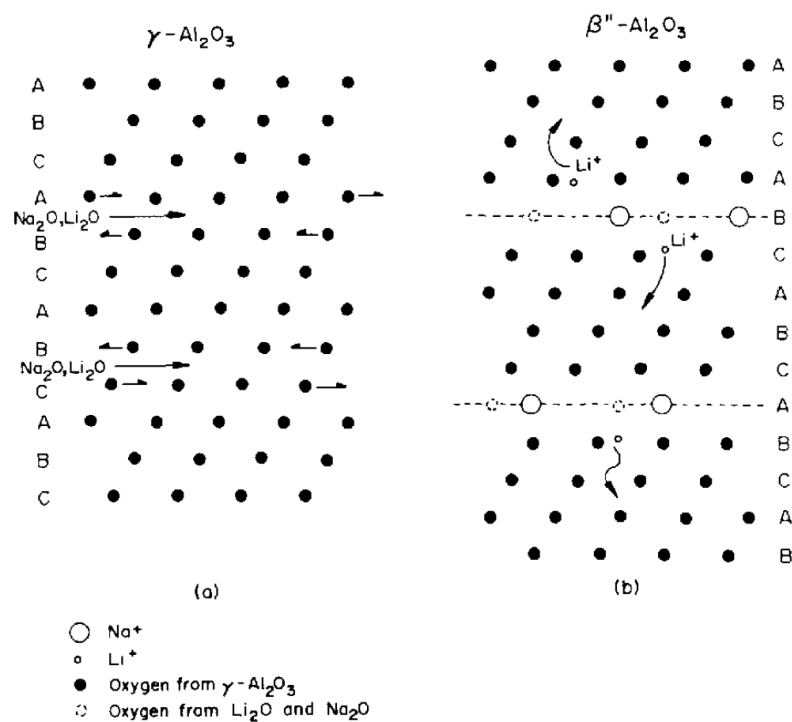

Figure 7. Schematic illustration of the conversion from γ-Al$_2$O$_3$ (a) to lithium stabilized Na-β″-alumina (b) as proposed by *Zyl et al.* [90] reprinted with permission.

2.4.2 Transition metal doping of Na-β″-alumina

The first publications about doping Na-β″-alumina electrolytes (beside Li$^+$ and Mg^{2+}) date back to the 1970s. Those publications mainly focus on exploring the effects of impurities like Si^{4+} or Ca^{2+} on Na-β″-alumina electrolytes. [94–98]

In 1976 *Boilot et al.* [98] added new data to ideas derived from two publications [87,99] and theorized that metal ions with an oxidation number of one or two and ionic radii of < 0.097 nm can enter the spinel block of Na-β''-alumina and replace Al^{3+}. The addition of the ions they tested (Ni^{2+}, Co^{2+}, Cu^{2+}, Zn^{2+}, Mn^{2+}, Cd^{2+} and Mg^{2+}) increased the conductivity of Na-β''-alumina. They therefore concluded that replacement of the Al^{3+}-ions reduces the amount of oxygen within the conduction slab (bridging oxygen) because less oxygen is needed to achieve a charge balance [90] . Therefore, higher mobility of the Na-ions within the slab can be achieved. Ca^{2+}, Sr^{2+}, Pb^{2+} and Ba^{2+} with an ionic radius of > 0.097 nm are too large to substitute Al^{3+} in the spinel block and are therefore located in the conduction plane and hinder the diffusion of the Na-ions. Different doping amounts or sintering temperatures were not tested. Also, the microstructure or the fracture strength was not characterized by *Boilot et al.* [98]

Boilot et al. [100] published another paper in 1977 containing the results of EPR (Electron paramagnetic resonance) measurements on doped Na-β-alumina single crystals (not Na-β''-alumina). To check whether the foreign ions are located in the conduction plane, the spinel block, or both, they tried to exchange foreign ions in the conduction plane by heating the Na-β-alumina crystals in a melt of NaI. If the foreign ions were located in the conduction slab, they would be washed out and no longer traceable. If the foreign ions were located in the spinel block, the EPR spectra would have been unaltered, and if the foreign ions were located in the conduction slab and within the spinel blocks, the EPR spectra would have been simplified.

The foreign ions tested were Cr^{3+}, Cu^{2+}, Gd^{3+}, and Mn^{2+}. It was found that all ions tested were located in the spinel blocks after heat treatment of 650 °C. Similar experiments on Na-β''-alumina do not yet exist. Furthermore, *Boilot et al.* [108] and the two publications they cited [87,99] are qualitative and mechanistic studies. Therefore, they lack a broad number of tested doping levels, sintering temperatures, and determination of the characteristic fracture strength, microstructure, or density. Another publication on 3d transition metal doping of Na-β''-alumina was that in 1982 by *Wasiucionek et al.* [101]. They doped Na-β''-alumina with a mass fraction of 4.0 % CoO, NiO, CuO, and ZnO (without the known phase stabilizers Li^+ or Mg^{2+}). They sintered the samples at 1600 °C and compared the results to a sample stabilized with lithium. They found a distinctive drop of the Na-β''-alumina phase content and hence the ionic conductivity decreased from 0.28 S cm^{-1} to about 0.1 S cm^{-1} (300 °C) in all samples that forego Li^+-addition. The microstructure or characteristic fracture strength of the electrolytes was not described.

The next important step regarding transition metal doping of Na-β''-alumina was not an actual doping process but an incorporation. *Viswanathan et al.* [102] published in 1983 that adding ZrO_2 does not lead to Zr^{4+} incorporation into the crystal lattice of Na-β''-alumina, but ZrO_2 forms a secondary phase. Therefore, they described the process as incorporation instead of doping. The incorporation of a mass fraction of 25 % ZrO_2 increased the characteristic fracture strength from 162 MPa to 379 MPa. The increase was mainly due to changes in the microstructure. The small, inert ZrO_2 grains disrupt the grain growth of Na-β''-alumina crystallites and contribute to a uniform microstructure shaped by small grains. Small grains tend to improve the characteristic fracture strength of a ceramic body since the vast number of grain boundaries can inhibit fracture growth. [69] In contrast, incorporating ZrO_2 hinders the diffusion of Na-ions and hence reduces the ionic conductivity of Na-β''-alumina electrolytes. Nevertheless, ZrO_2 (often fully Y-stabilized) incorporation became a standard technique used in numerous publications. [103–107] For industrial application, sufficient characteristic fracture strength is chosen over increased ionic conductivity because a single pore and a resulting micro fracture can lead to cell failure in practical applications. It should also be mentioned that ceramic Na-β''-alumina electrolytes have a relatively low characteristic fracture strength due to the weakly-bonded conduction planes [103] compared to other ceramic materials like Al_2O_3, MgO, or ZrO_2.

An example of a backscattering electron image of a commercial Na-β''-alumina/yttria-stabilized zirconia (YSZ) electrolyte produced by *Fraunhofer IKTS* is shown in Figure 8. The bright grains consist of YSZ, while the darker matrix consists of Na-β''-alumina.

Summing up, ZrO_2 incorporation is well-established and will not be further tested in this thesis but should still be mentioned because it is in common use. [71,104,108–111]
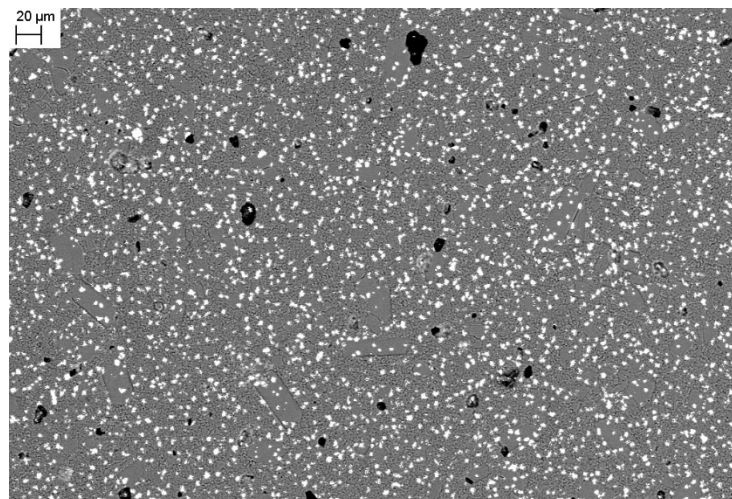
Figure 8. Example of a backscattering electron image of a commercial Na-β″-alumina/YSZ electrolyte produced by *Fraunhofer IKTS.*

In the decades after 1980 research on Na-β″-alumina decreased distinctly due to the triumph of LIBs, and no further breakthroughs regarding transition metal doping were published (Figure 9). This trend stopped around 2010 with the broader awareness of the ethical issues with LIBs and of their resource demands [112,113]. This awareness stimulated interest in alternative battery systems. This development also led to new publications regarding the transition metal doping of Na-β″-alumina.
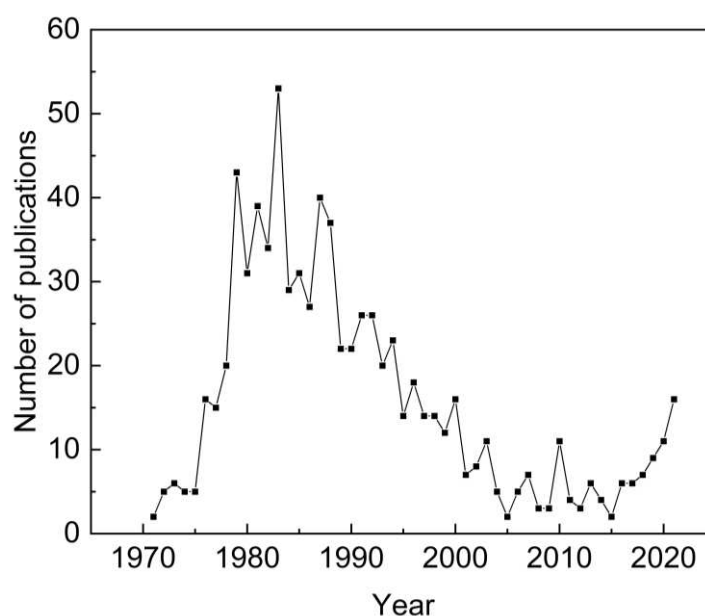
Figure 9. The number of scientific publications per year (1970/01/01-2021/11/01) was found by searching the keyword "Na-β″-alumina" at the scientific research engine "*SciFinder*" by *CAS.* Date: 2021/11/01

Most publications report the effects of TiO_2 (or other Ti^{4+}-compounds) doping on Na-β″-alumina electrolytes. *Shan et al.* [114] synthesized magnesium stabilized Na-β″-alumina

electrolytes by the citrate sol-gel method and observed increased Na-β″-alumina phase content, relative density, characteristic fracture strength, and ionic conductivity by adding mass fractions of up to 3.0 % titanium butoxide to the reactant solution. The phase content of Na-β″-alumina was raised from 54 % to 90 % by adding a mass fraction of 1.5 % titanium butoxide.

To evaluate the phase content, *Shan et al.* [114] used the two distinctive peaks of Na-β″-alumina and Na-β″-alumina according to equation (1). Where f (Na-β″-alumina) represents the Na-β″-alumina phase content, $I_{\text{Na-β″-alumina}}$ the intensity of the peak (20$\underline{10}$) at 45.9 °, and $I_{\text{Na-β-alumina}}$ is the intensity of the peak (10$\underline{11}$) at 44.5 °. This method assumes that no other crystal phases are present and is applied by various other researchers to evaluate the Na-β″-alumina phase content. [27,28,115,116] The limitation to two crystal phases heavily implies Rietveld refinement for phase content analysis.

$$f(\text{Na} - \beta'' - \text{alumina})\% = 100 - \frac{I_{\text{Na}-\beta-\text{alumina}}}{I_{\text{Na}-\beta-\text{alumina}} + 0.85 \cdot I_{\text{Na}-\beta''-\text{alumina}}} \cdot 100\% \quad (1)$$

The ionic conductivity of *Shan et al.* [114] samples rose from 0.04 to 0.21 S cm^{-1} at 350 °C by adding a mass fraction of 1.0 % titanium butoxide. The increased relative density was created by an improved densification process, illustrated by SEM measurements (Figure 10). The reasons for those improvements were not further investigated, but two theories were introduced:

- *Erkalfa et al.* [117] postulated that TiO_2 doping increases diffusion while sintering Al_2O_3 by increasing the amount of Al^{3+} vacancies, which seems, according to *Shan et al.,* [114] also possible for the sintering process of Na-β″-alumina electrolytes

- *Shan et al.* [114] furthermore assumed that a transient liquid phase could be formed that would support the densification of the Na-β″-alumina ceramic, leading to a high relative density
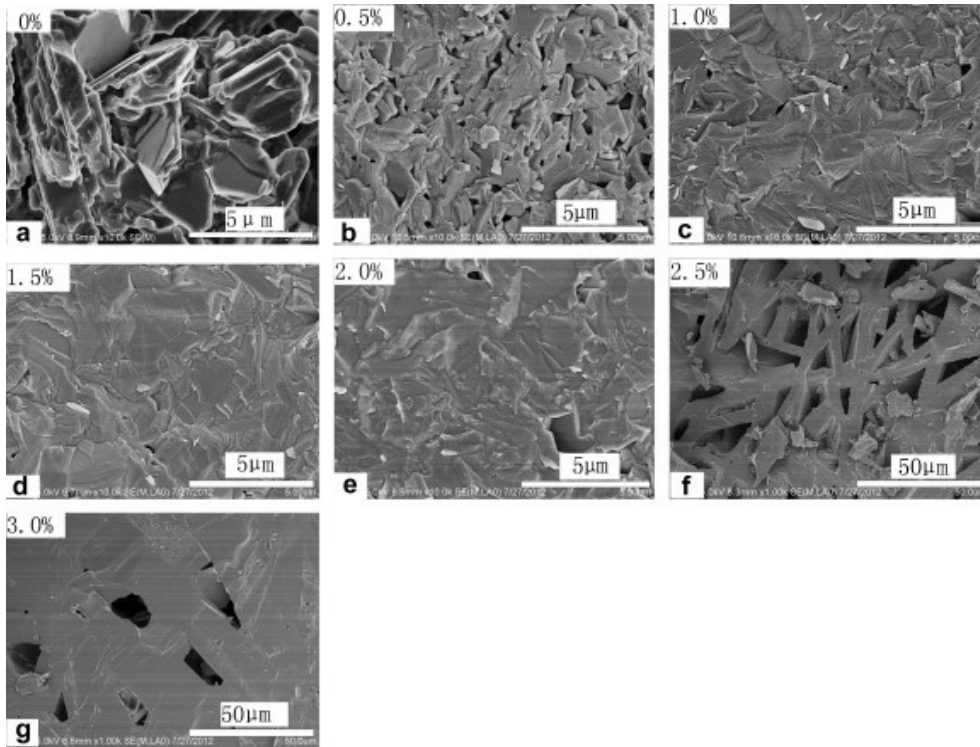
Figure 10. SEM images of magnesium stabilized Na-β"-alumina doped with different amounts of titanium butoxide. Reprinted with permission from [114]

Lu et al. [118] also observed increased densification by adding titanium butoxide to the reactant mixture. Their postulate [125] was that phases like $Na_8Ti_5O_{14}$, $Na_2Ti_3O_7$, and $Na_2Ti_6O_{13}$, melting between 1000 °C and 1300 °C, cause liquid-assisted sintering. Unfortunately, *Lu et al.* [125] did not publish ionic conductivity or characteristic fracture strength of their titanium butoxide doped electrolytes. *Wei et al.* [28] doped their magnesium stabilized Na-β"-alumina with TiO_2 (mass fractions of 0.0 to 2.0 %) and improved the ionic conductivity from 0.03 to 0.18 S cm^{-1}, and the characteristic fracture strength from 210 MPa to 280 MPa. They also assumed a transient liquid phase as the main factor.

Nevertheless, none of these authors [121,125,28] found any hint of a transient liquid phase while sintering in their XRD or SEM measurements.

Three more researchers tested the effects of Ti^{4+} doping on ZrO_2 strengthened magnesium stabilized Na-β"-alumina. [27,119,120] Doping amounts of mass fractions of up to 4.0 % were tested. They proved that ZrO_2 strengthened magnesium stabilized Na-β"-alumina electrolytes benefit from the dopant regarding their relative density, characteristic fracture strength, and ionic conductivity. Nevertheless, none of the researchers found any indication of the postulated liquid phase in XRD or SEM measurements. *Yang et al.* [27] assumed that the maximal dopant amount of a mass fraction of 4.0 % TiO_2 is still not high enough

for corresponding XRD peaks to be measured. The first to test TiO_2 doping on lithium stabilized (instead of Mg^{2+}) Na-β''-alumina were *Chen et al.* [121]. They demonstrated the increased densification and the beneficial influence on the ionic conductivity and characteristic fracture strength upon doping. The conductivity of their samples was lifted from 0.121 S cm^{-1} (the lowest reported doping level was a mass fraction of 0.1 % TiO_2) to 0.173 S cm^{-1} by adding a mass fraction of 0.8 % of TiO_2. In summary therefore the addition of Ti^{4+}-compounds increases the densification of Na-β''-alumina. If a transient liquid phase is involved in this process, its existence has not been proven so far.

Furthermore, it was shown, for example, by *Shan et al.* [114], that the Na-β''-alumina phase content was maximized by Ti doping if the undoped sample had a low phase content. The ionic conductivity and characteristic fracture strength can also be increased. However, it is still unclear if changes in the microstructure, the crystal structure, or an improved phase contend are most impactful.

In addition to Ti^{4+}-compounds, some other 3d transition metal compounds have also been tested although less often.

For example, *Zhu et al.* published two articles about Cr^{3+} doping (up to a mass fraction of 1.5 %) of lithium stabilized Na-β''-alumina in 2020. [115,122] They managed to increase the ionic conductivity from 0.061 S cm^{-1} to 0.110 S cm^{-1} (at 350 °C) and the characteristic fracture strength from 150 MPa to 215 MPa, by adding a mass fraction of 0.15 % Cr_2O_3. They assumed that Cr^{3+}-ions were able to occupy vacant Al^{3+} lattice positions and stabilize the Na-β''-alumina crystal phase. According to *Zhu et al.* [115,122], this led to a higher phase content and increased densification. A shift of XRD peaks or an introduced crystal phase was not detected. The authors assumed a peak shift due to doping would only be observed at higher doping contents.

Kennedy et al. [123] doped 1979 magnesium stabilized Na-β-alumina (not Na-β''-alumina) with $Mn(NO_3)_2$ and found an increase of the ionic conductivity from 0.018 to 0.025 S cm^{-1} at 300 °C for the addition of a mass fraction of 4.0 %. However, they did not analyze the different sintering regimes or the characteristic fracture strength. *Lu et al.* [118] co-doped Na-β''-alumina with a mass fraction of 5 % $Mn(NO_3)_2$, $Ti(OCH(CH_3)_2)_4$, and ZrO_2. The ionic conductivity or the characteristic fracture strength of $Mn(NO_3)_2$ single doped Na-β''-alumina was not reported, but *Lu et al.* noted a slightly increased shrinkage while sintering $Mn(NO_3)_2$ doped Na-β''-alumina. Therefore, there is still no extensive study of the influence of Mn doping on lithium stabilized Na-β''-alumina.

Fe_2O_3 doping was tested by *Lee et al.* [124]. They first doped Al_2O_3 with a mass fraction of 5.0 % Fe_2O_3 and successfully produced Na-β''-alumina electrolytes by the VPC method. They showed that iron-ions occupied Al^{3+}-positions within the Na-β''-alumina crystal structure. *Butts et al.* [125] used even higher doping levels than the high levels of *Lee et al.* [131] and replaced 52 % of the Al^{3+} with Fe^{3+}. They suggested that a low amount of Fe^{2+} was present even though it was not confirmed by *Mössbauer* spectroscopy. The high amount of dopant clearly changed the lattice constants. Nevertheless, the Na-β''-alumina crystal structure stayed intact. Furthermore, the highly doped Na-β''-alumina was tested as an anode material for sodium-ion cells. The intercalation reaction proposed is shown in equation (2).

$$Na_{2-x}(Al_{0.48}Fe_{0.52})_{11}O_{17} + Na^+ + e^- \rightleftharpoons Na_2(Al_{0.48}Fe_{0.52})_{11}O_{17} \qquad (2)$$
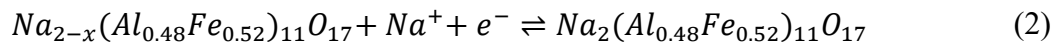
Co^{2+} doping was so far only described in the publication of *Wasiucionek et al.* [101] dating back to 1982 already mentioned. They doped unstabilized Na-β''-alumina with a mass fraction of 4.0 % CoO and found lower Na-β''-alumina phase content (80 %) than in Na-β''-alumina doped with Li^+ (100 %), Ni^{2+} (90 %) or Zn^{2+} (96 %). In consequence, ionic conductivity was also reduced, as mentioned before. *Wasiucionek et al.* [109] did not discuss the microstructure or the characteristic fracture strength.

In addition to the work of *Wasiucionek et al.* [101], *Zhu et al.* [116] tested the influence of NiO on lithium stabilized Na-β''-alumina. Their work is more detailed and shows that doping with a mass fraction of 0.25 % NiO remarkably increased the ionic conductivity (from 0.015 S cm^{-1} to 0.066 S cm^{-1} at 350 °C) and enhanced the characteristic fracture strength to 296 MPa. The improvements were ascribed mainly to reduced porosity due to the dopant. A criticism of this result is that the ionic conductivity is low compared to other undoped or doped polycrystalline Na-β''-alumina electrolytes. A reason for this observation is not given within the publication. [101]

CuO on lithium stabilized Na-β''-alumina doping was tested by *Moghadam et al.* [126]. In contrast to most other researchers, they determined the lattice constants. Both constants (a=b and c) shrank slightly with increasing doping levels. The ionic conductivity at 350 °C rose from 0.056 S cm^{-1} to 0.121 S cm^{-1} by adding a molar fraction of 1.5 % CuO. *Moghadam et al.* [126] explained the increase by a higher occupation ratio of the Na-ion position since Cu^{2+} replaces Al^{3+} while the charge neutrality has to be retained. Furthermore, they observed a more uniform microstructure due to the dopant.

ZnO doping was not only tested by *Wasiucionek et al.* [101], who reported reduced ionic conductivity compared to all other samples tested. *Engstrom et al.* [39] produced ZnO doped Na-β''-alumina single crystals. The conductivity at high temperatures (> 200 °C) stayed constant and conductivity of the ZnO doped sample improved significantly at room temperature.

Thus, in summary, the influence of many 3d transition metal dopants on Na-β''-alumina electrolytes have already been tested. Nevertheless, the measured ionic conductivities and characteristic fracture strengths are difficult to compare because of different reactants for synthesis, co-dopants, synthesis routes, sintering temperatures, and measuring temperatures (for the ionic conductivity) used by the various researchers.

Ti^{4+}-addition was tested several times and clearly increased ionic conductivity and the characteristic fracture strength. Nevertheless, it has not yet been possible to prove phases enabling the often-postulated liquid-assisted sintering. I therefore tested Ti^{4+} doping in this work because it is the 3d transition metal dopant most discussed.

Mn_3O_4 was chosen as the Mn-based dopant. Mn doping was so far only tested superficially. Furthermore, Mn_3O_4 offers Mn^{2+}-ions that able to occupy Al^{3+} positions and could therefore increase the Na^+-concentration in the conductive slab, as was postulated for Ni^{2+} or Cu^{2+} doping (see above). Mn^{3+} ions could influence the densification process as has been demonstrated for Cr^{3+} doping.

The last systematically tested dopant within this work was Ni^{2+}, which was already systematically tested by *Zhu et al.* [116] by increasing the ionic conductivity of the electrolytes by 300 %. Nevertheless, the ionic conductivity of their samples stayed way below average.

2.5 Liquid-assisted sintering

As explained in chapter 2.4.2, liquid-assisted sintering is a mechanism proposed for transition metal doped Na-β''-alumina. Therefore, a general explanation of the effects of a liquid phase on a sintering process is given in this chapter. In this general explanation, I discuss a ceramic body formed from two compounds. One of those components melts at a temperature lower than the sintering temperature but the other compound remains solid. This case is slightly different from sintering transition metal doped Na-β''-alumina. This is because the melting components are formed from the transition metal dopant during the sintering process and are not present initially.

Salmang et al. [69] defined four steps of a liquid-assisted sintering process (Figure 11):
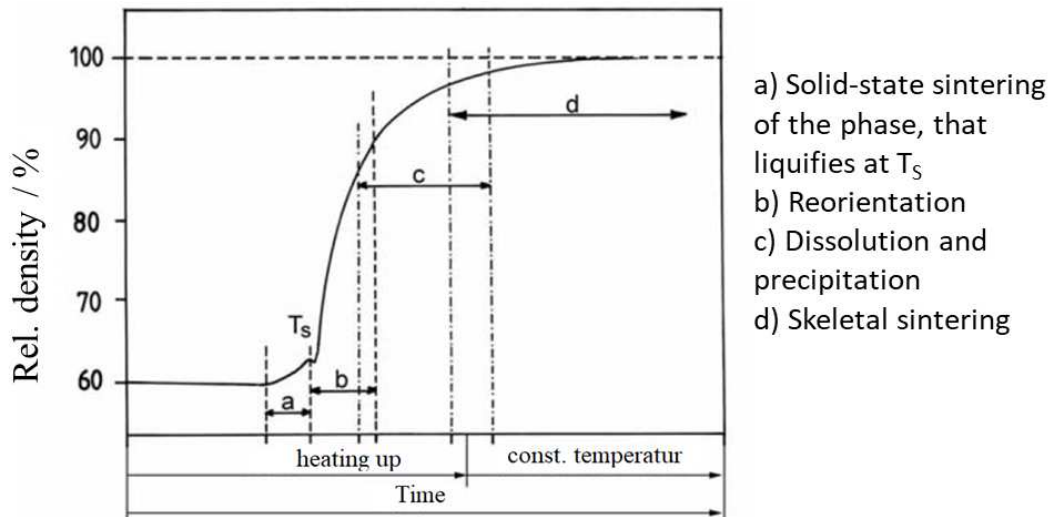
Figure 11. Idealized relative density to time curve of a liquid-assisted sintering process. Translated and reprinted with permission from *Salmang et al.* [69]

In the first stage of the sintering process, the compound with the low melting temperature starts a normal sintering process before it melts. This process is labeled with "a" in Figure 11, illustrating the general relative density to time curve of a liquid-assisted sintering process.

In the second step, grains of the solid compound are reorientated to minimize the surface- and interfacial energy. The influence of this step on the sintering procedure is highly dependent on the amount of the liquid phase. At a volume fraction of less than one-third of the liquid phase, the densification caused by reorientation processes decreases steadily. [69] Since amounts of up to a mass fraction of 5 % of transition metal dopant is typically added to Na-β″-alumina, the reorientation is likely less influential than the third step of liquid-assisted sintering.

The third step is the process of dissolution and precipitation. While this process occurs, dissolution of the solid phase in the liquid phase takes place. By subsequent precipitation, large grains grow while small grains vanish. This process is a form of *Ostwald* ripening. In the case of anisotropic solid phases, an idiomorph grain growth is typical.

The last step is dominated by skeletal sintering, especially if the solid phase outweighs the liquid phase. While the process of skeletal sintering, grains of the solid phase are sintered together in areas where no liquid phase is present. Also, coalescence phenomena are observable, where large grain boundary surfaces are sintered together while small grains are still present. The resulting microstructure can be seen in Figure 12. According to *Salmang et al.* [69], this is the most characteristic phenomenon of a liquid-assisted sintering process.

32
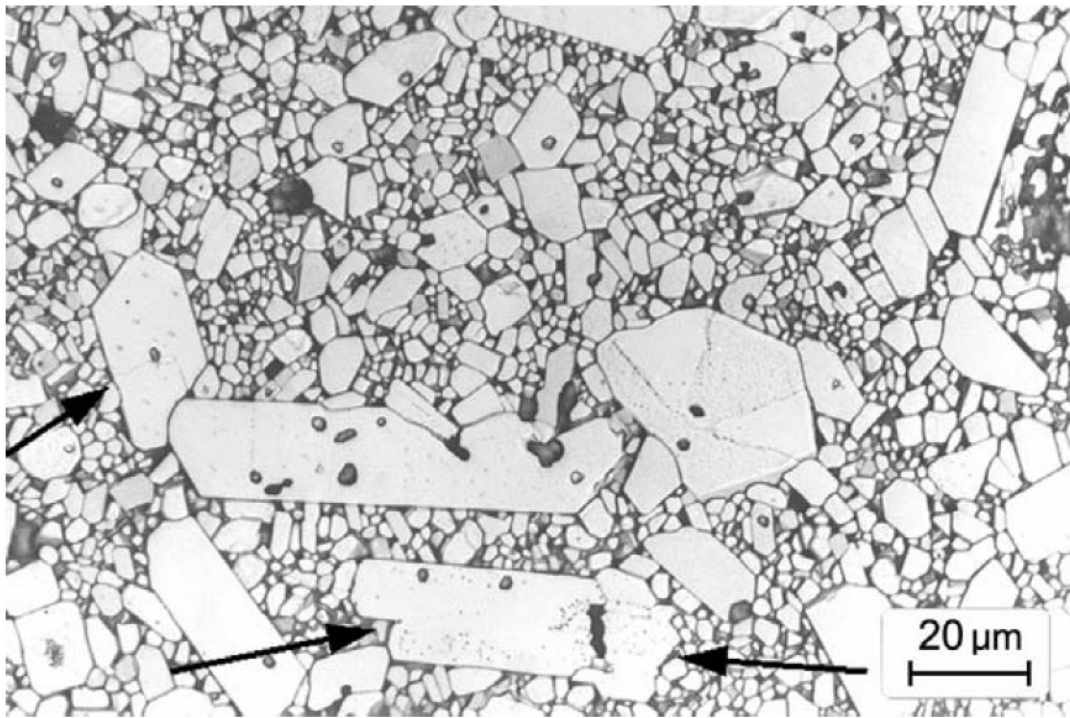
Figure 12. SEM image of an Al_2O_3 ceramic after liquid-assisted sintering. The arrows indicate possible areas with coalescence phenomena. Reprinted with permission from *Salmang et al.* [69]

It can be summed up that liquid-assisted sintering enables additional densification in contrast to conventional solid state sintering. Thereby, lower sintering temperatures are often needed to obtain a densely sintered ceramic. A drawback of liquid-assisted sintering is the greater likelihood of excessive grain growth and an uneven grain size distribution.

2.6   Na-β″-alumina electrolytes in Na/NiCl₂ cells

In addition to the established Na/S-batteries and AMTECs (Alkali-metal thermal to electric converter), Na/NiCl₂-batteries are the main commercial application of Na-β″-alumina electrolytes. The Na-β″-alumina electrolytes developed within this thesis were tested in Na/NiCl₂-cells (see sections 4.3 and 4.4). Therefore, the operating principle of those cells will be explained in the following. The cell redox reaction can be seen in equation (3). While charging the cell, NaCl and Ni react to NiCl₂ and Na. The resulting cell has an open circuit potential of 2.58 V at 300 °C, [52] which is the typical operating temperature of Na/NiCl₂-cells.

$$2\,\text{NaCl} + \text{Ni} \rightleftharpoons NiCl_2 + 2\,Na \qquad (3)$$
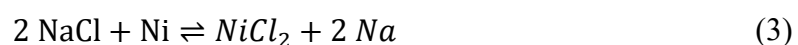
Figure 13 shows a simplified cross-sectional sketch of a commercially available tubular Na/NiCl₂-cell. The function of the compounds is briefly explained in the following:

- The current collector (colored orange in the sketch), which is the positive pole / cathode upon discharging, in the middle of the cell is usually made of nickel. It is placed in the center of the active material
- The active material (labeled by grey points in the sketch) consists of Ni and NaCl in the discharged state and $NiCl_2$ in the charged state. Furthermore, it is infiltrated with $NaAlCl_4$, which is liquid at 300 °C and acts as secondary electrolyte
- The active material is filled in a tube made from the solid electrolyte Na-β″-alumina (colored grey in the sketch)
- A sodium bath (labeled yellow in the sketch) – created during initial charging – serves as negative electrode (anode while discharging)
- The metal cell can (labeled blue in the sketch), contacting the sodium, is used as negative electrode´s current collector
- An isolating ceramic ring – typically Al_2O_3 – (labeled black in the sketch) seals the cell. It is joined to the metal parts and connected to the Na-β″-alumina ceramic by glass soldering
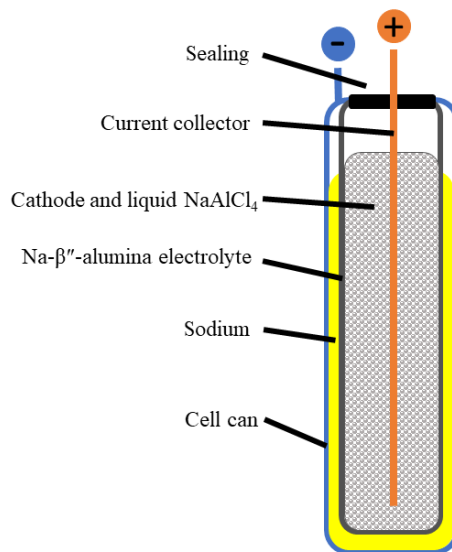
Figure 13. Sketch of a tubular Na/NiCl$_2$-cell.

After summarizing the functional principle of a Na/NiCl$_2$-cell, the active material and the coating of the Na-β″-alumina electrolyte, should be expounded in more detail.

To guarantee mass transport between the active material and solid Na-β″-alumina electrolyte, the liquid secondary electrolyte $NaAlCl_4$ (m.p. 156 °C) is used. [127] Between the solid (electrolyte) to liquid ($NaAlCl_4$) interface, only negligible interface resistances

occur. Therefore, the dry active material is infiltrated with NaAlCl$_4$ by applying various methods. It can be added to the cathode granulate in crystalline form, introduced as a melt by vacuum impregnation, or it is electrochemically formed during the initial charge of the cell by adding AlCl$_3$ and additional NaCl to the active material. [127] In addition to its role as an electrolyte, NaAlCl$_4$ protects the active material and the ceramic Na-β''-alumina electrolyte from damages caused by overcharging or over-discharging. The reversible overcharge and over-discharge reactions enabled by NaAlCl$_4$ are shown in Figure 14. [70]
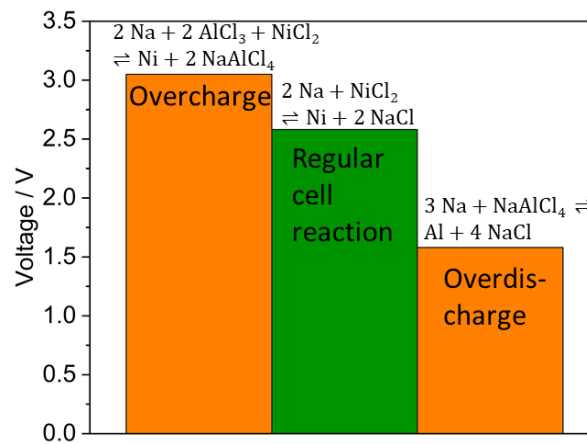
Figure 14. Overcharge and over-discharge reactions in Na/NiCl$_2$-cells.

The granulated active material is filled into the cell in the discharged state. Therefore, it consists of sodium chloride and nickel particles. The particle size must be small in order to maximize the surface area available for the electrochemical reactions. [128] The surface of the nickel particles is passivated by the formation of NiCl$_2$ while charging. In order to maintain a network of electronically conductive nickel within the active material, excess nickel is inserted into the material. [128] Varying amounts of iron can be added to the active material as an additional redox partner according to equation (4). The voltage of the reaction is 2.35 V at 300 °C. [127] Numerous publications discuss the possibility of using large amounts of iron instead of the costly nickel. [129–131] However, a large amount of iron reduces both the cell voltage and cell lifetime. [12]

$$Fe + 2\,NaCl \rightleftharpoons FeCl_2 + 2\,Na \qquad\qquad (4)$$
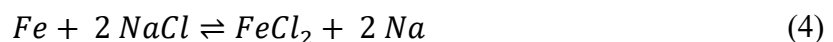
Besides these essential materials, FeS or other sulfur species are added to the active material to hinder grain growth during cell cycling. [132] In addition to FeS, Al powder is also added to the active material granules. It reacts during the initial charging of the cell according to equation

(5) (voltage of 1.6 V at 300 °C). [133] This reaction produces additional sodium in the negative electrode compartment during initial charging and thus ensures good electrical contact between the cell can and the ceramic Na-β″-alumina electrolyte. Furthermore, the reaction of the aluminum creates additional porosity in the active material, which improves cell performance. [127,133]

$$Al + 4\,NaCl \rightleftharpoons NaAlCl_4 + 3\,Na \qquad\qquad (5)$$
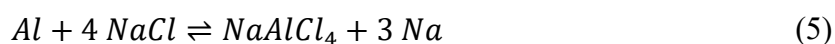
Sodium halogenides like NaF, NaBr, or NaI are often added to the active material to increase the conductivity of the secondary electrolyte $NaAlCl_4$ and hinder NaCl grain growth within the active material. [127,134,135]
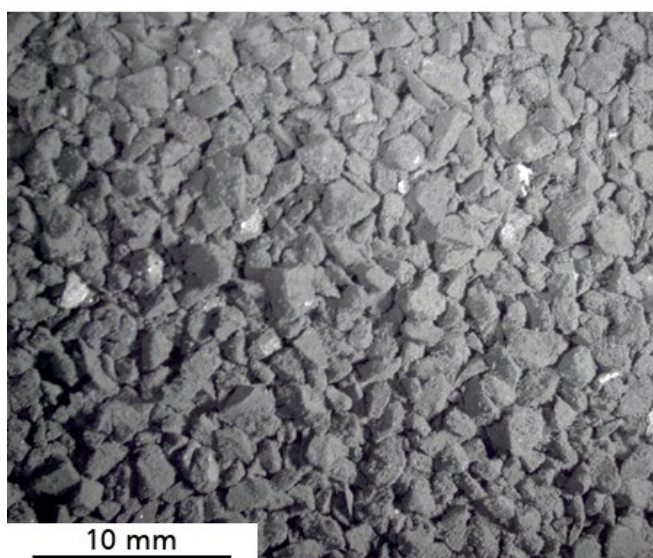
Figure 15. Picture of granulated active material (without $NaAlCl_4$) for $Na/NiCl_2$ cells.

A coating is necessary to ensure sufficient wettability of the Na on the Na-β″-alumina-surface. The coating decreases the contact angle of the liquid sodium and prevents the formation of large sodium drops with little contact with the ceramic. The most common coating is of carbon, as used in the present work. Figure 16 shows the influence of the carbon layer on the contact angle between a drop of sodium and Na-β″-alumina. Other known coating materials are Fe-, Sn-, Bi- or Pb-based [136–138]
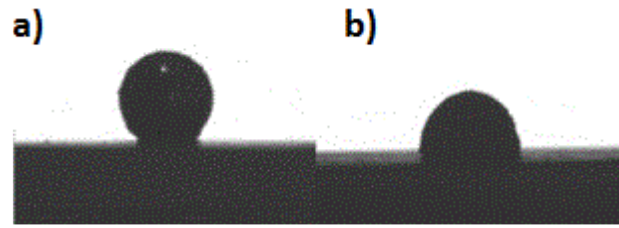
Figure 16. Picture of two liquid sodium drops. a) drop on an untreated Na-β″-alumina surface (contact angle 151°) b) drop on a carbon-coated Na-β″-alumina surface (contact angle 95°). Reprinted with permission from *Wen et al.* [139]

In contrast to the commercial tubular cell systems, the main cell system used for academic research and in the present work is a flat cell design described in chapter 3.4. This change in geometry does not change the processes within the cell but the cell setup is easier to assemble on the laboratory scale.

3. Experimental Section

3.1 Utilized chemicals and materials

The chemicals and materials used within this thesis are listed in Table 1.

Table 1. List of chemicals and materials used in the present thesis.

Chemical	Formula	Purity	Supplier
Acetone	C_3H_6O	> 99.5 %	Merk, Germany
Aluminum	Al	> 99.5 %	Carl Roth, Germany
Aluminum chloride	$AlCl_3$	> 99 %	Jobachem, Germany
Boehmite	$AlO(OH)$	> 98 %	Nabaltec, Germany
Carbon „Ensaco"	C	-	Imerys, France
Ethanol	EtOH	> 99.5 %	Merck, Germany
Iron(II) sulfide	FeS	Tech.	Avantor VWR, USA
Lithium carbonate	Li_2CO_3	> 99.8 %	Carl Roth, Germany
Mangan(IV) oxide	MnO_2	> 98 %	Carl Roth, Germany
Nickel T225	Ni	> 99.7 %	William Rowland, GB
Nickel(II) oxide	NiO	> 99 %	Lomberg Chemie, Germany
Potassium nitrate	KNO_3	> 99 %	ITW Reagents, USA
Silver nitrate	$AgNO_3$	> 99.9 %	Carl Roth, Germany
Sodium	Na	> 99.8 %	Acros organics, USA
Sodium bromide	NaBr	High-purity	Bernd Kraft, Germany
Sodium carbonate	Na_2CO_3	> 99 %	Carl Roth, Germany
Sodium chloride	NaCl	> 99.8 %	Akzo Nobel, Germany
Sodium nitrate	$NaNO_3$	> 99.5 %	Merck, Germany
Sodium nitrite	$NaNO_2$	> 99 %	Avantor VWR, USA
Sodium iodide	NaI	High-purity	Bernd Kraft. Germany
Titanium(IV) oxide	TiO_2	> 99.7 %	Alfa Aesar, USA

(anatase)

Terpineol	$C_{10}H_{18}O$	-	Carl Roth, Germany
Toluene	C_7H_8	> 99.8 %	Carl Roth, Germany
Zirconium oxide (Y-stabilized)	$(ZrO_2)_{0.91} - (Y_2O_3)_{0.09}$	> 99.7 %	Tosoh, Japan

3.2 Synthesis of Na-β″-alumina electrolytes

The synthesis of doped Na-β″-alumina electrolytes started by mixing AlO(OH), Na_2CO_3, and Li_2CO_3 according to the stoichiometry $Na_{1.67}Al_{10.67}Li_{0.33}O_{17}$. (Mixing using rotation beaker: 35 min^{-1}; rotation stirrer: 1100 min^{-1}; beaker inclination: 20 °; mixing time: 5 min; Eirich R02, Germany.) Afterward, the powder was calcined at 1280 °C for two hours in MgO crucibles and dis-agglomerated. The exact temperature regime can be found in the annex (Figure 57). The particle size distribution and an XRD pattern can be found in (annex Figure 56).

MnO_2 was oxidized to Mn_3O_4 (650 °C / 5 h) before using it as a dopant. The XRD pattern of Mn_3O_4 is displayed in Annex Figure 56. For synthesizing doped materials, as delivered, TiO_2, NiO, or the Mn_3O_4 were added to the synthesized Na-β″-alumina powder. When the doping amount is given in %, it relates to the mass fraction according to equation (6).

$$\omega \ [\%] = 100 \ \% \cdot \frac{m_{dopant}[g]}{m_{undoped \ powder}[g] + m_{dopant}[g]} \qquad (6)$$

The mole fraction was calculated by equation (7).

$$\chi = \frac{n_{dopant \ ions}}{n_{Na1.67Al10.67Li0.33O17} + n_{dopant \ ions}} \qquad (7)$$

The powder mixture was ball milled (Retsch PM 400, Germany) for 0.5 h at 200 rpm in 500 ml ZrO_2 beakers. The beakers were filled with 100 g powder mixture, 150 ml EtOH and 250 g of ZrO_2 milling balls (D = 0.5 cm). After milling, the powders were dried in a drying cabinet (*Thermo Fisher Scientific* FT 6060, USA) at 80 °C for 12 h. The dried powder was granulated by adding an aqueous binder solution during mixing (*Eirich* EL1, Germany) to the powder until fine granules were obtained. The granules were dried at 120 °C overnight. Afterwards the granules were pressed uniaxially with 110 kN (*Engelsdorf Sondermaschinenbau* TPA 16, Germany) into bars (5 mm x 5 mm x 50 mm) and discs (d = 2 cm, t = 0.15 cm) (Figure 17 a). The bars were cut into smaller pieces of 15 mm to 25 mm with a sharp knife in order to avoid deformation while sintering. The green bodies were then sintered in tailored MgO crucibles (Figure 17 b and c) at 1400 °C, 1500 °C, 1600 °C, or 1700 °C for 0.5 h. The exact sintering regime is in (Annex Figure 58). An overview of the samples produced is given in Table 2.
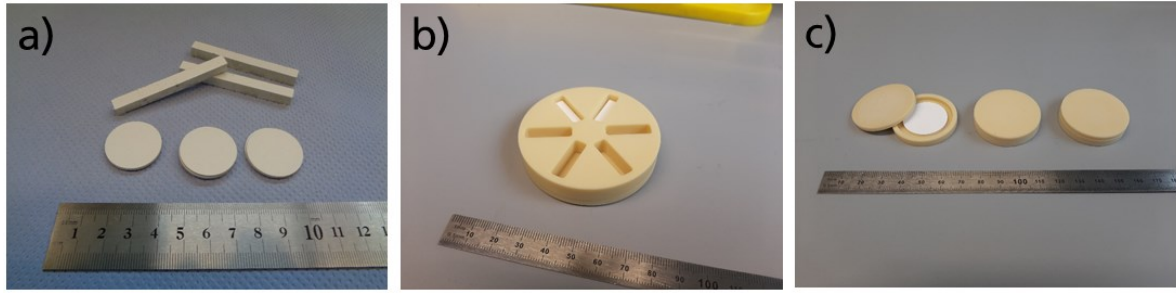
Figure 17. (a) green Na-β″-alumina electrolytes. (b) green Na-β″-alumina electrolyte bars in a MgO-crucible. (c) green Na-β″-alumina electrolyte disks in MgO crucibles.

Table 2. Overview of all tested dopants, doping amounts, and sintering temperatures to produce Na-β″-alumina electrolyte within the present work.

Doping amount (mass fraction)	Dopant: TiO_2			Dopant: Mn_3O_4			Dopant: NiO		
	Applied sintering temperature / °C								
0.0 %	1500	1600	1700	1500	1600	1700	1500	1600	1700
0.5 %	1500	1600	1700	1500	1600	1700	1500	1600	1700
1.0 %	1500	1600	1700	1500	1600	1700	1500	1600	1700
1.5 %	1500	1600	1700	1500	1600	1700	1500	1600	1700
2.0 %	1500	1600	1700	1500	1600	1700	1500	1600	1700
2.5 %	1500	1600	1700	1500	1600	1700	1500	1600	1700
5.0 %	1500	1600	1700	1500	1600	1700	1500	1600	1700

3.3   Applied characterization and analysis methods

XRD patterns were measured from disks that had been ground (D8 Advance, *Bruker*, USA) with CuKα radiation. The quantitative XRD evaluation was performed by the *Rietveld* refinement method (Autoquan 2.8.0.2, XRD *Eigenmann GmbH*, Germany).

Density analysis was carried out via *Archimede's principle* in toluene according to equation (8). The temperature of the toluene, and therefore the exact density, was measured by a manual alcohol thermometer.

$$\rho_{Sample} = \frac{m_{sample}}{m_{sample} - m_{sample\ in\ Toluene}} \cdot \rho_{Toluene} \tag{8}$$

The **absolute density** was measured from grounded samples by a He-Pycnometer (*Thermo Fisher* Pyknomatik-ATC, USA).

Fractured samples were used to take SEM images (Ultra 55+, Carl Zeiss, Germany). **SEM-EDX**-scans (Ultra 55+, *Carl Zeiss*, Germany/ Trident XM4, EDAX, USA) were taken from polished and thermally etched samples. The acceleration voltage for the secondary electrons and the backscattered electrons measurement mode was set to 15 kV. Before the measurement, all samples were coated with carbon (Leica MED20, Germany). The software *Lince* estimated the grain size (Lince 2.4.2, *TU Darmstadt*, Germany).

The **particle size** of the Na-β''-alumina powder was measured by laser diffraction (LS 13, *Beckman Coulter*, USA)

The **XPS** (X-ray photoelectron spectroscopy) measurement (Axis Ultra DLD, *Kratos Analytical Ltd*, Great Britain) was carried out by Al-K$_\alpha$-radiation. The software "CasaXPS 2.3.14" (Casa Software Ltd., Great Britain) was used to process the data.

The amount of Na-ions in the conduction slab was determined by converting Na-β''-alumina to Ag-β''-alumina. This happed by heating the samples to 260 °C in an AgNO$_3$ melt for 48 h. The number of Na-ions in the undoped sample was calculated according to equation (9). The procedure was derived from *Bay et al*. [33]

$$n(Na) = \frac{\Delta m}{\Delta M} = \frac{m_{Na-\beta''-alumina} - m_{Ag-\beta''-alumina}}{M_{Na} - M_{Ag}} \tag{9}$$

The **characteristic fracture strength** was determined on ten sintered tablets per doping level by the ball-on-three-balls method (Zwick 100, *Zwick*, Germany). The load increase speed was set to 5 N s^{-1}. The data were evaluated by *Weibull* statistics (maximum likelihood estimation) according to *Danzer et al.* [140] The *Weibull* distribution function is given in equation (10). [140] Where σ_0 is the characteristic fracture strength, σ_s is the fracture strength, V is the volume, V_0 is the normalized volume, and "m" is the modulus that describes the scatter of the measurement. A high value corresponds to a narrow distribution.

$$F(\sigma, V) = 1 - \exp\left[-\frac{V}{V_0}\left(\frac{\sigma_s}{\sigma_0}\right)^m\right] \tag{10}$$

DSC measurements (TDSC404, *Netzsch,* Germany) were performed on fragments of pre-sintered disks under N$_2$-atmosphäre at a heating rate of 20 K min^{-1}.

The **ionic conductivity** was measured by impedance spectroscopy (SP-240, *Biologic*, France and Reference 3000 AE, *Gamry*, USA). The sine wave amplitude was set to 10 mV, and the frequency range was 1 MHz to 9 Hz. The bar-shaped electrolyte samples were clamped in a sample holder (Figure 18). A glass wool pad (infiltrated with a eutectic mixture of KNO_3, $NaNO_3$, and $NaNO_2$) was used to ensure a proper connection between the sample and the sample holder. The measurements were performed in a drying cabinet to ensure a constant temperature.
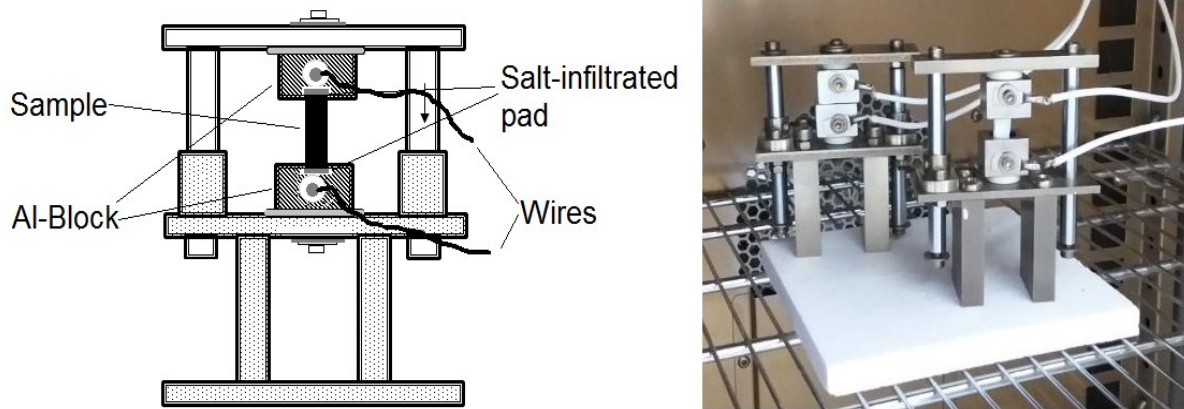
Figure 18. Sketch (left) and photograph (right) of the sample holder used for ionic conductivity measurements. Reprinted with permission from *Dirksen et al.* [64]

The Nyquist plot of the data recorded was fitted with the equivalent circuit (Figure 19), which other researchers also use to determine the ionic conductivity of Na-β''-alumina. [16,122,141] The fit provided the values for the bulk resistance (R_b) and the grain boundary resistance (R_{gb}), which were summed up (Equation (11)) to the resistance (R) of the sample. The constant phase element Q_1 represents the double layer capacitance of the grain boundaries, while Q_2 describes low-frequency regions of the Nyquist plot. It is mainly equivalent to the diffusion processes of an electrical system and not addressed further here.

$$R = R_b + R_{gb} \tag{11}$$

The resistance was used to calculate the ionic conductivity (σ) of the sample according to equation (12). The geometric parameters l (length) and A_{cs} (cross-sectional area) of the samples were measured using calipers.

$$\sigma = \frac{L}{A_{cs} \cdot R} \tag{12}$$

43

In addition to calculating the ionic conductivity, the specific grain boundary resistance (R_{sgb}) was also calculated. This quantity was given by equation (13).

$$R_{sgb} = \frac{A_{cs} \cdot R_{gb}}{L} \tag{13}$$

The temperature dependence of the ionic conductivity was described by the Arrhenius-type equation (equation 14).

$$\sigma = \frac{A}{T} \cdot exp^{\frac{-E_a}{T \cdot k_B}} \tag{14}$$
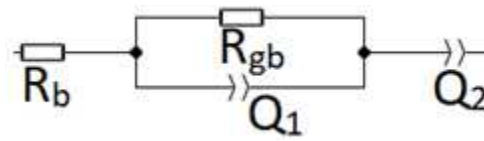
Figure 19. Equivalent circuit used for fitting the Nyquist plot.

3.4   Na/NiCl$_2$ cell assembly and test procedures

To test Na-β″-alumina electrolytes, a flat Na/NiCl$_2$-cell setup (Figure 20) was designed, manufactured, and utilized. The different components and an assembled cell are shown in Figure 21.
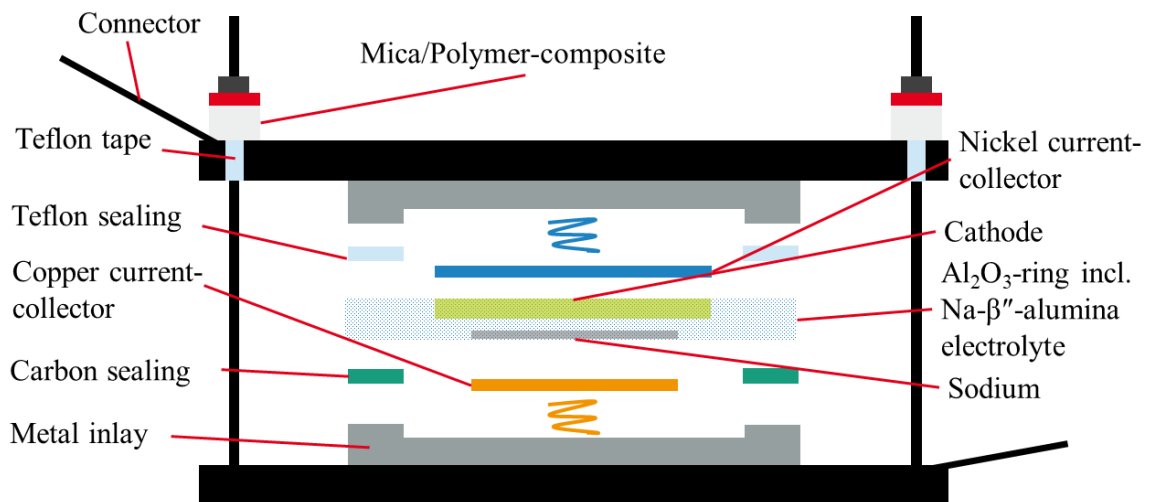
Figure 20. Sketch of a Na/NiCl$_2$-flat cell used to test Na-β″-alumina electrolytes.
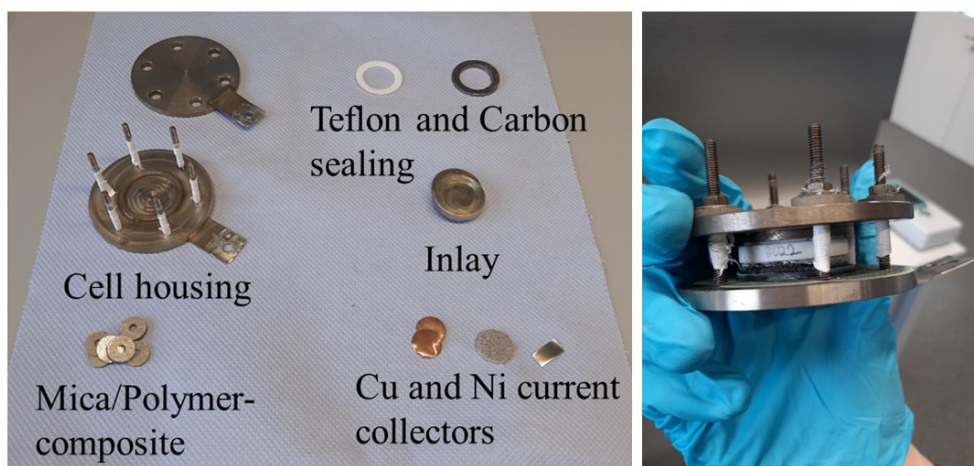
Figure 21. Cell components and an assembled flat Na/NiCl$_2$-cell.

The cell housing consists of a bottom and a top plate. Both are made from stainless steel and have a connector lug. The bottom plate serves as a negative terminal, while the top plate serves as a positive terminal. The threaded bolts on the bottom plate, used to close the cell, are wrapped with Teflon tape to avoid a short circuit. A mica/polymer composite ring isolated the top of the threaded bolts and the nuts. Ni-coated inlays protected the cell housing from corrosion.

Furthermore, the inlays have ripples to ensure the proper sealing of the cell. The galvanic nickel plating of the stainless-steel inlays was performed in two steps. At first, a thin layer of about 1 µm was applied by nickel-strike, followed by a thicker 20 µm layer by *Watt's* nickel. A Teflon® ring was used to seal the cathode chamber, while a carbon ring sealed the anode chamber.

The disk-shaped Na-β″-alumina electrolyte was joined to an Al$_2$O$_3$-ring (Figure 22) using glass solder to form a ceramic sub-assembly. The solder paste was prepared by mixing terpineol and glass powder (*Schott*, Germany) in a mass ratio of 2:5. The glass/terpineol mixture was applied between the electrolyte and the Al$_2$O$_3$-ring. Subsequently, the components were heated to 960 °C for three hours to seal correctly. The quality was checked by a He-leak detector (SmartTest, *Pfeiffer Vacuum*, Germany).

Afterwards, the negative electrode site of the electrolyte was coated with a carbon paste in order to obtain a high sodium wettability of the electrolyte. The carbon paste consists of acetone, water, carbon, and sodium phosphate.
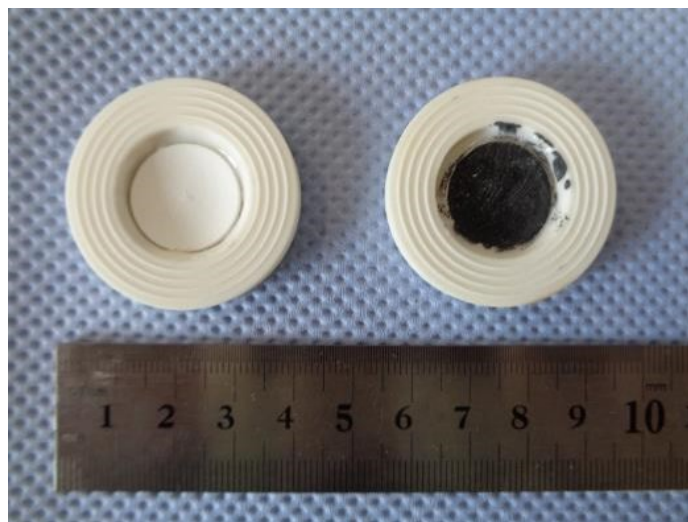
Figure 22. Al_2O_3-Ring with Na-β″-alumina electrolyte. Left: Without coating. Right: With carbon coating.

While assembling the Na/NiCl$_2$-cell under N$_2$-atmosphere, 0.25 g of sodium was placed in the anode chamber to ensure a proper electrical connection between the electrolyte and the current collector. Before closing the cell, the cathode chamber was filled with 1 g cathode granules and 1 g NaAlCl$_4$ powder. The same cell setup was used for tests on Na/Na-cells, but the cathode chamber was also filled with 0.25 g Na.

The cathode for Na/NiCl$_2$-cells was produced by granulating (RCC 100x20, *Powtec*, Germany) a mixture of Ni, NaCl, and small amounts of Al, NaBr, NaI, and FeS. The granules were sieved to separate the granules from the remaining powder (> 500 µm). NaAlCl$_4$ was synthesized by heating NaCl and AlCl$_3$ in the molar ratio 1.05:1 to 150 °C for one hour under an N$_2$-atmosphere.

The cell was heated to 300 °C and initialized by applying the following process:

1. Charging with 5 mA (corresponds to a current density of 2.83 mA cm^{-2}) for 30 min
2. Charging with 10 mA (corresponds to a current density of 5.66 mA cm^{-2}) until a voltage of 2.65 V was reached
3. Discharging with 10 mA until 20 % of the charged capacity was reached

The SoC (State of charge) of 100 % was defined as 80 % of the total capacity charged in step 1 and step 2. The subsequent cell cycling was carried out according to the following regime:

1. Charging with 10 mA to 100 % SoC
2. Discharging with different cycling rates until a voltage of 2.4 V was reached
3. Start at 1. again

The *PC* (*Peukert* constant) was calculated using equation (15). C_n is the cell capacity measured by applying the minimal discharge current I_n. I_{n1} is the discharge current on which the PC is measured. C_{n1} is the resulting capacity. [142]

$$PC = \left(\log_{\frac{I_n}{I_{n1}}} \frac{C_{n1}}{C_n} \right) + 1 \tag{15}$$

3.5 Synthesis and characterization of bilayer electrolytes

The porous bulk material was obtained from the University of Leipzig. The synthesis was described by *Hoppe, Dirksen, et al.* [143]. The dense layer was applied to the porous bulk material via spin-coating (Spin 150i, *Polos*, Netherlands). The spinning regime is displayed in Table 3. The slurry was produced by ball milling (400 rpm; 20 min; 30 g of 3 mm-ZrO_2-milling balls) of 9.5 g Na-β″-alumina, 0.5 g TiO_2, 1.0 g ZrO_2, 14.75 mL deionized water, 0.8 g organic binder and 0.05 g Contraspum. After coating, the samples were dried overnight under ambient conditions. The dried samples were placed in a dense MgO-crucible with the coated layer facing upwards. A thin layer of Na-β″-alumina powder was added to the bottom of the crucibles to avoid shrinkage and deformation of the electrolytes during heat treatment. Sintering was performed at 1400 °C for 2 h. To guarantee a dense layer, the procedure was repeated three times. The impermeability of the dense layer was checked by a He-leak detector.

The cell construction with bilayer electrolytes was carried out as described in Chapter 3.4.

Table 3. Spinning regime used to coat porous bulks with a Na-β″-alumina slurry.

Step-No.	Function	Rotation speed / rpm	Duration / sec
1	check position	200	10
2	deposition of slurry	800	5.0
3	Spinning	2000	30
4	Drying	800	20

Since the analytical characterization of the bilayer electrolytes differs slightly from the one applied to the electrolytes used in the doping experiments (described in chapter 3.2 and chapter 3.3), the applied analytics are described in this chapter. The SEM (Ultra 55 plus, *Carl Zeiss*, Germany) and EDX (XM14, *EDAX Trident*, Germany) images of the bilayer

electrolyte were recorded after embedding it in epoxy resin and subsequent polishing. The porosity was measured via mercury intrusion (PASCAL 440, *ThermoScientific/POROTEC*, USA) at up to 400 MPa at room temperature. To measure the ionic conductivity, the sintered bilayer electrolyte was attached to an Al_2O_3-cylinder (similar to the one in Figure 22) by a glass joining. The dense layer and the glass joint of the electrolyte sub-assembly were considered gas-tight if the leakage rate was below 1×10^{-7} mbar·L·s^{-1} (Smart Test, *Pfeiffer Vacuum*, Germany). Na was applied on the carbon-coated dense side, while the porous side was infiltrated with $NaAlCl_4$ at 300 °C. Both electrolyte sides were contacted with a Cu sheet. The test cell (same as in Figure 21, but without active material) was sealed with a Teflon® ring ($NaAlCl_4$-side) and a carbon ring (Na-side). The ohmic resistance was measured by impedance spectroscopy (SP-240, *Biologic*, France) from 1 MHz to 10 Hz and sine wave amplitude of 10 mV at temperatures from 165 °C to 300 °C. The cell assembly and measurements took place under an N_2 atmosphere. The impedance data were recorded and processed with the software "EC-Labs 11.3". Equation (12) was used to calculate the specific ohmic conductivity of the electrolyte (σ). As length, the overall thickness (bulk + dense layer) electrolyte was used.

4. Results and Discussion

This chapter discusses the properties of ceramic Na-β″-alumina electrolytes doped with TiO_2, Mn_3O_4, or NiO in comparison to each other and to undoped Na-β″-alumina electrolytes. It also presents practical examples of such electrolytes. Different doping levels and dopants were tested as well as different sintering temperatures (Table 2). First, techniques like XRD or EDX (Energy-dispersive X-ray spectroscopy) were carried out to evaluate the influence of 3d transition metal oxides on phase content, lattice parameters, and sintering mechanisms. Second, the electrolytes were characterized in respect of performance-relevant material properties such as characteristic fracture strength or ionic conductivity. The chapter concludes with two demonstration examples for TiO_2 doped Na-β″-alumina electrolytes.

4.1 Elucidating of transition metal doping mechanisms in Na-β″-alumina

After Na-β″-alumina has been doped with transition metal ions, it is necessary to clarify whether the Na-β″-alumina crystal phase is still present. Furthermore, it is from interest whether the dopant entered the crystal lattice or formed a secondary phase. Several analytical methods were used for these clarifications. XRD measurements were made to evaluate the Na-β″-alumina phase content, observe possible secondary crystal phases, and measure change in the lattice constants. EDX, XPS, and DSC (Differential thermal calorimetry) were used as support. EDX mapping is also able to detect secondary phases and their chemical composition, while XPS determines the oxidation state of the dopant ions. DSC enables the recording of the melting or crystallization enthalpies and processes that would be present if a liquid-assisted sintering process takes place as suggested by previous researchers. It should be noted that in chapter 4, all dopant amounts are given in percentage of the mass fraction.

4.1.1 Phase formation in Na-β″-alumina with transition metal doping

Undoped Na-β″-alumina

Before evaluating the effects of transition metal oxide doping, I recorded the XRD patterns of undoped Na-β″-alumina electrolytes (Figure 23) and the Na-β″-alumina phase content after sintering at three different temperatures. The peaks measured for all three samples match the literature peaks of Na-β″-alumina (pdf 84-1715, red bars at the bottom of Figure

23). The main impurity visible in the diffractograms is NaAlO$_2$, with peaks at 30.2° and 33.6°. By *Rietveld* refinement, it was possible to confirm a Na-β″-alumina phase content of > 95 % for all three samples. The main difference between the diffractograms is the increasing relative intensity of the peak 006 at 15.8°. *Li et al.* [71] and *Yi et al.* [120] found the same phenomenon and explained it by the anisotropic growth of Na-β″-alumina crystals at high sintering temperatures. I confirmed the anisotropic grain growth with SEM images (see chapter 4.2).
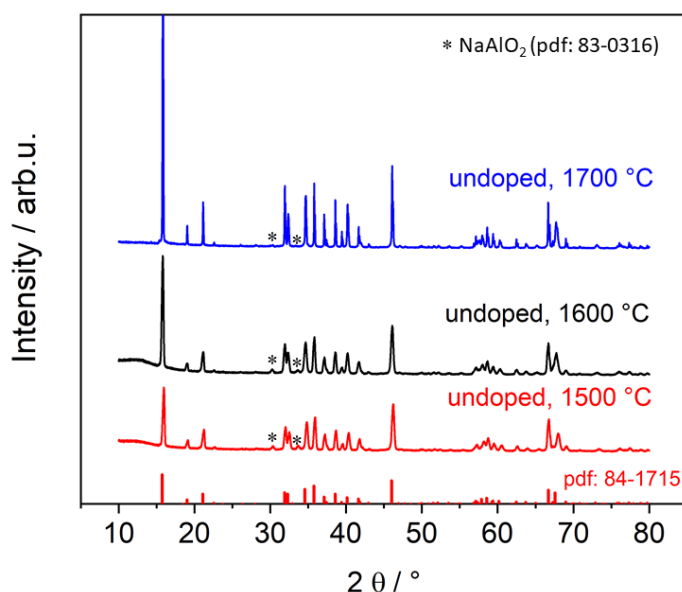
Figure 23. Diffraction patterns of undoped Na-β″-alumina sintered at 1500 °C, 1600 °C, or 1700 °C. The red bars at the bottom illustrate the literature peaks of Na-β″-alumina (pdf: 84-1715). The peak 006 (15.8°) is clipped off. Reprinted with permission from *Dirksen et al.* [86]

TiO$_2$ doped Na-β″-alumina

A selection of XRD patterns recorded from TiO$_2$ doped Na-β″-alumina is displayed in Figure 24 , while a complete overview is given in the appendix Figure 59.

Samples sintered at 1500 °C or 1600 °C and doped with a mass fraction of 2.5 % TiO$_2$ or less showed no phases other than those present in the undoped samples. Furthermore, the Na-β″-alumina phase content rose to around 95 % for all samples, independent of doping amount or sintering temperature (see

Table *4*). An increased mass fraction of 5.0 % TiO$_2$ or the application of higher sintering temperatures led to additional peaks that were possibly due to the formation of secondary phases, such as NaLiTi$_3$O$_7$ and Na$_{1.97}$Al$_{1.82}$Ti$_{6.15}$O$_{16}$. Typical peaks are shown by the XRD pattern of a sample doped with a mass fraction of 1.5 % TiO$_2$ and a sintering temperature

of 1700 °C, as well as by that of a sample doped with a mass fraction of 5.0 % and a sintering temperature of 1600 °C (Figure 24 a). Two fingerprint sections of XRD patterns, one with and one without the additional crystal phases, are shown in detail in Figure 24 b.

Previous work reported slightly different effects of TiO$_2$ doping on Na-β″-alumina electrolytes. *Yi et al.* [120] found a reduced Na-β″-alumina phase content of their magnesium stabilized electrolytes regardless of the doping amount. *Wei et al.* [28] also found an increase of the magnesium stabilized Na-β″-alumina phase content of 1.9 % by adding a mass fraction of 1.75 % TiO$_2$. *Yang et al.* [27] increased the phase content from 83 % to 92 % by adding a mass fraction of 1.0 % TiO$_2$.

Comparing the reported and present results, it can be stated that the influence of TiO$_2$ doping on the phase content was not fully understood and depends strongly on the synthesis route and the Na-β″-alumina phase content of the undoped material. There is as yet no literature showing formation of crystal phases similar to NaLiTi$_3$O$_7$ or Na$_{1.97}$Al$_{1.82}$Ti$_{6.15}$O$_{16}$. [27,118,121,124] Nevertheless, the results presented here align with those of other researchers. This is valid for the common experimental frame that was applied. The broadening of the experimental conditions by applying sintering temperatures as high as 1700 °C or doping amounts with mass fractions as high as 5.0 % TiO$_2$ enabled clarification of the TiO$_2$ doping mechanism.

Compounds with compositions like NaLiTi$_3$O$_7$ or Na$_{1.97}$Al$_{1.82}$Ti$_{6.15}$O$_{16}$ are also present after low sintering temperatures, as shown by EDX mapping in chapter 4.1.3. Possible mechanisms that are able to hinder detection by XRD are an insufficient crystalline fraction or tiny crystallites that lead to very broad and hardly detectable peaks.
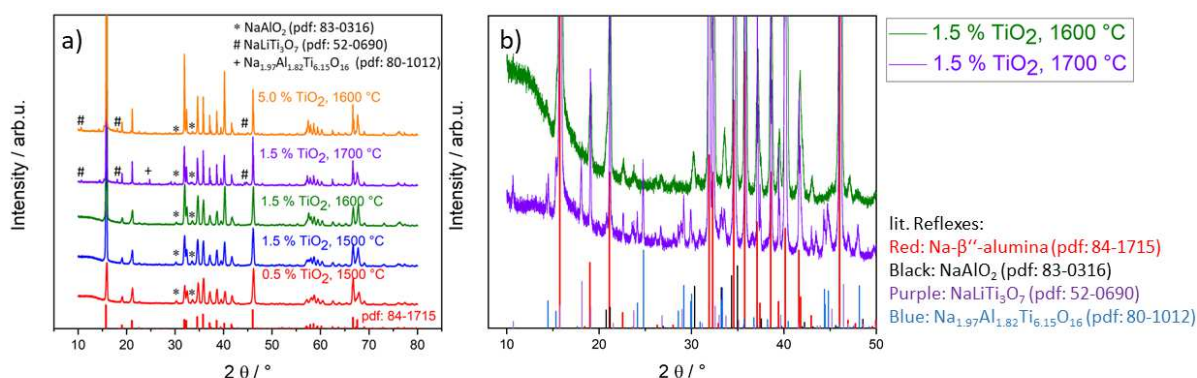
Figure 24. a) Diffraction patterns of TiO$_2$ doped Na-β″-alumina samples. The peak 006 (15.9°) is clipped off. Percentages indicate mass fractions. The literature peaks at the bottom are taken from pdf: 84-1715. b) XRD

fingerprint of two TiO_2 doped Na-β″-alumina samples with Na-β″-alumina literature peaks at the bottom. Reprinted with permission from *Dirksen et al*. [86]

Table 4. Na-β″-alumina phase content of the crystalline fraction of TiO_2 doped and differently sintered Na-β″-alumina electrolytes. Percentages indicate mass fractions. Reprinted with permission from *Dirksen et al.* [86]

Doping amount / %	Na-β″-alumina Phase content of TiO_2 doped electrolytes / %		
	1500 °C	1600 °C	1700 °C
0.0	95.6 ± 0.8	96.3 ± 0.5	95.5 ± 1.7
0.5	96.4 ± 0.4	96.6 ± 0.4	96.2 ± 0.3
1.0	96.8 ± 0.5	96.4 ± 0.4	98.0 ± 0.4
1.5	95.5 ± 0.5	94.0 ± 0.6	94.1 ± 1.0
2.0	96.3 ± 0.8	95.9 ± 0.5	90.8 ± 0.6
2.5	94.8 ± 0.5	95.3 ± 0.2	96.7 ± 0.8
5.0	96.6 ± 1.1	92.5 ± 0.3	94.2 ± 1.7

Mn_3O_4 and NiO doped Na-β″-alumina

In contrast to TiO_2 doped samples, samples doped with Mn_3O_4 or NiO revealed no secondary phases other than those occurring in undoped samples ($NaAlO_2$ and Na-β-alumina), regardless of the doping amount or sintering temperature. Some examples of diffraction patterns are displayed in Figure 25. The diffraction patterns for other sintering temperatures and doping amounts are displayed in appendix Figure 60 and Figure 61. The Na-β″-alumina phase content of the different samples is listed in Table 5 and Table 6. These data indicate that the Na-β″-alumina phase content is not dependent on the sintering temperature or doping amount. It hovers around 95 %. The sintering regime is most certainly able to explain this observation because it includes a two-hour temperature plateau at 1400 °C after the peak temperature (The whole sintering regime is shown in the appendix Figure 58). During these two hours, the phase contents of the samples sintered at different peak temperatures equilibrate to similar values. The plateau at 1400 °C guarantees a high Na-β″-alumina phase content. [141,144,145]

While no literature comparison exists for Mn^{2+} or Mn^{3+} doping, *Zhu et al.* [116] increased the Na-β″-alumina phase content of their samples from 92.3 % to a maximum of 98.9 % by

the addition of a mass fraction of 0.25 % NiO. In contrast to the present work, they used the intensity relation of a Na-β″-alumina peak and a Na-β-alumina peak to calculate the phase content. However, they did not consider phases such as Al_2O_3 or $NaAlO_2$.
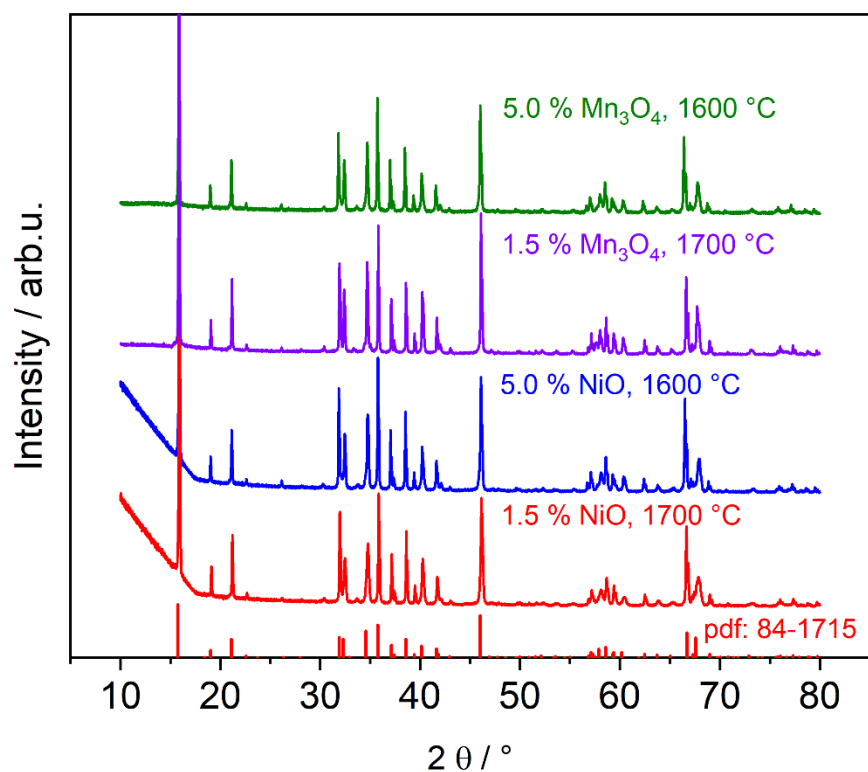
Figure 25. Diffraction patterns of Mn_3O_4 doped Na-β″-alumina. The peak 006 (15.9°) is clipped off. Percentages indicate mass fractions. The red bars at the bottom illustrate the literature peaks of Na-β″-alumina (pdf: 84-1715). Reprinted with permission from *Dirksen et al.* [86]

Table 5. Na-β''-alumina phase content of the crystalline fraction of Mn_3O_4 doped and differently sintered Na-β''-alumina electrolytes. Percentages indicate mass fractions. Results for sintering temperatures of 1500 °C, 1600 °C, and 1700 °C are reprinted with permission from *Dirksen et al.* [86]

Doping amount / %	Na-β''-alumina phase content of Mn_3O_4 doped electrolytes / %		
	1500 °C	1600 °C	1700 °C
0.0	95.6 ± 0.8	96.3 ± 0.5	95.5 ± 1.7
0.5	94.9 ± 0.2	94.9 ± 0.3	93.8 ± 3.6
1.0	94.4 ± 1.5	94.1 ± 4.1	94.4 ± 1.0
1.5	96.8 ± 0.3	95.7 ± 0.5	95.3 ± 1.0
2.0	94.3 ± 0.4	93.5 ± 0.3	95.6 ± 2.4
2.5	97.1 ± 0.3	95.2 ± 0.2	93.9 ± 2.1
5.0	95.4 ± 0.2	96.3 ± 0.5	95.5 ± 1.7

Table 6. Na-β''-alumina phase content of the crystalline fraction of NiO doped and differently sintered Na-β''-alumina electrolytes. Percentages indicate mass fractions. Results for sintering temperatures of 1500 °C, 1600 °C, and 1700 °C are reprinted with permission from *Dirksen et al.* [86]

Doping amount / %	Na-β''-alumina phase content of NiO doped electrolytes at different sintering temperatures / %		
	1500 °C	1600 °C	1700 °C
0.0	95.6 ± 0.8	96.3 ± 0.5	95.5 ± 1.7
0.5	95.2 ± 2.1	97.0 ± 0.1	94.6 ± 0.5
1.0	94.0 ± 0.5	96.3 ± 0.4	95.2 ± 0.5
1.5	93.8 ± 0.2	96.7 ± 1.5	96.7 ± 0.2
2.0	95.9 ± 0.4	94.8 ± 0.2	97.1 ± 0.5
2.5	95.7 ± 0.2	94.4 ± 0.2	96.8 ± 0.9
5.0	97.0 ± 0.1	95.5 ± 0.3	95.6 ± 1.2

4.1.2 Crystallographic lattice parameters and Na-content of doped Na-β″-alumina

The lattice parameters of the Na-β″-alumina crystal phase were calculated by the *Rietveld* refinement program "Autoquan" to find additional information about the possible incorporation of foreign ions into the crystal lattice. The number of Na-ions in the conduction slab was also measured via an ion exchange process because it affects the lattice parameters.

The lattice parameters calculated for the differently doped Na-β″-alumina samples sintered at 1600 °C are given in Figure 26. The results for different sintering temperatures showed the same tendency and are displayed in appendix Figure 62 and Figure 63.

The lattice parameters of TiO_2 doped samples do not depend on the amount of dopant. Parameter a (= b) is distributed around a mean of 0.5614 nm ± 0.0002 nm, the c parameter around 3.368 nm ± 0.002 nm. This finding hints that Ti-ions are not incorporated into the crystal lattice of Na-β″-alumina. To verify this claim and prove that the Ti-ions are only located in the secondary phases, EDX measurements were made (Chapter 4.1.3.).

The lattice parameters after Mn_3O_4 doping showed similar tendencies to NiO doping. The lattice parameter a (= b) increased from 0.5615 nm to 0.5630 nm in Mn_3O_4 doping and to 0.5623 nm in NiO doping at a doping amount of a mass fraction of 5.0 %. On the other hand, the lattice parameter c decreased from 3.3679 nm to 3.3571 nm in Mn_3O_4 doping and from 3.3679 nm to 3.3536 nm in NiO doping. Since Ni^{2+} and $Mn^{2+/3+}$ – regardless of their coordination – are larger than Al^{3+}, [146] it was expected that Al^{3+} substitution would enlarge all three crystal lattice parameters. The explanation for the reduction in the lattice parameter c was recently published by *Bay et al*. [33]. They demonstrated that the c-lattice parameter decreases by about 0.025 nm if the amount of Na^+ within the conduction slab is increased. However, the lattice parameter a (= b) is unaffected. This arises because of the increased electrostatic attraction between the positively charged conduction slab and the negatively charged spinel blocks. The same phenomenon possibly occurs after replacing Al^{3+} with Ni^{2+} or Mn^{2+}. To ensure charge neutrality, more Na-ions are located in the conduction slab. There is a similar relationship with CuO doped Na-β″-alumina. *Moghadam et al.* [126] showed that c-lattice parameter declines (from 3.355 nm to 3.325 nm) after the addition of a mole fraction of 2.5 % of CuO.

The lattice parameters calculated from samples sintered at 1500 °C and 1700 °C showed the same tendency as the ones after a sintering temperature of 1600 °C and are displayed in appendix Figure 62 and Figure 63. Only the sample with the highest doping amount and a sintering temperature of 1700 °C odds out and has a higher c-lattice parameter, than expected, while the a-lattice parameter is in line with the observations made after applying sintering regimes with lower temperatures.
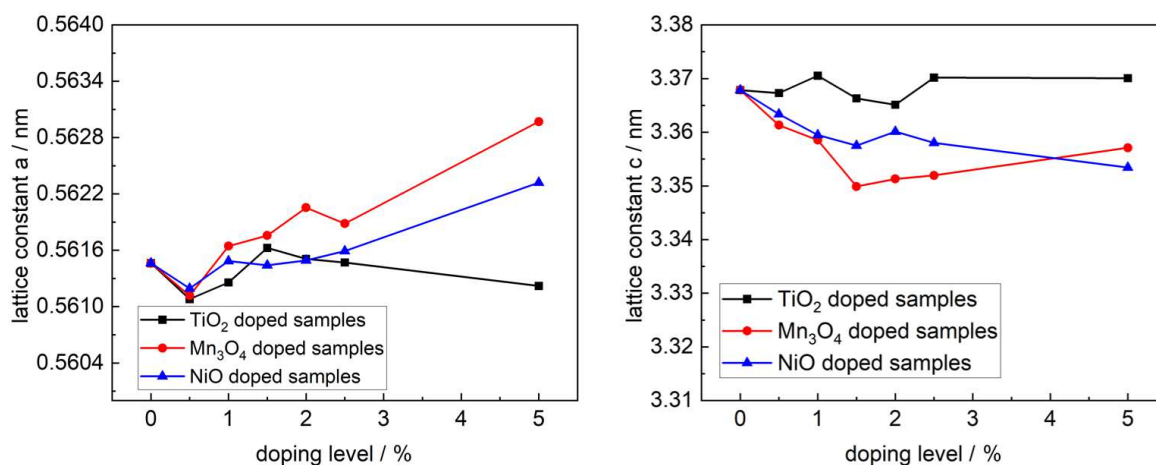
Figure 26. Crystallographic lattice parameters a (=b) and c of Na-β″-alumina samples sintered at 1600 °C. Percentages indicate mass fractions. Reprinted with permission from Dirksen *et al.* [86]

The number of Na-ions within the conduction slab was measured to further support this idea. The measurement was performed by converting the Na-β″-alumina into Ag-β″-alumina. In the transformation process in molten salt, the mobile Na-ions in the conduction slab are completely replaced by Ag-ions. [33] The number of Na-ions in the conduction slab is calculated by comparing the weight before and after ion transition. [33] The resulting Na-ion contents for samples (mass fraction of 2.5 % dopant) are shown in Table 7. The ratio between the exchanged sodium (measured) and the Al^{3+}-ions + dopant ions (calculated via stoichiometry) was used to compare the different samples. The Na/Al ratio was 0.157 based simply on the quantities of AlO(OH) and $NaCO_3$ is used while synthesizing the electrolyte. However, it was slightly less, at 0.144, based on the ion exchange technique. The deviation is probably caused by the secondary phases (mainly $NaAlO_2$), where no exchange of Na-ion with Ag-ion is expected. The TiO_2 doped sample had nearly the same ratio (0.141), which is in line with the suggestion that the Ti-ions are not incorporated into the crystal lattice and therefore do not influence the number of Na-ions in the conduction slab.

To evaluate the expected Na/(Al+Mn)-ratio change by Mn_3O_4 doping it is necessary to know the oxidation state of the Mn-ions. This is because it is possible that every Mn^{2+} incorporation results in one more Na-ion in the conduction slab but that Mn^{3+} incorporations do not.

XPS was used for this task. The XPS data is shown in appendix Figure 64. It revealed an Mn^{2+} to Mn^{3+} ratio of 26 % to 74 %. In consequence of this ratio, only about a quarter of the Mn-ions are expected to increase the Na-ion amount in the conduction slab. The expected Na/(Al+Mn)-ratio calculated amounted to 0.155 which matched the measured ratio of 0.156.

The expected ratio of 0.169 for the NiO doped samples is higher than that for Mn_3O_4 doped samples because the presence of Ni^{3+} is unexpected (Ni_2O_3 decomposes to 2 NiO and 0.5 O_2 at temperatures of about 600 °C [147]). However, the measured ratio was only 0.157. The reason for this gap is not entirely apparent. However, it is possible that the secondary crystal phases within the electrolyte, *e.g.,* $NaAlO_2$ is possibly also doped with Ni^{2+}-ions and thus influence the measurement and the expected value.

In addition to the unclear ratio of NiO doped samples, it can be concluded that the addition of TiO_2 did not lead to a distinctly changed amount of Na-ions in the conduction slab while Mn_3O_4 and NiO doping increased the number of Na-ions in the conduction slab. This is a conclusive reason for the reduced c-lattice parameter of the Na-β''-alumina crystal phase.

Table 7. Mass and Na-contents of samples used for the conversion from Na-β''-alumina to Ag-β''-alumina.

Sample name and theoretical composition	$m_{Na-\beta''-alumina}$ / g	Δm / g	Measured amount of Na / mol	n_{Na} / $n_{Al+Mn/Ni/Ti}$ [*]	Expected ratio [**]
Undoped sample ($Na_{1.67}Al_{10.67}Li_{0.33}O_{17}$)	1.160	0.251	0.00296	0.144	-
2.5 % TiO_2 ($Na_{1.63}Ti_{0.19}Al_{10.43}Li_{0.32}O_{17}$)	1.168	0.247	0.00291	0.141	-
2.5 % Mn_3O_4 ($Na_{1.65}Mn_{0.20}Al_{10.54}Li_{0.33}O_{17}$)	1.079	0.253	0.00298	0.156	0.155
2.5 % NiO ($Na_{1.65}Ni_{0.20}Al_{10.54}Li_{0.33}O_{17}$)	1.146	0.271	0.00350	0.157	0.169

[*] n_{Na} is the measured value, $n_{Al+Mn+Ni}$ is the value calculated from the reactant mixture, while synthesizing the electrolyte.

[**] The expected ratio, if every Ni^{2+}- and Mn^{2+}- ion resulted in one more Na-ion in the conduction slab, it was calculated by: $(n_{Na(undoped)} + n_{0.24Mn/Ni}) / (n_{Al} + n_{Mn/Ni})$, where $n_{Na(undoped)}$ represents the amount of Na the sample would have, if no dopant took influence.

4.1.3 Chemical analysis of transition metal doped Na-β''-alumina by EDX analysis

TiO_2 doped Na-β''-alumina

For further clarification of the whereabouts of the TiO_2, EDX measurements of polished electrolytes were performed. In this chapter, only the chemical compositions resulting from the spectra are discussed, while the changes in the microstructure are shown in chapter 4.2. An EDX mapping of samples doped with different amounts of TiO_2 and sintered at 1600 °C is shown in Figure 27. EDX mapping and a spot analysis of an undoped sample is in the appendix Figure 66 and Figure 67. The sample doped with a mass fraction of 0.5 % TiO_2 did not show any Ti-related EDX signals, neither in a mapping experiment Figure 27 a) nor in a spot measurement (appendix Figure 65). Figure 27 b) shows the element mapping of a sample doped with a mass fraction of 2.0 % TiO_2. The corresponding SEM image areas with fine grains (< 10 μm) accompanied by a brighter Ti-containing phase can be seen. The large grains with a diameter of > 20 μm were free of Ti. The Na-β''-alumina sample doped with a mass fraction of 5.0 % TiO_2 (Figure 27 c) features a clear phase separation between Ti-free, darker grains, and bright phases with a high Ti-content.
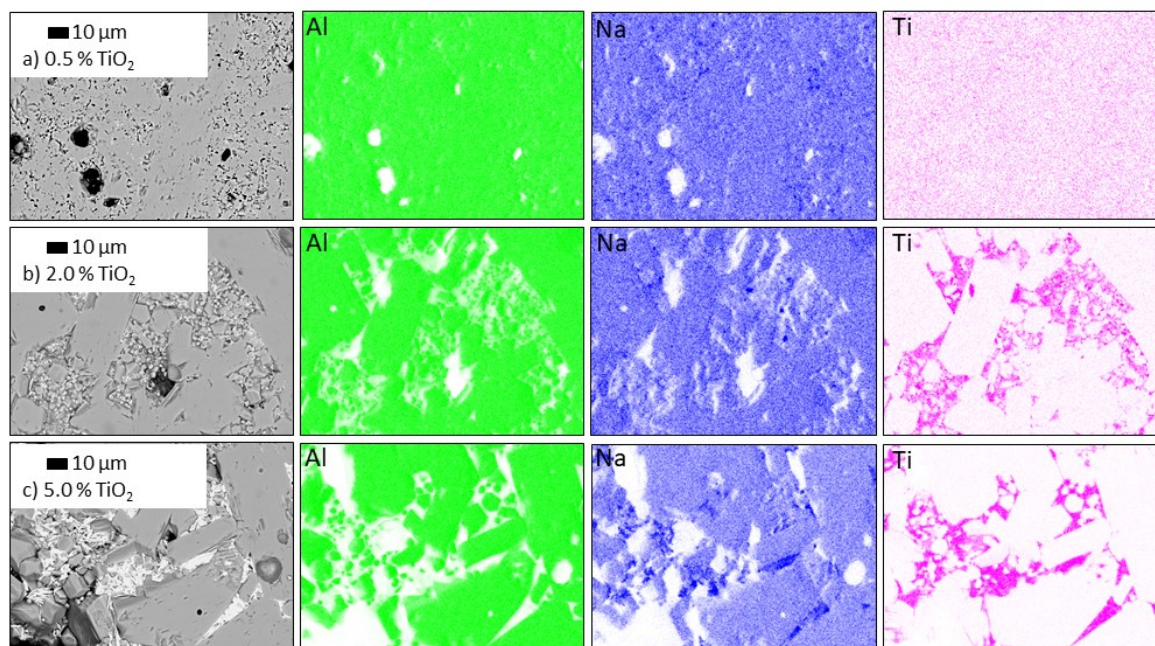
Figure 27. EDX mapping and backscattering SEM images of TiO_2 doped, polished Na-β″-alumina samples (sintered at 1600 °C). a) 0.5 % TiO_2 b) 2.0 % TiO_2 c) 5.0 % TiO_2. Al is labeled green; Na is labeled blue; Ti is labeled pink. Percentages indicate mass fractions. Reprinted with permission from *Dirksen et al.* [86]

Point-EDX-spectra taken from three different spots of the sample and a backscattering electron image of the area are shown in Figure 28. In a similar way to Figure 27 c), the SEM image confirmed the existence of dark grains (low mean atomic number) and bright areas (high mean atomic number). The quantitative evaluation revealed additional Ti as the main difference between the phases. The dark grains (Figure 28 spot X1) had a chemical composition of: $Na_{1.63}Al_{10.8}O_{17}$, which matches Na-β″-alumina, while the chemical composition of the bright phase was not uniform. Spot X2 is located at a bright needle-shaped area in Figure 28 and had the chemical composition: $Na_{3.4}Al_{3.9}Ti_{4.2}O_{16}$. Spot X3, located in another bright area, had the composition $Na_{2.0}Al_{0.1}Ti_{3.0}O_7$. These results support the idea that secondary phases are formed that contain Ti, yet not all of them contain Al. The compositions measured by EDX match the crystal phases identified by XRD, namely $NaLiTi_3O_7$ and $Na_{1.97}Al_{1.82}Ti_{6.15}O_{16}$. The EDX experiments furthermore confirm the absence of Ti in the Na-β″-alumina grains. It is thereby underlined that Ti-ions are not incorporated into the Na-β″-alumina crystal structure but form secondary phases.
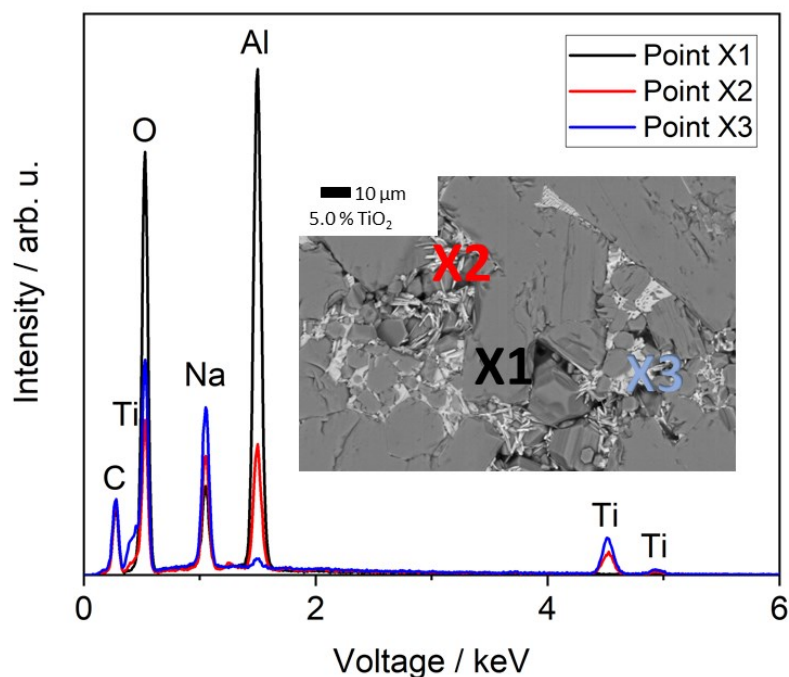
Figure 28. EDX point analysis of a Na-β″-alumina sample doped with 5.0 % TiO_2 (sintered at 1600 °C). The measuring points are marked in the backscattering SEM image. Percentages indicate mass fractions. Reprinted with permission from *Dirksen et al.* [86]

Mn_3O_4 and NiO doped Na-β″-alumina

After the TiO_2 doped samples, the Mn_3O_4 and NiO doped Na-β″-alumina samples were also scanned by EDX mapping. The mapping result for a Mn_3O_4 doped Na-β″-alumina sample is shown in Figure 29, and that for a NiO doped sample in Figure 30. The mapping experiments of both dopants showed, despite the high doping amount, no clear Mn or Ni signals over the mapped area (the pores visible in the Na- or Al-mapping are not visible in the Mn/Ni mapping experiments). Also undetected were the formation of Mn or Ni enriched regions or accumulation at grain boundaries. Accordingly, no dopant containing secondary phase was visible in the EDX experiments or the X-ray diffractograms. A point EDX of a Mn_3O_4 and NiO doped Na-β″-alumina sample is displayed in the appendix Figure 68 and appendix Figure 69. They showed a small peak ascribable to Mn (in the Mn_3O_4 doped sample) and to Ni (in the NiO doped sample) within the Na-β″-alumina grains.

These results, in addition to the change in lattice parameters, indicate that Mn- and Ni-ions are incorporated into the crystal lattice of the Na-β″-alumina crystal structure, as previous researchers assumed. [100,123]
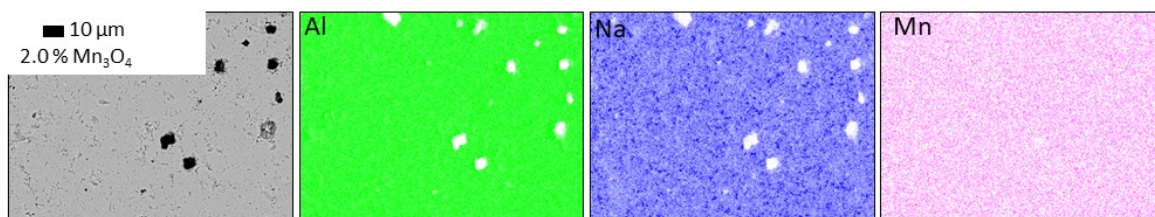
Figure 29. EDX mapping and backscattering-SEM image of Mn_3O_4 doped, polished Na-β″-alumina samples (sintered at 1600 °C). Al is labeled green; Na is labeled blue; Mn is labeled pink. Percentages indicate mass fractions. Reprinted with permission from *Dirksen et al.* [86]
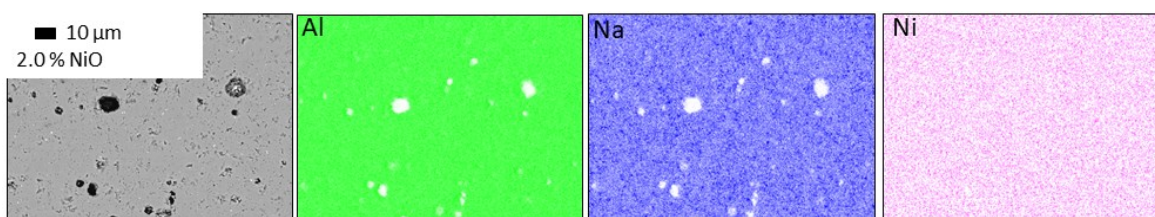
Figure 30. EDX mapping and backscattering-SEM image of NiO doped polished Na-β″-alumina samples (sintered at 1600 °C). Al is labeled green; Na is labeled blue; Ni is labeled pink. Percentages indicate mass fractions. Reprinted with permission from *Dirksen et al.* [86]

4.1.4 Thermal analysis of phase formation processes in transition metal doped Na-β″-alumina by DSC

DSC measurements were performed to prove the formation of a liquid phase, enabling liquid-assisted sintering while sintering TiO_2 doped samples. Figure 31 displays the results measured. The DSC-line of the TiO_2 doped Na-β″-alumina samples had a significant signal starting at a temperature of about 1050 °C, which indicates a melting process. The temperature was independent of the TiO_2 doping amount. The crystal phases found by XRD and similar compounds have melting points in a temperature range of 1000 °C to 1300 °C. [118,148] This finding indicates, that the compounds found by XRD are responsible for the observed melting process. A higher doping TiO_2 amount led to a larger endothermic peak, which can be explained by larger amounts of meltable Ti-containing substances as they were found in the XRD measurements.

This experiment proved, for the first time, liquid phase formation while sintering TiO_2 doped Na-β″-alumina.

To detect possible different or more Ti-containing liquid compounds forming at 1050 °C, it was also tried to quench the sintering process at 1200 °C by removing it from the hot oven. The resulting XRDs are shown in appendix Figure 71 and do not show any additional crystal phases.

The DSC measurements of undoped, Mn_3O_4 doped, and NiO doped samples did not indicate any liquid phase formation in that temperature range. They show a peak between 1550 °C and 1600 °C, which is typical for the sintering process of Na-β''-alumina and results from an eutectic point in the phase diagram Na_2O-Al_2O_3. [88,149] The TiO_2 doped samples do not show this peak which indicates, that the substance meltable at about 1550 °C dissolve in the already existing liquid phase and a clear melting temperature is not observable anymore. The phenomenon of solving was also described in chapter 2.5 as a typical procedure at liquid assisted sintering processes.
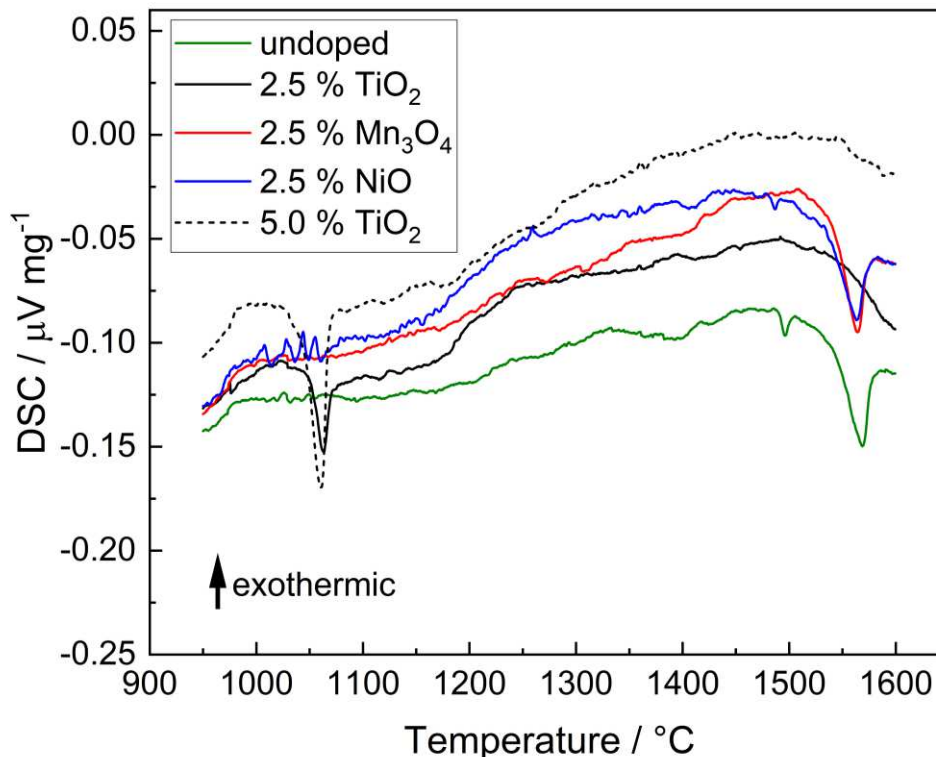
Figure 31. DSC scan of Na-β''-alumina samples doped with a mass fraction of 2.5 % TiO_2 (black line), 5.0 % TiO_2 (black dotted-line), 2.5 % Mn_3O_4 (red line), or 2.5 % NiO (blue line) in comparison to an undoped sample (green line).

Another attempt to estimate the effect and temperature range of the liquid phase formation of the secondary Ti-containing phases was made by polishing already sintered samples and heating them to different temperatures. The liquid phase spills over the polished surface if the temperature for liquid assisted sintering is reached and a sufficient amount of liquid phase is formed. Figure 32 a) and b) shows the surface of a sample doped with a mass fraction of 1.5 % TiO_2 after applying a temperature of 1500 °C. A liquid phase was visible spilled over the polished surface. A sample doped with Mn_3O_4 (Figure 32 c) showed no signs of a liquid phase. The polished surface remained clean if a lower temperature of only

1400 °C was applied to the TiO_2 doped sample (Figure 29 d). A temperature of 1400 °C is also insufficient to sinter and densify a TiO_2 doped Na-β″-alumina electrolyte *Dirksen et al.* [64]. Therefore, it can be concluded that temperatures of more than 1400 °C are necessary to enable a liquid-assisted sintering process, that results in a dense ceramic electrolyte. An EDX- analysis of the liquid phase (Figure 32) is shown in appendix Figure 70.
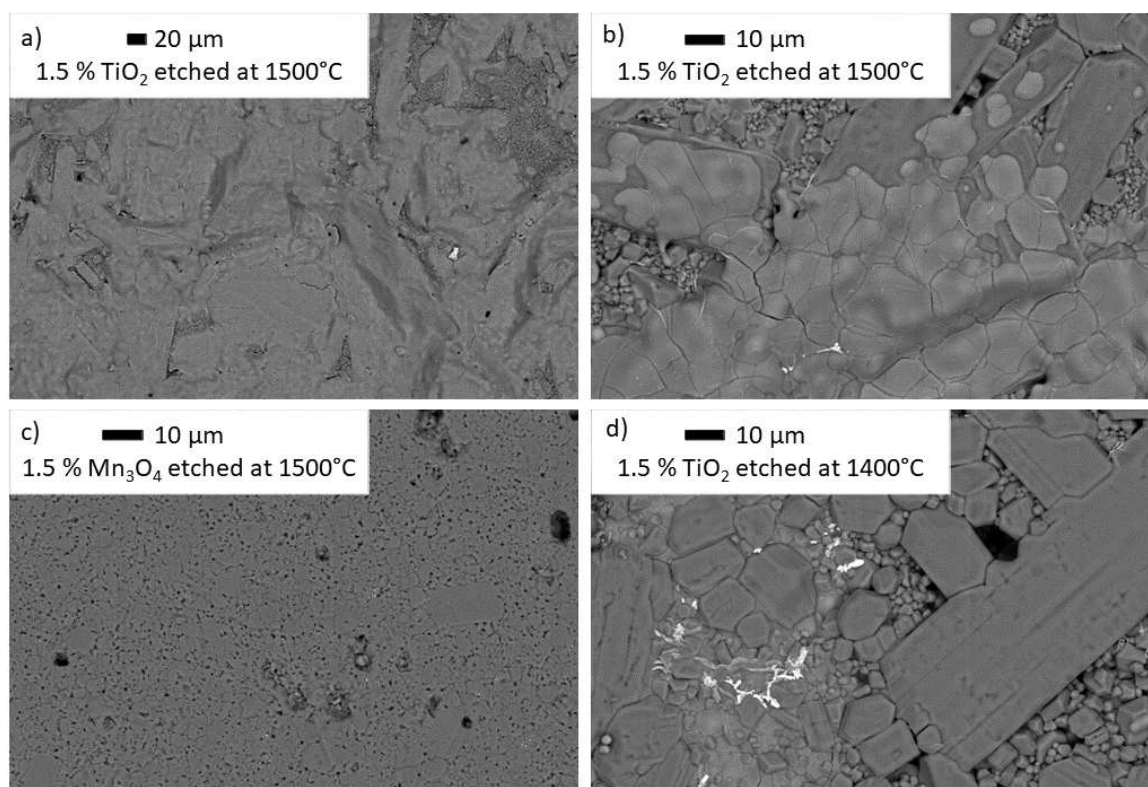
Figure 32. SEM images of polished and thermal etched Na-β″-alumina samples. a) and b) sample doped with a mass fraction of 1.5 % TiO_2 and an etching temperature of 1500 °C at two different magnifications c) sample doped with a mass fraction of 1.5 % Mn_3O_4 and an etching temperature of 1500 °C d) sample doped with a mass fraction of 1.5 % TiO_2 and an etching temperature of 1400 °C.

4.1.5 Interim résumé

XRD measurements revealed that regardless of the dopant (TiO_2, Mn_3O_4, or NiO), the doping amount and sintering temperature of the Na-β″-alumina phase content hovers around 95 %. The annealing step at 1400 °C after the sintering step possibly provides similar phase contents.

Furthermore, it was shown that TiO_2 doping results in the formation of additional phases such as $NaLiTi_3O_7$ or $Na_{1.97}Al_{1.82}Ti_{6.15}O_{16}$ that enable liquid-assisted sintering at temperatures higher than 1400 °C. EDX measurements found no Ti within the Na-β″-

alumina grains, nor did the lattice parameters of the Na-β″-alumina crystal phase show any changes. It is therefore concluded that Ti-ions are not integrated into the Na-β″-alumina crystal lattice and are not a classic dopant, but a sintering aid (nevertheless, the term "doping" will be used to avoid ambiguities).

Mn_3O_4 and NiO doping does not result in an additional melting process, and no doping-related secondary phases were found by XRD. A change of the lattice parameters of the Na-β″-alumina crystal phase and EDX measurements indicated that Mn- and Ni-ions are integrated into the Na-β″-alumina crystal lattice.

4.2 Impacts from transition metal doping of Na-β″-alumina to electrolyte-relevant material properties

The two parameters used to judge the performance of Na-β″-alumina electrolytes are first, the characteristic fracture strength and, second, the ionic conductivity. As outlined in chapter 1, a high characteristic fracture strength is vital for preventing failure during cell operation and allows the design of thin but stable electrolytes. The ionic conductivity is vital for minimizing cell resistance and so maximizing cell performance. As outlined in the following chapter, both of these performance parameters are strongly influenced by the microstructure of the Na-β″-alumina electrolyte.

4.2.1 Microstructural changes from transition metal doping of Na-β″-alumina

To evaluate the influence of the sintering temperature and the doping level on the microstructure of the Na-β″-alumina electrolytes, the relative density and thereby the porosity of the samples were measured. Low porosity is desirable in a Na-β″-alumina electrolyte because pores increase the conduction pathway for Na-ions and thus, increase the ohmic resistance of the solid electrolyte. Furthermore, pores reduce the fracture strength of ceramic compounds. SEM images were recorded to evaluate the microstructure grain size. Grain size plays an essential role in the ionic conductivity and the characteristic fracture strength of a Na-β″-alumina electrolyte. Small grains are desirable because they maximize the fracture strength of a ceramic [87], while large grains are desirable to maximize ionic conductivity by avoiding grain boundaries.

undoped Na-β″-alumina

The relative density of the undoped and TiO_2 doped samples is displayed in Figure 33. For the undoped material, the relative density dropped with an increasing sintering temperature from 98.6 % (3.16 g cm^{-3}) after sintering at 1500 °C to 93.1 % (2.98 g cm^{-3}) after sintering

at 1700 °C. The reason for this reduction is oversintering caused by pore agglomeration. This is a typical phenomenon of ceramics that were sintered at high temperatures [69]. Furthermore, increased sublimation of Na_2O (sublimating point 1275 °C [34]) is able to generate additional pores or prevent existing pores from closing during sintering (due to being trapped in those pores). [22] The increasing number of pores is also visible in the SEM images in Figure 34 a)-c). The SEM images also revealed a significant change of the microstructure between the sample sintered at 1500 °C and the samples sintered at 1600 °C or 1700 °C (additional SEM images with different magnifications are shown in appendix Figure 72). Low-temperature sintering resulted in a fine (mean grain diameter of 2.1 µm ± 0.7 µm) and homogenous grain structure. However, high sintering temperatures of 1600 °C and 1700 °C produced large and directionally and anisotropically grown grains with a length of up to 100 µm. As described in chapter 4.1.4, a liquid phase formation at temperatures of about 1550 °C is typical for Na-β″-alumina. The liquid phase (and the thereby enabled liquid assisted sintering) is causal for the distinct increase of the grain size at sintering temperatures of ≥ 1600 °C. This observation was already described by previous researchers. [149] The consequences of these microstructural changes on the performance parameters of the electrolyte are discussed in chapter 4.2.
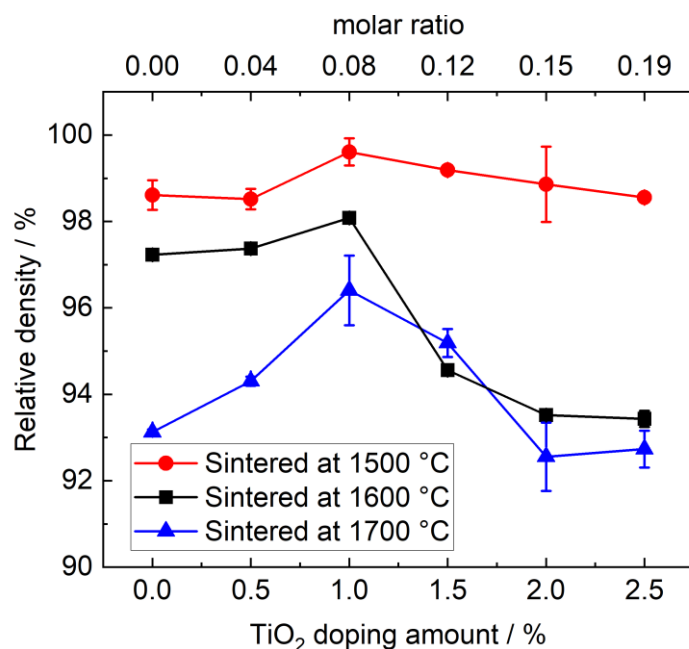
Figure 33. Relative density of TiO_2 doped Na-β″-alumina samples. Percentages indicate mass fractions. Reprinted with permission from *Dirksen et al.* [32]
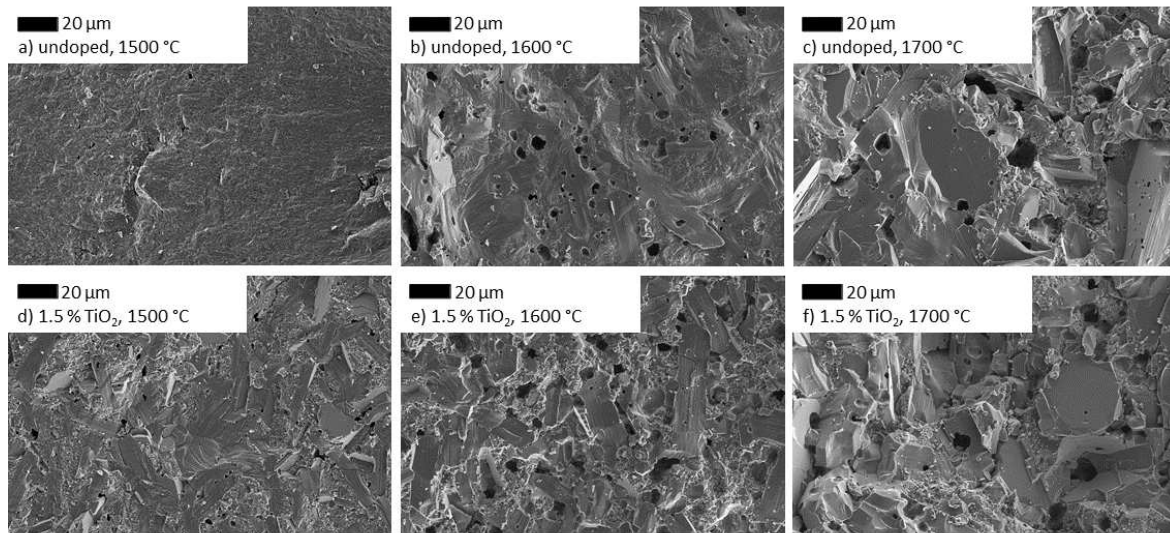
Figure 34. SEM images of Na-β″-alumina samples sintered at 1500 °C, 1600 °C, or 1700 °C; a)–c) undoped samples; d)–f) Na-β″-alumina doped with a mass fraction of 1.5 % TiO$_2$. Reprinted with permission from *Dirksen et al.* [32]

TiO$_2$ doped Na-β″-alumina

The influence of TiO$_2$ doping on the relative density at different sintering temperatures is shown in Figure 33. Samples of the SEM images obtained are shown in Figure 34 d)-f). As for the undoped samples, relative density of the TiO$_2$ doped Na-β″-alumina samples decreased with increasing sintering temperature. The increasing number and size of pores were also clearly visible in the SEM images Figure 34 d)-f). The increase is ascribable to the same phenomena as for the undoped samples. It is thus clear that sintering temperatures of 1600 °C or 1700 °C led to higher porosity and larger grains than the samples sintered at 1500 °C.

In addition to the sintering temperature, the TiO$_2$ doping amount also influenced the relative density and the grain size. Independently of the sintering temperature, the highest relative densities were reached using a doping amount of a mass fraction of 1.0 % TiO$_2$. The highest relative density of 99.6 % (3.14 g cm^{-3}) was reached at a sintering temperature of 1500 °C. The de facto absence of pores was also visible in the SEM image (Figure 35 c). Higher doping amounts reduced relative density at all three sintering temperatures due to an oversintering effect. This is a consequence of the liquid-assisted sintering process, which is intensified by high doping amounts, and enables oversintering and the pore agglomeration related to it at lower temperatures. This influence is clearly visible in Figure 35 which shows SEM images of samples with different doping levels but the same

66

sintering temperature of 1500 °C. Appendix Figure 73 to Figure 78 show additional SEM images of different sintering temperatures and doping levels.

The microstructure of the undoped sample (Figure 35 a) and the sample doped with a mass fraction of 0.5 % TiO_2 (Figure 35 b) were dominated by homogenous fine grains. These grains were of mean grain size of 2.1 µm ± 0.7 µm and 2.7 µm ± 0.9 µm. The sample doped with a mass fraction of 1.0 % TiO_2 (Figure 35 c), however, showed typical indications of liquid-assisted sintering (see Chapter 2.5.). These indications include large idiomorphic grains in a matrix of small grains in addition to the fine grains that still dominate the microstructure, it is possible to see large directionally and anisotropically grown grains with a length of up to 30 µm. Using even higher doping amounts of mass fractions ≥ 1.5 % TiO_2 resulted in a microstructure dominated by large grains with diameters of up to 50 µm. The microstructure looked similar but less porous (higher relative density) to the microstructure of undoped samples at a sintering temperature of 1600 °C or 1700 °C. Thus, in summary, TiO_2 doping enables the formation of a microstructure dominated by large grains at low temperatures. Therefore, the relative density stays at the desired level of above 98 %, which was impossible at high sintering temperatures. At lower doping levels and a sintering temperature of 1500 °C, the fine grain structure remains, and the relative density is greater. There is widespread confirmation of doping with Ti-containing substances increasing the relative density of Na-β″-alumina. [27,28,120] *Yang et al.* [27], for example, increased the relative density of their Na-β″-alumina electrolytes from 92.8 % to 99.6 % by adding a mass fraction of 1.0 % TiO_2. However, in contrast to my work, former researchers did not investigate the influence of the sintering temperature.
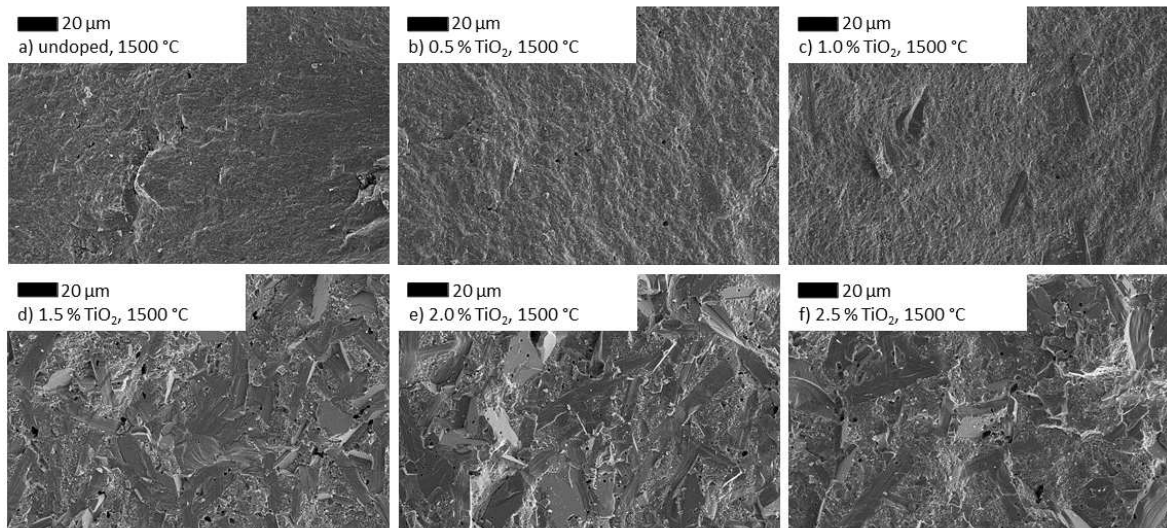
Figure 35. SEM images of Na-β″-alumina samples doped with different amounts of TiO_2 (b-f) in comparison to an undoped sample a). Percentages indicate mass fractions. Reprinted with permission from *Dirksen et al.* [86]

Mn_3O_4 and NiO doped Na-β″-alumina

The relative density of Mn_3O_4 doped samples at different sintering temperatures is shown in Figure 36 a). The relative density of samples sintered at 1500 °C decreased with increased doping amount. The relative density of the sample doped with a mass fraction of 0.5 % Mn_3O_4, for instance, dropped from 98.6 % / 3.16 g cm^{-3} to 96.0 % / 3.11 g cm^{-3}. Samples sintered at 1600 °C or 1700 °C showed no clear correlation between the relative density and the doping amount but the relative density again went down with a high sintering temperature of 1700 °C. The SEM images (Figure 37) confirmed this observation. The samples sintered at 1500 °C or 1600 °C showed fewer and smaller pores than those sintered at 1700 °C. In addition to the reduced number of pores, changes in the grain size become apparent. Mn_3O_4 doped samples sintered at 1500 °C or 1600 °C showed no signs of excessive grain growth but a fine-grained homogenous microstructure. Additional SEM images are presented in the appendix in Figure 80 to Figure 84. Figure 38 shows sample SEM images of polished and thermally etched surfaces of samples that were doped with a mass fraction of 1.5 % Mn_3O_4 and sintered at 1500 °C, 1600 °C, or 1700 °C. The mean grain size after sintering at 1500 °C amounted to 2.3 µm ± 0.6 µm. After sintering at 1600 °C, the grain size increased only slightly to 2.5 µm ± 0.6 µm.

A more significant microstructural modification of the microstructure was observed in the shape of the grains. While the sample sintered at 1500 °C showed flake-like grains, the

grains of the sample sintered at 1600 °C had a circular shape. High sintering temperatures of 1700 °C resulted in excessive grain growth independently of the doping amount.

It is possible to conclude that Mn_3O_4 doping hinders the sintering process and prevents grain growth at temperatures of 1600 °C while the relative density remained similar to that of an undoped sample. At sintering temperatures of 1500 °C, Mn_3O_4 doping reduces the relative density, which is another hint of reduced sinter activity due to the dopant.
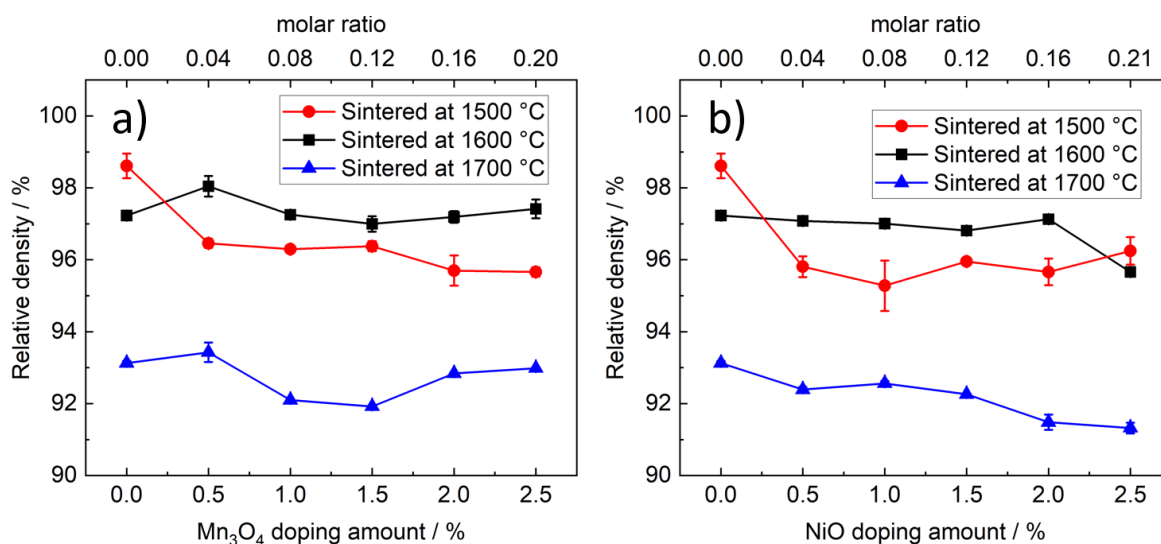
Figure 36. a) relative density of Mn_3O_4 doped Na-β″-alumina samples; b) relative density of NiO doped Na-β″-alumina samples. Percentages indicate mass fractions. Reprinted with permission from *Dirksen et al.* [86]
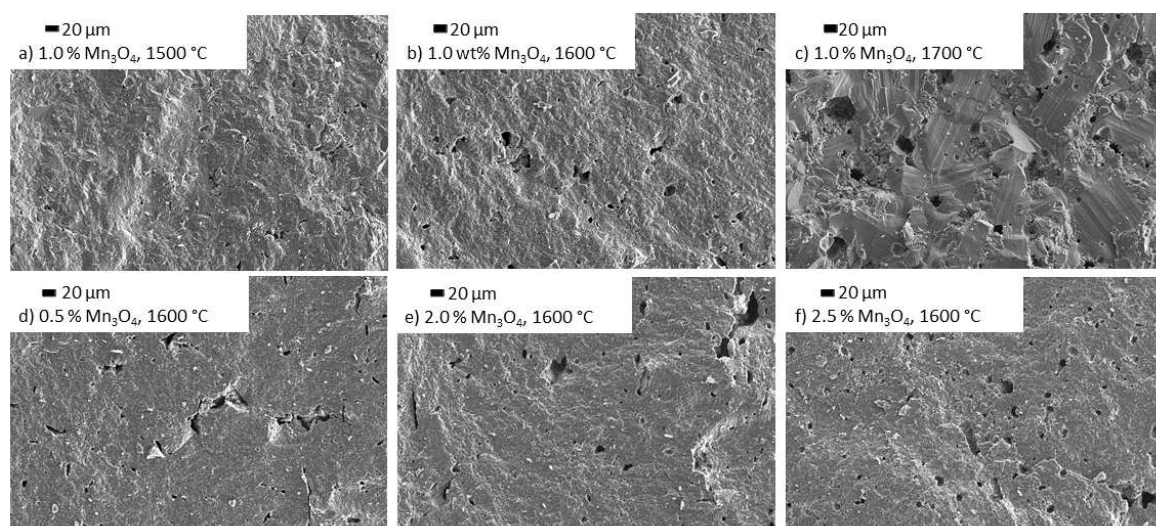
Figure 37. SEM images of Na-β″-alumina samples sintered at 1500 °C, 1600 °C, or 1700 °C, doped with different amounts of Mn_3O_4 (b-f) in comparison to an undoped sample a). Percentages indicate mass fractions. Reprinted with permission from *Dirksen et al.* [86]
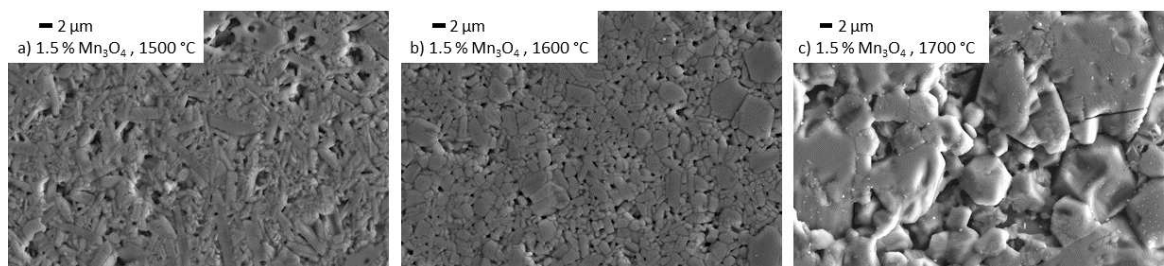
Figure 38. SEM images of Na-β''-alumina samples sintered at 1500 °C a), 1600 °C b), or 1700 °C c) and doped with a mass fraction of 1.5 % Mn_3O_4 after polishing and thermal etching. Other magnifications are displayed in appendix Figure 81.

NiO doping has similar microstructural effects on Na-β''-alumina electrolytes to those of Mn_3O_4 doping. Figure 36 b) shows the relative density of the differently NiO doped and sintered specimens. In a way analogous to Mn_3O_4 doping, NiO doping lead to a lower density with sintering at 1500 °C. For sintering temperatures of 1600 °C or 1700 °C, there was only a negligible diminution of the density with increasing doping level.

SEM images were recorded to evaluate the microstructure presented in Figure 39. Additional SEM images are shown in appendix Figure 85 to Figure 90. The images revealed a remarkable influence of NiO doping on the grain size. While Mn_3O_4 doping suppresses excessive grain growth only at sintering temperatures of 1600 °C, doping with NiO also hinders the formation of a grain structure dominated by large grains with a diameter of more than 100 μm at sintering temperatures as high as 1700 °C. An example of this is shown for a sample doped with a mass fraction of 1.0 % NiO in Figure 39 (c).

Another difference between Mn_3O_4- and NiO doping at sintering temperatures of 1600 °C were some large, directional and anisotropicly grown grains between the areas of fine grains. Especially at the low doping amount of mass fractions of 0.5 % NiO (Figure 39), the number of large grains was notably higher than after doping with a mass fraction of 0.5 % Mn_3O_4. SEM images of thermally etched samples doped with a mass fraction of 1.5 % NiO are shown in Figure 40. A sintering temperature of 1500 °C resulted in flake-like shaped grains (needle-like shaped in the 2D-SEM technique) with a mean diameter of 2.7 μm ± 0.7 μm, which is nearly the same mean diameter as the one of the sample sintering at a temperature of 1600 °C (mean diameter 2.6 μm ± 0.7 μm). As was already observed in samples doped with Mn_3O_4, the grain shape changed from flake-like to more circular-shaped grains with increasing sintering temperature. The prevention/downshift of excessive grain growth by the addition of Mn_3O_4 or NiO is surprising, since the DSC measurements (chapter 4.1.4) show a melting peak for Mn_3O_4 and NiO doped samples at

the same temperature as the undoped sample. Possibly the addition of Mn_3O_4 and NiO hinders the dissolution and precipitation processes that typically occur while liquid assisted sintering takes place. Nevertheless this topic should be further examined in future. A possible research strategy is the quenching of the sintering process at different temperatures and subsequent SEM, EDX and XRD measurements.

Zhu et al. [116] also doped lithium stabilized Na-β″-alumina with NiO and reported different results. They observed increased densification of the ceramic by the addition of NiO. A possible reason for this different finding is the low sintering temperature of 1400 °C / 2 h used by *Zhu et al.* In my work I applied high sintering temperatures for only 0.5 h. The low sintering temperature also resulted in a very low ionic conductivity (0.066 S cm^{-1} at 350 °C) compared to the ionic conductivity of lithium stabilized Na-β″-alumina electrolytes published by other researchers (see Chapter 4.2.4).
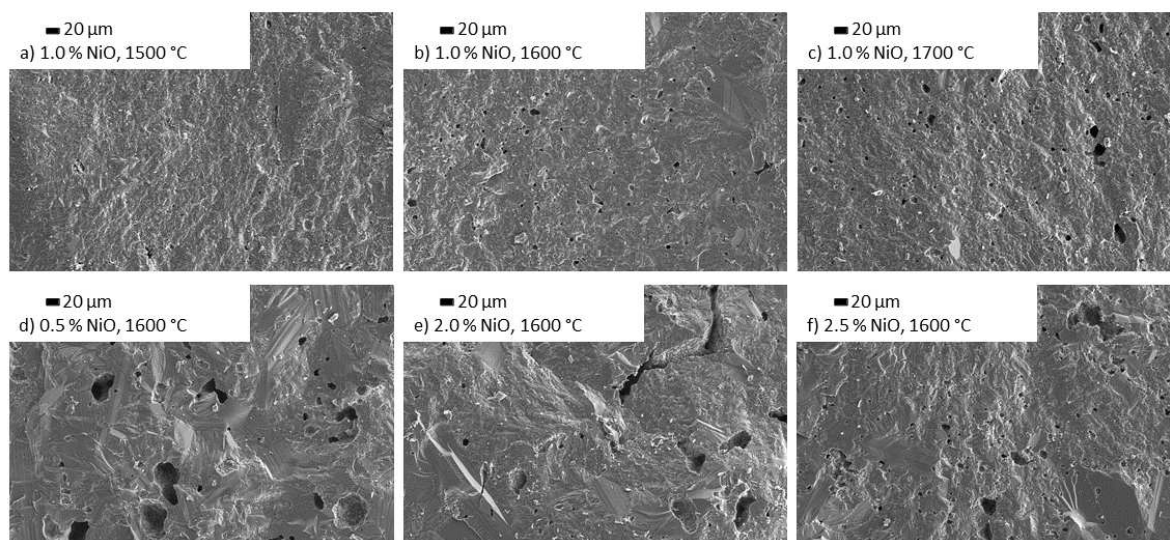
Figure 39. SEM images of Na-β″-alumina samples sintered at 1500 °C, 1600 °C, or 1700 °C, doped with different amounts of NiO (b-f) in comparison to an undoped sample a). Percentages indicate mass fractions. Reprinted with permission from *Dirksen et al.* [86]
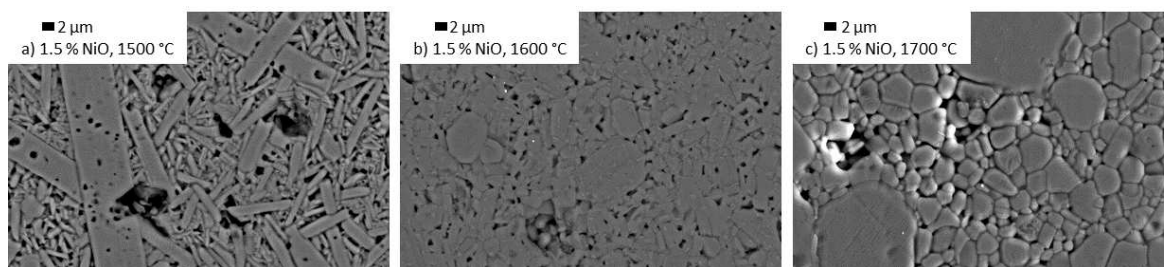
Figure 40. SEM images of Na-β″-alumina samples sintered at 1500 °C a), 1600 °C b), or 1700 °C c) and doped with a mass fraction of 1.5 % NiO after polishing and thermal etching. Other magnifications are displayed in appendix Figure 87.

4.2.2 Interim résumé

The effect of the three dopants tested and sintering regimes on the microstructure of lithium stabilized Na-β″-alumina electrolytes can be summarized as follows:

Higher sintering temperatures result in higher porosity, and thus lower relative density, and excessive grain growth. These features were observed at sintering temperatures of ≥ 1600 °C for undoped samples.

TiO_2 doping increases relative density if low doping amounts are used. The maximum is reached with 1.0 % of TiO_2 at all the sintering temperatures tested. TiO_2 also enables the formation of large grains at a low sintering temperature of 1500 °C.

This is due to low temperature liquid-assisted sintering, the effects of liquid assisted sintering (described in chapter 2.5) are intensified at high mass percentages of TiO_2, since more liquid phase is available for mass transport.

Mn_3O_4 doping has little influence on the relative density at sintering temperatures of 1600 °C and 1700 °C. At 1500 °C, it reduces the density. Mn_3O_4 doping can hinder the formation of large grains and provides a microstructure shaped by homogeneous, small grains

NiO doping has little influence on the relative density at sintering temperatures of 1600 °C and 1700 °C. At 1500 °C, it reduces the density. NiO doping also hinders the formation of large irregular grains up to a sintering temperature of 1700 °C

4.2.3 Effect of doping on the characteristic fracture strength of Na-β″-alumina

Four main material properties influence the characteristic fracture strength of Na-β″-alumina electrolytes.

First, the inherent fracture strength of the crystal phase is essential. Stoichiometry influences it. A second factor is the amount and nature of secondary phases within the electrolyte. These are able to increase the characteristic fracture strength (*e.g.,* ZrO_2) and create a predetermined breaking point. [118,150,151] The third factor is the pores. Pores sharply lower the characteristic fracture strength of ceramics. [69] The fourth material property is the grain size and the grain shape. Large grains tend to lower the characteristic fracture strength of ceramic compounds because there are fewer grain boundaries that prevent crack growth. [69]

The characteristic fracture strength is given by σ_0, representing the tensile stress required to break 63.2 % of the tested samples in a ball-on-three-balls measuring setup (the value of 63.2 % is typically chosen for *Weibull* statistics [152,153]). Figure 41 displays the characteristic fracture strength of the differently doped and sintered Na-β″-alumina electrolytes. The exact values and the non-dimensional distribution parameter "m" (see chapter 3.3) are listed in the appendix Table 8, Table 9, and Table 10.
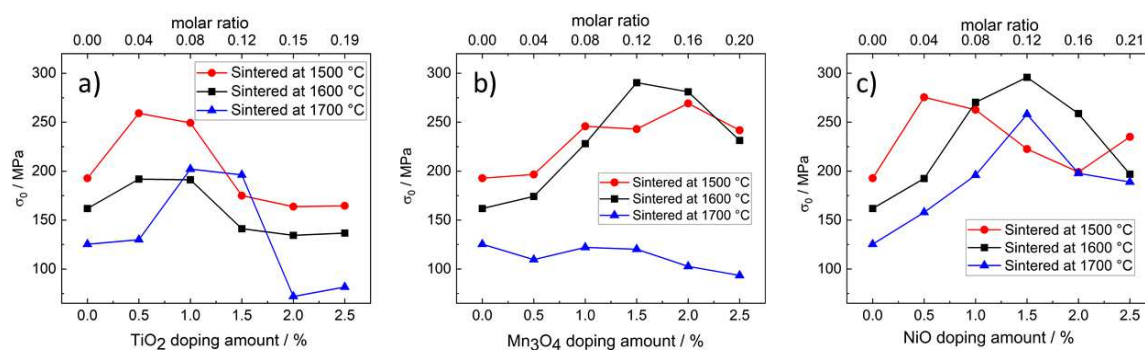
Figure 41. a) Characteristic fracture strength σ_0 of TiO_2 doped Na-β″-alumina. The results of TiO_2 doped samples and sintering temperatures of 1500 °C or 1600 °C are reprinted with permission from *Dirksen et al.* [64]. Those of 1700 °C are reprinted from [86] b) Characteristic fracture strength σ_0 of Mn_3O_4 doped Na-β″-alumina. Percentages indicate mass fractions. The results from the samples sintered at 1600 °C or 1700°C are reprinted from *Dirksen et al.* [86] c) Characteristic fracture strength σ_0 of NiO doped Na-β″-alumina. The results from the samples sintered at 1600 °C or 1700 °C are reprinted from *Dirksen et al.* [86]

Influence of the sintering temperature on the characteristic fracture strength of undoped samples

The undoped samples had a characteristic fracture strength of 193 MPa at a sintering temperature of 1500 °C. Higher sintering temperatures resulted in lower characteristic fracture strengths. At a temperature of 1700 °C, σ_0 dropped to 125 MPa. This reduction is in line with the observations of chapter 4.2, where the increased porosity and immense

grain growth were discussed. Since the phase content stayed constant and no dopants were incorporated, those factors are irrelevant for the undoped samples.

Influence of TiO$_2$ doping on the characteristic fracture strength

The TiO$_2$ doping amount also greatly influenced the characteristic fracture strength (Figure 41 a). Small mass fractions (0.5 % and 1.0 %) of TiO$_2$ promote the characteristic fracture strength regardless of the sintering temperature.

At 1500 °C, the maximum fracture strength of 259 MPa was reached by doping with 0.5 % TiO$_2$. At a doping mass fraction of 1.0 % TiO$_2$, σ_0 decreased slightly to 249 MPa, while doping with a mass fraction of 1.5 % resulted in a sharp drop to a value of 175 MPa. These results are in good agreement with the microstructure reported in chapter 4.2. While samples doped with a mass fraction of 0.5 % TiO$_2$ had fine and homogeneous grains, the first large and irregular grains occurred at a mass fraction of 1.0 % TiO$_2$. A turning point was reached at a mass fraction of 1.5 % where the whole microstructure was dominated by large irregular grown grains.

At higher sintering temperatures, the characteristic fracture strength follows the same trend as the relative density. Hence, the porosity becomes a more dominant factor. Since the characteristic fracture strength only decreased slightly between a mass fraction of 1.5 % and 2.5 % and sintering temperatures of 1500 °C or 1600 °C, it seems likely that the amount of secondary phase from TiO$_2$ doping is too small to exert a distinct influence. Other researchers have confirmed the increase in the characteristic fracture strength. [27] For example, *Chen et al.* [134] found a maximum of 230 MPa at a mass fraction of 0.5 % TiO$_2$ and a sintering temperature of 1550 °C.

Influence of Mn$_3$O$_4$ doping on the characteristic fracture strength

The results obtained from Mn$_3$O$_4$ doping were different from those obtained from samples doped with TiO$_2$. At 1500 °C and 1600 °C Mn$_3$O$_4$ doping improved the characteristic fracture strength for all doping amounts tested. A maximum of 290 MPa was reached at a sintering temperature of 1600 °C and a mass fraction of 1.5 % Mn$_3$O$_4$.

At sintering temperatures of 1700 °C, the dopant slightly reduced the characteristic fracture strength. These results are in good agreement with the SEM observations, where samples sintered at temperatures of 1500 °C had fine-grained flake-shaped microstructure that points to high fracture strength. Samples sintered at 1600 °C had fine and rounded grains.

However, the microstructure of samples sintered at 1700 °C was defined by large grains and a high porosity and this clearly implies weak mechanical strength.

Furthermore, I observed that, independently of doping level, the relative density and porosity of the samples sintered at 1700 °C stayed constant while the characteristic fracture strength decreased. It seems possible that incorporating Mn-ions reduces the intrinsic fracture strength of the Na-β''-alumina crystal lattice by expanding the crystal parameters (see chapter 4.1.2) and introducing residual stresses. However, further experiments are necessary to distinguish between the influence of the microstructure and the possible influence of residual stresses introduced by doping.

Influence of NiO doping on the characteristic fracture strength

The effects of NiO doping are generally similar to those of Mn_3O_4 doping. In a way that deviates from what was seen with Mn_3O_4 doping, NiO doping also increases the characteristic fracture strength of samples sintered at 1700 °C. This is likely to be because of the influence of NiO doping on the microstructure (Chapter 4.2.).

The maximum characteristic fracture strength of 296 MPa was reached at a sintering temperature of 1600 °C and a mass fraction of 1.5 %. At 1700 °C, the greatest characteristic fracture strength of reached was 258 MPa, even though the relative density of the samples sintered at 1700 °C was relatively low. It is therefore possible to conclude that the grain size and, possibly, the grain shape, is the predominant factor affecting the fracture strength. The change of the relative density from around 97 % (samples sintered at 1600 °C) to 92 % (samples sintered at 1700 °C) seems less influential.

The influence of incorporating Ni^{2+} into the crystal lattice on the mechanical strength is not yet apparent. High mass fractions of 2.0 % or 2.5 % NiO potentially weaken the lattice because they led to a lower characteristic fracture strength at all sintering temperatures tested, even though the density and the grain size change only marginally.

The fracture strength of NiO doped Na-β''-alumina electrolytes was, unlike Mn doped Na-β''-alumina, also evaluated by another researcher. *Zhu et al.* [116] measured the fracture strength by three-point bending and found a maximum of 296 MPa at a doping mass fraction of 0.25 %. Higher doping amounts sharply reduced the fracture strength to 177 MPa at the highest mass fraction tested of 1.5 % NiO. One possible explanation for the different findings is the different sintering regimes and different starting materials. *Zyl et al.* [90] showed that, in particular, a change of the Al-source influences the resulting

electrolyte properties. This might apply here because my work and that of *Zhu et al.* [123] do use different Al-sources. *Zhu et al.* used α-Al$_2$O$_3$ and sodium oxalate as a reactant but I used AlO(OH) and Na$_2$CO$_3$.

4.2.4 Effect of doping on the ionic conductivity of Na-β″-alumina

The ionic conductivity of a Na-β″-alumina electrolyte depends on several factors. The microstructure of the electrolyte plays the most important role and depends on several factors. [65,149]

First, the **grain size** must be taken into account. Smaller grains result in high resistant grain boundaries [154] that have to be crossed by a Na-ion. This resistance to ion movement reduces the ionic conductivity of the electrolyte. Next, the **porosity** of the electrolyte influences the ionic conductivity. The more pores there are, and the larger they are, the greater the distances that ions must traverse. In consequence, conductivity is reduced. As the final microstructure parameter, the **grain shape** must be considered. Needle or flake-like Na-β″-alumina grains extend the tortuosity of the ion pathway. This factor is even more important because of the 2D-conductive nature of Na-β″-alumina compared to 3D-conductive materials. [155,156]

It is not only the microstructure that has an influence but also the crystallographic composition of the electrolyte. The Na-β″-alumina phase content, as the conductive crystal phase, is important and should be as high as possible. Nonconductive **secondary phases** extend the paths of ions in the same way as pores do. In addition, features of the Na-β″-alumina crystal phase itself can alter ionic conductivities. Such features include dopant-introduced **point defects** and different Na$^+$-occupation ratios of the conducting layer. [33,157]

The ionic conductivity of the doped Na-β″-alumina electrolytes was measured by impedance spectroscopy as described in section 3.3. The data obtained were expressed in a *Nyquist* plot, and a regression analysis was performed. Therefore, a *Randles* circuit (see Figure 19) was chosen to analyze the bulk resistance R$_b$ and the grain boundary resistance R$_{gb}$. Some sample plots are displayed in Figure 42, while appendix Table 11, Table 12 and Table 13 show additional data. The ionic conductivities calculated from the fitted curves are shown for TiO$_2$ doping in Figure 43 a), for Mn$_3$O$_4$ doping in Figure 44 a), and for NiO doping in Figure 45 a). The specific grain boundary resistances for TiO$_2$ doping are shown in Figure 43 b), for Mn$_3$O$_4$ doping in Figure 44 b), and for NiO doping in Figure 45 b).
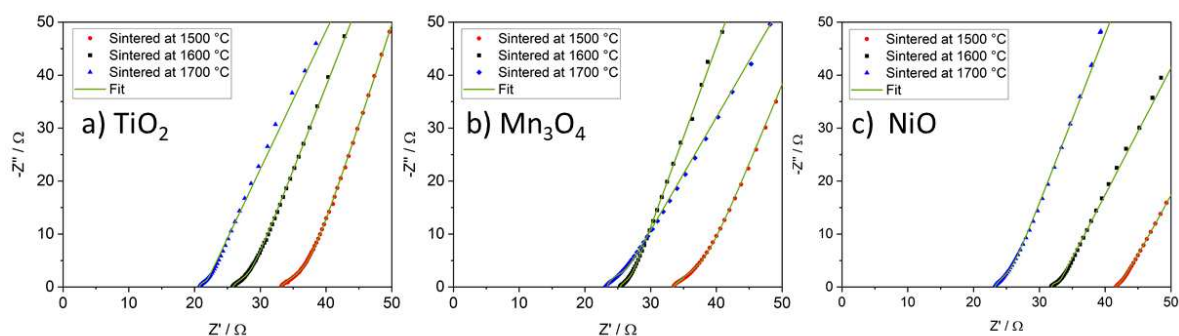
Figure 42. Nyquist plots of differently doped Na-β″-alumina samples recorded at 300 °C. a) doped with a mass fraction of 1.0 % TiO_2 b) doped with a mass fraction of 1.0 % Mn_3O_4 c) doped with a mass fraction of 1.0 % NiO. Reprinted with permission from *Dirksen et al.* [86]

Influence of the sintering temperature on the ionic conductivity of undoped samples

The ionic conductivity at 300 °C of undoped samples increased from 0.15 S cm^{-1} when the sintering temperature was 1500 °C. Raising the sintering temperature to 1600 °C raised the conductivity to 0.21 S cm^{-1}. A further rise of sintering temperature to 1700 °C further raised the conductivity to 0.25 S cm^{-1}. As shown in chapter 4.1, the phase content is not significantly changed by altering the sintering temperatures. Therefore, the influence on the ionic conductivity is presumably low. No significant change was found in Na-content after the different sintering regimes by the rather imprecise EDX method. Nevertheless, higher sintering temperatures led to excessive grain growth. Such growth shortens the percolation path [64,154] and lowers the grain boundary resistance (see Figure 43 b)). The specific grain boundary resistance of an undoped sample sintered at 1700 °C was only 0.16 Ω cm. This was much less than the 0.38 Ω cm for a similar sample sintered at the lower temperature of 1500 °C. Samples sintered at higher temperatures tend to have a higher porosity and that increases the path length. However, the factors that reduce conductivity are more than offset by those that increase it. In consequence, ionic conductivity rises with increasing sintering temperature. The coherence between grain size and conductivity illustrates a general trade-off in the production of Na-β″-alumina electrolytes. Larger grains reduce the characteristic fracture strength but increase the ionic conductivity.

Influence of TiO_2 doping on the ionic conductivity

The amount of TiO_2 dopant, as well as the sintering temperature, also influences the ionic conductivity of Na-β″-alumina (Figure 43 a)). For 1500 °C, the lowest sintering temperature tested, adding a mass fraction of 1.5 % TiO_2 raised the ionic conductivity from 0.15 S cm^{-1} to a maximum of 0.30 S cm^{-1}.

In Chapter 4.2., I showed that a mass fraction of 1.5 % TiO_2 changes the microstructure from fine-grained to one dominated by large grains. In consequence, the ionic conductivity increases, and the characteristic fracture strength decreases at this point. Higher amounts of dopant than this did not further increase conductivity. This is because higher dopant amounts increase porosity. Thus, the ionic conductivity remains more or less constant. These results show that the microstructural changes induced by TiO_2 doping correlate with the ionic conductivities measured.

The specific grain boundary resistance (Figure 43 b)) of the TiO_2 doped samples was in good agreement with the microstructure observed at a sintering temperature of 1500 °C. The specific grain boundary resistance was maximal for the undoped sample, followed by the sample doped with a mass fraction of 0.5 % TiO_2 and a sintering temperature of 1500 °C. Higher doping amounts and higher sintering temperatures reduce the specific grain boundary resistance due to the increasing grain size.

It is also possible that increasing phase contents of the nonconductive Ti-containing species ($NaLiTi_3O_7$ or $Na_{1.97}Al_{1.82}Ti_{6.15}O_{16}$) lower the ionic conductivity. However, since their concentration was low and the Na-β''-alumina phase content stayed nearly constant, it is inevitable that the microstructural changes are more influential.

Independent of the doping level, samples sintered at 1600 °C or 1700 °C exhibited a microstructure dominated by large grains and, therefore, high ionic conductivity. Also, the grain boundary resistance was constantly at values of about 0.2 Ω cm, independently of the TiO_2 amount. The maximum ionic conductivity was reached in both cases at a mass fraction of 1.0 % TiO_2. This corresponds to the highest relative density for both sintering temperatures. It is possible that the reduced density at higher doping amounts also reduces the ionic conductivity. The role of the Na-β''-alumina phase content is minor since the phase content changed only marginally at different doping amounts. A significant depletion of sodium within the Na-β''-alumina crystal phase, caused by the formation of sodium-containing Ti-species and influencing the ionic conductivity, was not observed by EDX measurements (Chapter 4.1). This was expected because sodium-rich $NaAlO_2$ was detected in all samples. Furthermore, *Bay et al.* [33,154] also confirm that microstructure is the dominant factor for differently sintered but undoped Na-β''-alumina electrolytes.
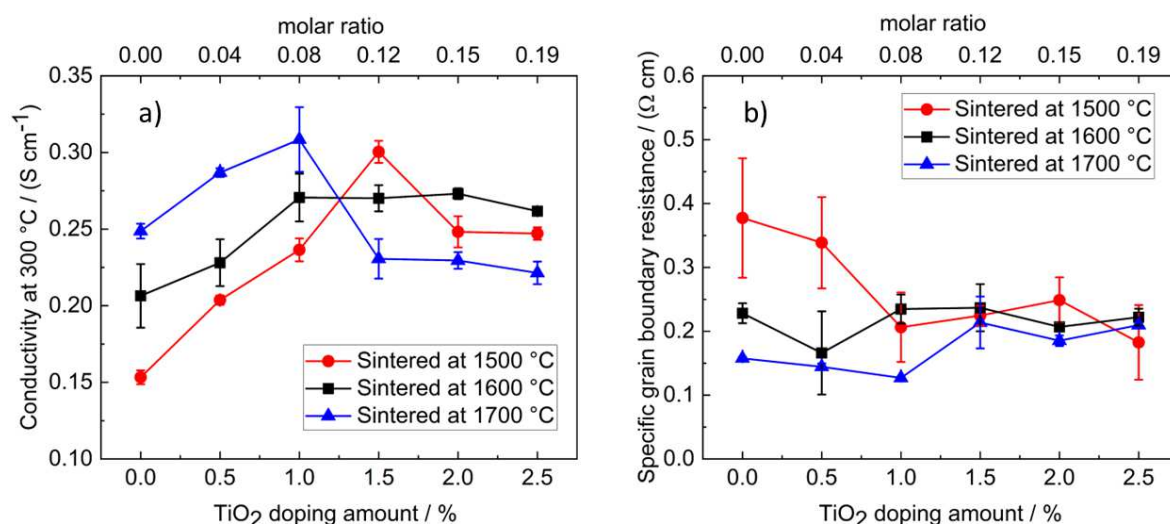
Figure 43. Ionic conductivity (a) and specific grain boundary resistance (b) at a temperature of 300 °C of TiO$_2$ doped Na-β″-alumina samples sintered at 1500 °C, 1600 °C, or 1700 °C. Percentages indicate mass fractions. Reprinted with permission from *Dirksen et al.* [86]

Influence of Mn$_3$O$_4$ doping on the ionic conductivity

The influence of Mn$_3$O$_4$ doping on the ionic conductivity of Na-β″-alumina electrolytes is displayed in Figure 44 a), while the grain boundary resistance can be seen in Figure 44 b). The ionic conductivity is more dependent on the sintering temperature than on the doping amount. This finding is unexpected since the inhibition of excessive grain growth at sintering temperatures of 1600 °C should lower the ionic conductivity at higher doping amounts. Instead, conductivity rises slightly from 0.21 S cm^{-1} to 0.23 S cm^{-1} at 300 °C. It seems likely that this finding is once more explained by the microstructure changes described in chapter 4.2.

Mn$_3$O$_4$ doped samples have small grains at sintering temperatures of both 1500 °C and 1600 °C. However, grain shapes are notably different at the two temperatures. The flake-shaped grains occurring at sintering temperatures of 1500 °C seem to produce conduction paths longer than those produced by the more circular grains occurring at sintering temperatures of 1600 °C. The flake-shaped grains also produce higher specific grain boundary resistances (Figure 44 b)). These effects might be linked to the 2D-conductive nature of Na-β″-alumina. At temperatures of 1700 °C, the microstructure was dominated by very large grains that produced high ionic conductivity but low fracture strength. Therefore, the findings from measuring the characteristic fracture strength, the ionic conductivity, and the shape of the microstructure are in good agreement.

Future EBSD (Electron backscatter diffraction) scans could possibly further clarify this relationship between microstructure and ionic conductivity. The influence of Mn^{2+}/Mn^{3+}-ions occupying Al^{3+}-positions is hard to separate from microstructural effects and the alteration of Na-ions in the conduction slab. However, because there is little influence of Mn_3O_4 doping at sintering temperatures of 1700 °C, where the dopant does not prevent excessive grain growth, the influence of the microstructure is greater than that of the doping. In future research, measurements on a single crystal might be able to avoid these difficulties.
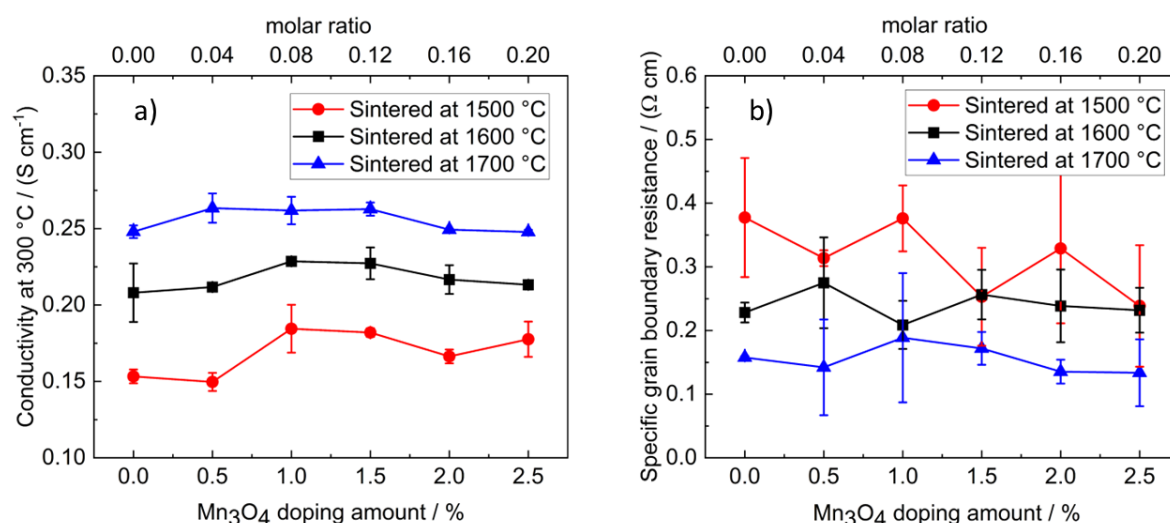
Figure 44. Ionic conductivity (a) and specific grain boundary resistance (b) at a temperature of 300 °C of Mn_3O_4 doped Na-β″-alumina samples sintered at 1500 °C, 1600 °C, or 1700 °C. Percentages indicate mass fractions. Reprinted with permission from *Dirksen et al.* [86]

Influence of NiO doping on the ionic conductivity

The influence of NiO doping is similar to that of Mn_3O_4 doping. Even though NiO doping suppresses excessive grain growth even more effectively than Mn_3O_4 doping, it does not greatly influence ionic conductivity (Figure 45 a)) or specific grain boundary resistance (Figure 45 b)). The explanation for this observation is identical to the findings on Mn_3O_4 doped samples, namely the change of flake-shaped grains to more rounded grains. The influence of the doping amount is again low even though Ni^{2+} doping led to a larger increase of Na-ions in the conduction slab than Mn_3O_4 doping. This is another hint of the low influence on the ionic conductivity of Na-β″-alumina electrolytes of slight changes in the Na^+-occupation ratio or of foreign ions in the crystal lattice.
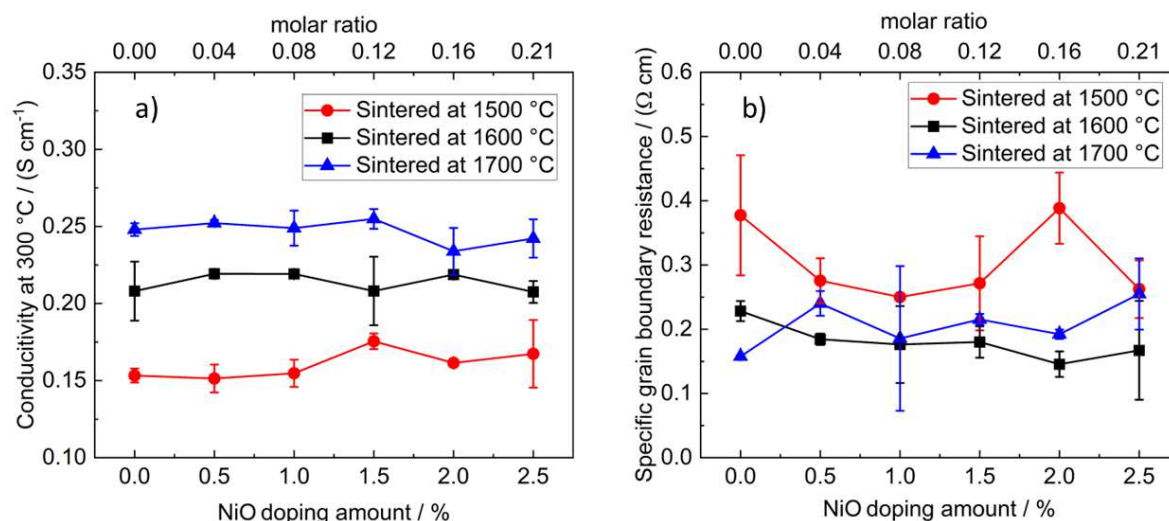
Figure 45. Ionic conductivity (a) and specific grain boundary resistance (b) at a temperature of 300 °C of NiO doped Na-β″-alumina samples sintered at 1500 °C, 1600 °C, or 1700 °C. Percentages indicate mass fractions. Reprinted with permission from *Dirksen et al.* [86]

Next to the ionic conductivity at 300 °C, the activation energy for several samples were calculated (appendix Figure 91). The resulting energies amounted between 0.17 eV and 0.22 eV. Samples with higher ionic conductivities at 300 °C tent to show lower activation energies. This observation is in line with other researchers [116,122] and can be explained by similar phenomena that influences the ionic conductivity (larger grains, short ion pathway, *etc*.). The activation energies are in line with the ones measured by other researchers. [121][116,121,122]

4.2.5 Interim résumé

The ionic conductivity measurements and the characteristic fracture strength of transition metal doped Na-β″-alumina electrolytes reveal that TiO_2 doping is a promising candidate for research towards future industrial production. Adding small amounts of TiO_2 leads to higher ionic conductivity and characteristic fracture strength. Those improvements are possible at low sintering temperatures, so reducing production and energy costs. The favorable conditions are a doping amount of 1.0 % TiO_2 and a sintering temperature of 1500 °C. These samples had a characteristic fracture strength of 249 MPa, 56 MPa more than the best undoped sample. They also had an ionic conductivity of 0.22 S cm⁻¹, the highest value achieved without using very high sintering temperatures and without producing excessive grain growth.

Mn_3O_4 and NiO doping also showed the potential to maximize the characteristic fracture strength of Na-β″-alumina electrolytes. Adding a mass fraction of 1.5 % of NiO and a

sintering temperature of 1600 °C resulted in the highest measured characteristic fracture strength of 296 MPa. The reduction of sintering temperatures or the increase of ionic conductivity is impossible with the addition of Mn_3O_4 or NiO.

For this reason, only TiO_2 doped electrolytes were put into operation in two demonstration cases in order to verify the chemical and electrochemical stability.

4.3 Demonstration case 1: TiO₂ doped Na-β″-alumina as electrolyte in cells

The formation of secondary phases resulting from TiO_2 doping necessitates the verification of the chemical and electrochemical stability of the electrolyte in operation. It must be ruled out that the secondary phases destabilize the electrolyte towards the chemicals or voltages occurring in electrochemical cells. To clarify this, electrochemical cell tests were conducted.

First, different current densities were tested in a Na/Na-symmetrical cell setup. Second, a Na/NiCl₂ full cell was used to test an electrolyte doped with a mass fraction of 1.0 % TiO_2 and sintered at 1500 °C.

As outlined in chapter 2.6, Na/NiCl₂-cells use liquid sodium as negative electrode and a Ni-based positive electrode material infiltrated with the liquid electrolyte NaAlCl₄. The cell design used for the experiment is shown in chapter 3.4, *i.e.*, in Figure 21. Compression seals were used instead of welded ones. Hence, the test did not represent stability tests lasting several months but gives a first impression about the suitability of TiO_2 doped Na-β″-alumina. The measuring regime applied to the cell was that used for Na/NiCl2 cell assembly and test procedures (Chapter 3.4.). It comprises mainly the discharge of the cell with different currents from 100 % SoC.

4.3.1 Symmetric Na|TiO₂ doped Na-β″-alumina|Na cell test

Figure 46 displays the voltage profiles of the Na|TiO₂ doped Na-β″-alumina|Na cell at different currents. Low currents were first applied to the cell for five minutes in each direction. This procedure ensured that the electrolyte surface was evenly covered with sodium. Thereafter, a current of 500 mA (283 mA cm^{-2}) was applied to the electrolyte. This was a much greater current than the 130 mA cm^{-2} typically applied to commercial Na/NiCl₂-cells. [158,159]
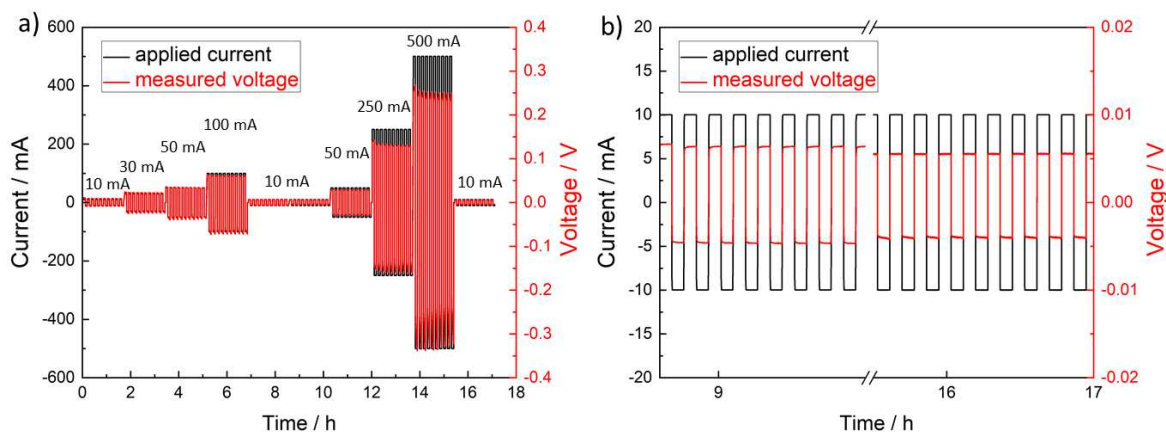
Figure 46. Voltage profile of a Na|TiO₂ doped Na-β″-alumina|Na symmetrical cell at different currents for 5 min in each direction at 300 °C. (10 mA corresponds to a current density of 5.66 mA cm^{-2} and 500 mA to 283 mA cm^{-2}) a) overview of all measurements b) middle and end area of a) in detail.

An anomaly of the measurement in Figure 46 is the slightly different voltage dependence of the current sign. In a symmetrical cell, it would be expected that the same voltage is measured no matter in what direction the current flows. The minor differences are caused by the experiments being carried out on a heating plate and not in an oven. One side of the flat cell was thus hotter than the other and a temperature-dependent potential affected the voltage measured. To calculate the ohmic resistance, *Ohm*'s law was applied. The calculation used the mean voltage of the two current directions. After the first couple of cycles, the resulting conductivity was stable at 0.21 S cm^{-1} (independent of the current applied). Resistance only increased after applying 500 mA. As a result, the ionic conductivity rose irreversibly to 0.24 S cm^{-1}. It is certain that the exceptionally high current density (283 mA cm^{-2}) leads to some form of micro cracks and this have caused the slight increase in ionic conductivity. Analytical verification of the micro crack formation postulated failed so far because the carbon coating, and Na-remained on the electrolyte surface, hindered microscopic methods. Cleaning the electrolyte with ethanol did not help as the cleaning probably removed any existing Na remains in the cracks therefore it was not possible to find any Na-filled cracks. This is not surprising because the sodium was washed out, and the remaining micro crack canals were too small to be detected easily by standard analytical methods.

The ionic conductivity of the electrolyte initially measured in the test cell (0.21 S cm^{-1}; measured by applying *Ohm's* law) was slightly lower than the ionic conductivity measured by applying impedance spectroscopy on the test cell (0.236 S cm^{-1}). This difference is expected since liquid sodium has a lower wettability than liquid salt. Furthermore,

83

overpotentials occur, caused by the mass transport and the redox reactions in a $Na|TiO_2$ doped Na-β''-alumina$|Na$ cell.

The impact of TiO_2 doping on the largest current density that it is possible to apply to a Na-β''-alumina electrolyte and how the secondary phases influence dendrite formation should be evaluated in future research. The experiments I report here only lasted a short time, several days. They indicate, however, that over this short time at least, the current densities occurring in $Na/NiCl_2$-cells do not affect the Na-β''-alumina electrolyte. A longer-term measurement with 2000 cycles of 6 min with a current of 100 mA (56.6 mA cm^{-2}) in a $Na|TiO_2$ doped Na-β''-alumina$|Na$ cell is displayed in appendix Figure 92 and shows no salience. No long term measurements, over several months or years, have yet been made.

4.3.2 Na/NiCl$_2$-cell test

Next to the symmetrical-cell setup, the TiO_2 doped electrolytes were tested in a $Na/NiCl_2$-full cell. The capacities that were measured by applying different cycling rates are shown in Figure 47. As expected, high cycling rates lead to low capacities. The maximum capacity of 71 mAh was reached at the lowest current of 5 mA (discharge rate of 0.0526 h^{-1} corresponds to 1/16 C). The lowest capacity of 60 mAh was measured using the highest tested current of 30 mA (discharge rate of 0.375 h^{-1} corresponds to 3/8 C). This resulted in a *Peukert exponent* of 1.094. This is a value similar to that of NiMH (Nickel-metal hydride battery) cells but lower than commercial LIBs. [160] Furthermore, it should be noted that the $Na/NiCl_2$-cells that I used were not tested at the high cycling rates used to test commercial NiMH or LIBs.

After testing different discharge currents, the stability of the cell system was tested by performing 90 charge-discharge cycles at a constant cycling rate of 0.125 h^{-1} (discharge at 10 mA). The resulting capacity was relatively stable at 68 mAh. A slight drop in capacity was registered between the cycles 40 and 50. It seems possible that this occurred because a sodium drop was distributed unevenly at the anode-side of the electrolyte and so caused the temporary capacity change.
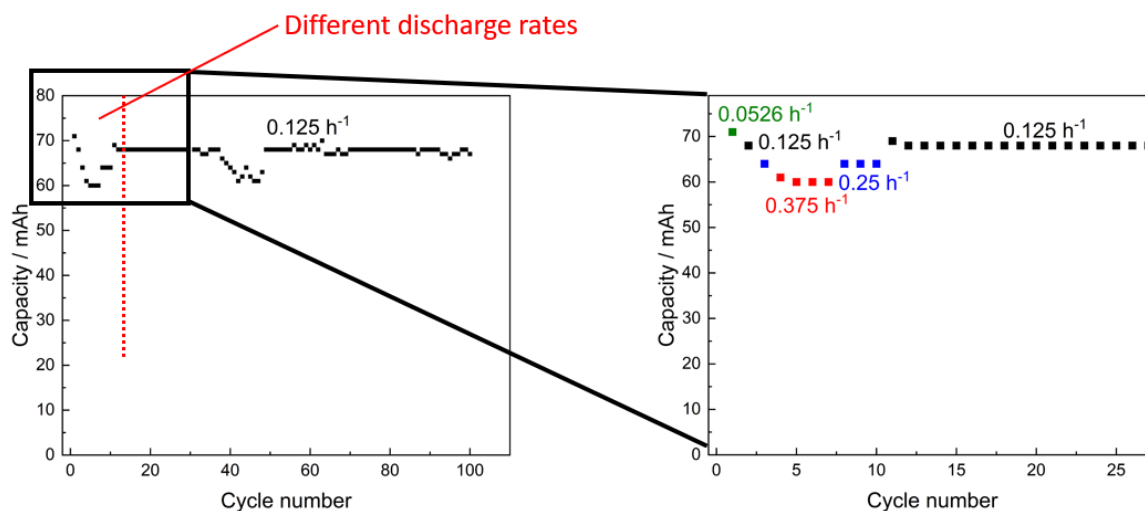
Figure 47. Cycling performance of a Na/NiCl$_2$-cell with a TiO$_2$ doped Na-β″-alumina electrolyte at different discharge cycling rates (A discharge rate of 1 h^{-1} (1 C) corresponds to 80 mA).

To ensure that the Na-β″-alumina electrolyte does not cause cell aging, it was submitted to post-mortem analysis. First, the He-tightness was checked and remained unchanged at $1 \cdot 10^{-9}$ mbar l^{-1} s^{-1}. Next, an XRD analysis (appendix Figure 93) was performed that did not reveal any changes. Also, an analysis of the microstructure by SEM did not reveal any anomalies (Figure 48).
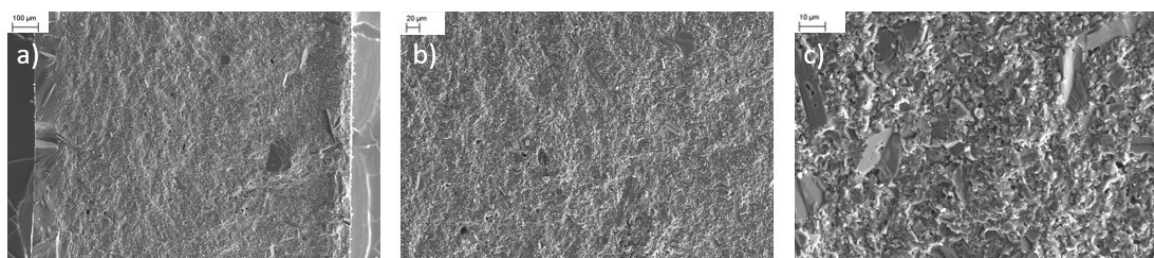
Figure 48. a)-c) SEM images (different magnifications) of a Na-β″-alumina electrolyte (doped with a mass fraction of 1.0 % of TiO$_2$) after using it in a Na/NiCl$_2$-cell. The left edge of a) shows a thin layer (about 100 μm) of glass seal.

Chapter 4.3 gives a first impression of the possibility of using TiO$_2$ doped Na-β″-alumina electrolyte in Na/NiCl$_2$-cells. So far, there was no indication that secondary phases found by XRD and EDX cause any degradation. Nevertheless, further experiments on a large scale and with properly sealed cells are necessary to provide proof of their long-term stability. A more detailed analysis of the maximal current density is also pending.

85

4.4 Demonstration case 2: TiO$_2$ doped Na-β''-alumina as layer in bilayer-electrolytes

In addition to using a conventional Na/NiCl$_2$-cell, TiO$_2$ doped Na-β''-alumina enabled the preparation of disk-shaped bilayer electrolytes by reducing the necessary sintering temperature. Why the temperature reduction is necessary and how a bilayer electrolyte is working, is elaborated in the following chapter:

The layout of the bilayer electrolyte is schematically shown in Figure 49 and Figure 50 shows a photograph. One layer of the flat bilayer electrolyte is thin and consists of densely sintered Na-β''-alumina. The other layer consists of a thick bulk to ensure sufficient fracture strength. However, this bulk is also highly porous. These pores are filled with the liquid and highly conductive secondary electrolyte NaAlCl$_4$. The path of the Na-ions in the electrolyte runs partly through the liquid NaAlCl$_4$ and partly through the dense Na-β''-alumina. Because NaAlCl$_4$ has more than twice the ionic conductivity of Na-β''-alumina [127], it seems possible to reduce the overall resistance of the electrolyte. The operation of the electrolyte was also tested with the porous layer at the anode side and with the pores infiltrated with liquid Na. However, infiltration with liquid Na failed due to its high surface tension.
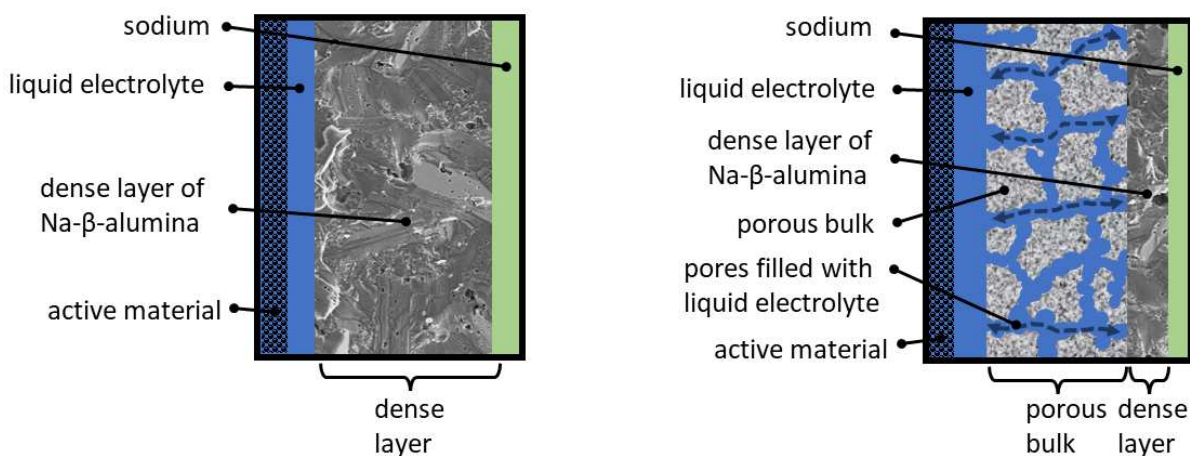
Figure 49. Left: Sketch of the operating principle of a state-of-the-art Na/NiCl$_2$-cell. Right: Sketch of the operating principle of a partially porous solid-state bilayer electrolyte. Reprinted with permission from *Hoppe, Dirksen, et al.* [143]
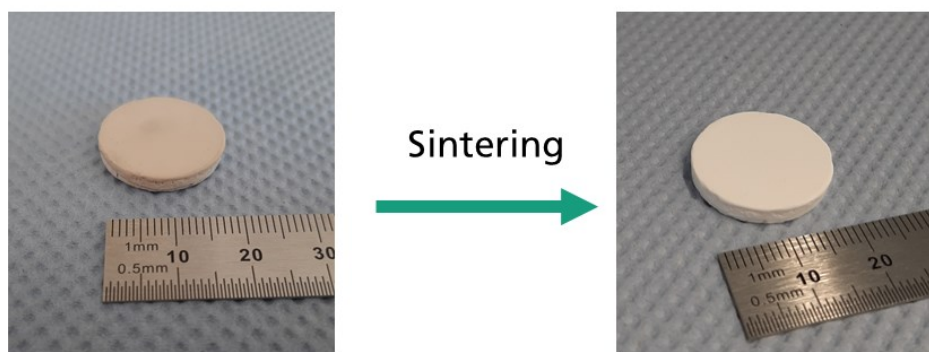
Figure 50. Picture of an unsintered (left) and a sintered (right) bilayer electrolyte.

The porous bulk material was synthesized via a sol-gel route by the University of Leipzig, as described in Chapter 3.5. The crystalline fraction of the bulk material consists, according to XRD analysis (see appendix Figure 94), of > 90% Al_2O_3 and about 5 % of Na-β/β″-alumina. [143]

The dense Na-β″-alumina layer was applied via spin coating of an aqueous Na-β″-alumina slurry (see chapter 3.5). After deposition, the electrolyte must be sintered to join the two layers properly. It turned out that the porosity of the bulk material is highly dependent on the sintering temperature applied. Figure 51 displays the pore distribution of the bulk material heated to 1400 °C for 2 h (Figure 51 a) and 1700°C for 2 h (Figure 51 b).

Due to the higher temperature, the pore volume shrank from 0.34 cm³ g⁻¹ to 0.11 cm³ g⁻¹.
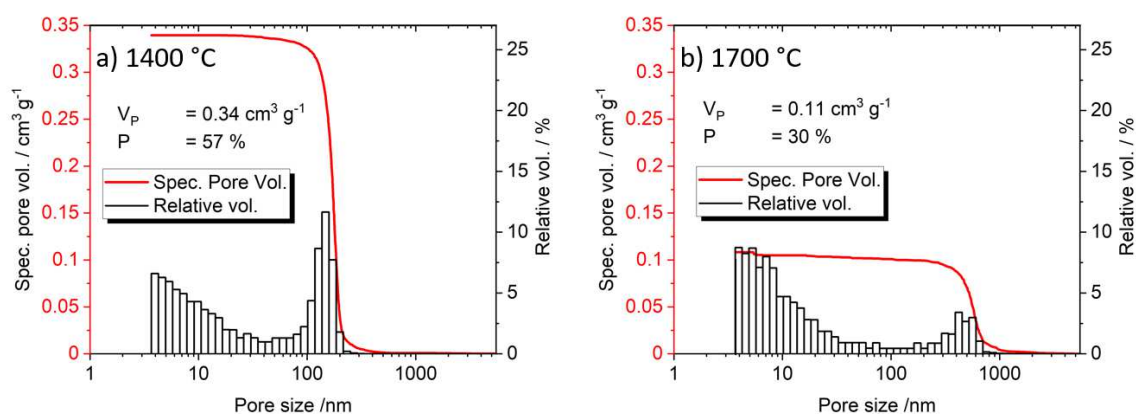
Figure 51. Pore size distribution of the bulk material used to prepare bilayer electrolytes. a) sintered at 1400 °C b) sintered at 1700 °C.

Since a low pore volume minimizes the amount of liquid $NaAlCl_4$ and tiny pores are difficult to infiltrate, many large pores are favorable for the support material. Hence, the sintering temperatures to join the bulk with the dense layer should be as low as possible.

TiO$_2$ doped Na-β″-alumina shows an increased densification process at lower temperatures and is therefore favorable. By using TiO$_2$ doped Na-β″-alumina, it was possible to sinter the bilayer electrolytes at temperatures of only 1400 °C to obtain a sufficiently dense and gas-tight Na-β″-alumina layer. Without the addition of the sintering aid, it was not possible to synthesize TiO$_2$ bilayer-electrolytes with high open porosity.

SEM images of the resulting bilayer electrolytes are presented in Figure 52. Figure 52 (a) shows the cross-section of the electrolyte with the dense layer (thickness of about 50 to 100 µm) on the left and the porous bulk on the right. A surprising feature was the intermediate layer between the dense layer and the bulk. This layer appears brighter than the rest and is about 0.3 mm thick. Figure 52 d) and e) show the crack-free surface of the thin layer. The flake-shaped structure visible under greater magnification (Figure 52 d) is typical for Na-β″-alumina. [116,119,149] The dense layer displayed in detail in Figure 52 c) shows some unwanted porosity, yet it showed a sufficient low leakage rate of $< 1 \cdot 10^{-7}$ mbar·L·s^{-1}. It therefore seems likely that most pores are closed.

It was unfortunately impossible to measure the leakage rate of the porous bulk material. This was because the detector was too sensitive to detect such high leakage.

It is not known whether the unwanted pores of the dense layer (Figure 52) might limit the long-term stability of the electrolyte. How far this might be the case must be tested in future cell tests.
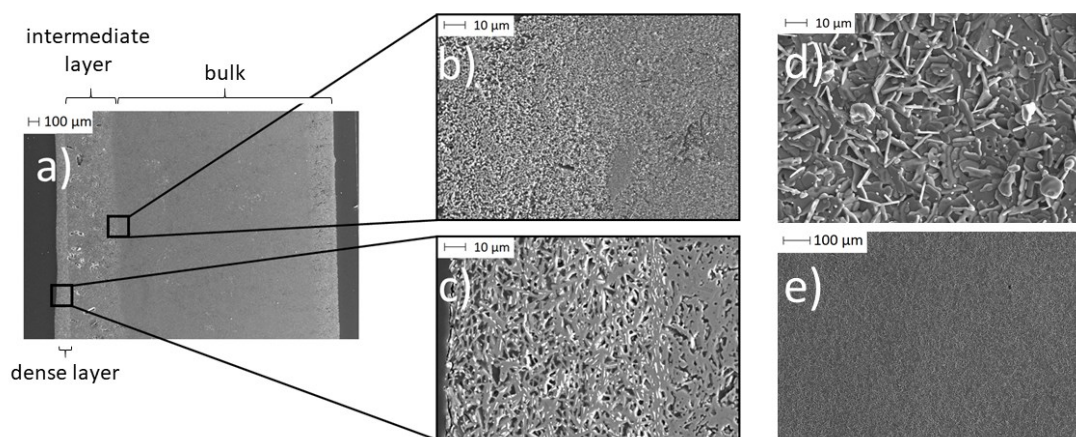
Figure 52. SEM images of a bilayer electrolyte. a) cross-section of the partially porous solid-state bilayer electrolyte; b) cross-section of the transition area from the Na-enriched bulk to undoped bulk material; c) cross-section of the dense thin layer; d) and e) surface of the thin layer. Reprinted with permission from *Hoppe, Dirksen, et al.* [143]

88

To further investigate the bright intermediate layer, I EDX mapped the electrolyte cross-sections (Figure 53). The Na-mapping clearly showed the diffusion of Na from the dense layer that was applied by Na-rich Na-β''-alumina slurry, into the porous bulk, with a low Na concentration. The inhomogeneous diffusion front within the porous bulk can be explained by the faster diffusion of the Na-ions in Na-β''-alumina/Na-β-alumina than in Al_2O_3. [81]

In contrast to the sodium enrichment in the bulk material, Na-depletion of the dense layer was evident. Accordingly, it can be assumed that the Na-β''-alumina phase content and thereby the ionic conductivity of the dense layer was reduced. An attempt to increase the Na-content within the sol-gel synthesis failed because of the crystallization of Na-salts within the gel and, consequently, an uneven distribution of Na. [143]

Future experiments will focus on VPC to increase the Na-β''-alumina phase content of the porous bulk. The general procedure of VPC is described in chapter 2.2.

In contrast to Na, Ti did not show any diffusion from the dense layer into the bulk layer.
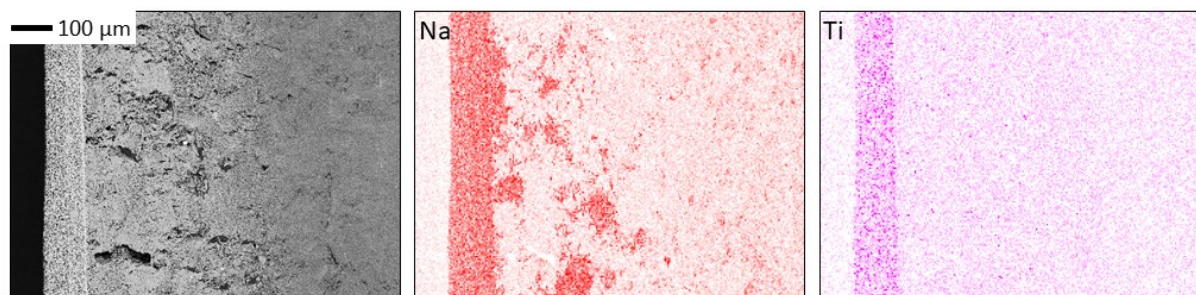
Figure 53. Cross-section SEM images (grey) and EDX mappings of Na (red) and Ti (purple) of a bilayer electrolyte. Reprinted with permission from *Hoppe, Dirksen, et al.* [143]

Figure 54 shows the ionic conductivity of a bilayer electrolyte at different temperatures. The higher the temperature the greater was the ionic conductivity. This behavior was expected because the ionic conductivity of Na-β''-alumina/Na-β-alumina, and that of NaAlCl$_4$, increases with higher temperatures. Ionic conductivity reached a value of 0.1 S cm^{-1} at 300 °C, which is only about half the ionic conductivity of a typical dense Na-β''-alumina electrolyte. The reason for the nonlinear increase of the ionic conductivity at temperatures near 300 °C (the behavior was reproducible for all three tested samples) is not entire clear, since the conductivities of Na-β''-alumina and NaAlCl$_4$ are showing a linear increase in this temperature range. [127] Possibly the low Na-β''-alumina crystal phase

content or the complex behavior of small pores filled with a liquid electrolyte [161,162] are responsible for this anomaly.

Nevertheless, these results provide proof of concept for the bilayer-electrolyte.
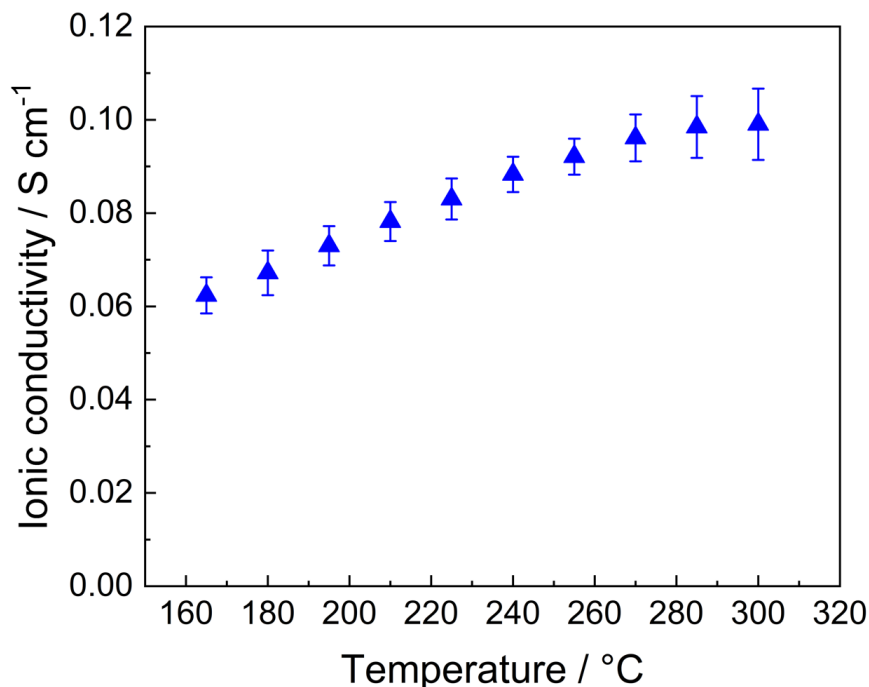
Figure 54. Temperature-dependent ionic conductivity of a bilayer electrolyte. The values are reprinted with permission from *Hoppe, Dirksen, et al.* [143]

Future research regarding the bilayer electrolyte will focus on increasing the Na-β″-alumina phase content within the porous bulk to reach a competitive ionic conductivity. Experiments involving bilayer-electrolytes with even lower Na-β″-alumina phase content showed that Na-β″-alumina phase content is an essential parameter for increased ionic conductivity. [143] It would be fruitless to increase porosity further because to do so would harm structural integrity.

In summary, it was possible to synthesize and test a novel type of bilayer electrolyte – with a porous bulk and a dense, thin layer. The dense layer was correctly bonded to the porous bulk without cracks in the porous bulk. Reducing the sintering temperature by TiO_2 doping enabled the synthesis of bilayer electrolytes at low sintering temperatures, thereby maintaining high porosity in the bulk layer. Due to the large open porosity, the infiltration of the porous bulk with a highly conductive salt was successfully performed. A drawback of the low sintering temperature was that it extended the dwell time to 2 h instead of the 0.5 h as was used for sintering dense Na-β″-alumina electrolytes (Chapters 4.1 to 4.3.). A

long dwell time favors Na-diffusion and Na_2O sublimation. Therefore, the Na content within the bulk material must be adjusted to reach a competitive ionic conductivity in the future.

5. Conclusion and Outlook

5.1   Conclusion

The present work elucidates the effects of 3d transition metal doping on ceramic, lithium stabilized Na-β''-alumina electrolytes. Three dopants, namely TiO_2, Mn_3O_4, and NiO in various molar amounts, were analyzed for their effect on the synthesis and resulting properties of transition metal doped Na-β''-alumina electrolytes at three different sintering temperatures. The resulting electrolytes were characterized in respect of their phase content, sintering behavior, microstructure, characteristic fracture strength, and ionic conductivity. The work was complemented by introducing two battery application cases for doped Na-β''-alumina electrolytes.

The phase analysis of the doped electrolytes was performed by XRD and EDX. It was found that Ti-ions are not incorporating into the crystal lattice of Na-β''-alumina, but TiO_2 doping results in additional crystal phases like $NaLiTi_3O_7$ or $Na_{1.97}Al_{1.82}Ti_{6.15}O_{16}$. It was proven for the first time that TiO_2 is not a classical dopant but a sintering aid. Mn_3O_4 and NiO doping results in a doped Na-β''-alumina crystal lattice on the Al^{3+} positions and hence change lattice parameters. As expected, the lattice parameter a (= b) is increased, while the lattice parameter c is reduced by Mn_3O_4 or NiO doping. This observation is explicable by an increased occupation rate of Na-ion in the conduction plane and thereby increased electrostatic attraction between the spinel blocks and the conduction slab. This claim was supported by measuring the amount of Na-ions within the conduction slab.

After investigating the effects of the dopants on the Na-β''-alumina phase, I evaluated the microstructure of the electrolytes. The first finding was the influence of the sintering temperature. Undoped samples sintered at the lowest sintering temperature tested had fine uniform grains and a relative density of 98.6 %. In contrast, sintering temperatures of 1600 °C or 1700 °C caused excessive grain growth and reduced relative density, hence an increasing porosity. This effect was attributed to the sublimation of Na_2O at high temperatures and pore agglomeration. The addition of TiO_2 and thus the production of secondary phases greatly impacted the microstructure. It enabled low temperature liquid-assisted sintering and thereby made it possible to produce densely sintered Na-β''-alumina electrolytes with a relative density of 99.6 % at sintering temperatures as low as 1500 °C (by the addition of a mass fraction of 1 % TiO_2). A TiO_2 mass fraction of > 1.5 % at sintering temperatures of 1500 °C resulted in excessive grain growth and increased

porosity, a behavior observed at sintering temperatures of 1600 °C or 1700 °C in the case of undoped samples. This finding can be explained by the formation of compounds like $NaLiTi_3O_7$ or $Na_{1.97}Al_{1.82}Ti_{6.15}O_{16}$ that enable liquid-assisted sintering at temperatures of 1500 °C. In contrast to the addition of TiO_2, Mn_3O_4 and NiO addition did not lower the sintering temperature. However, it promoted a microstructure with small and homogenous grains that also persisted at higher sintering temperatures. Nevertheless, there was a change in the grain shape. At a sintering temperature of 1500 °C, the grains were flake-shaped. At higher sintering temperatures, the grains had a much rounder shape.

The influence of those mineralogical and microstructural changes on the performance parameters, namely the characteristic fracture strength and the ionic conductivity, were evaluated. Regarding the fracture strength, it was found that microstructural parameters influence phase parameters more strongly than the crystallographic. Larger grains and a higher porosity caused a low characteristic fracture strength. At the same time, other factors like the crystal lattice changes were less important. Since the microstructure is strongly influenced by all tested dopants, they all greatly influence the characteristic fracture strength. TiO_2 doping increased the characteristic fracture strength only on low doping amounts, while high doping amounts produced excessive grain growth and, hence, lowered characteristic fracture strength. The highest value of 269 MPa was reached by a mass fraction of 0.5 % TiO_2 and a low sintering temperature of 1500 °C.

In contrast, Mn_3O_4 and NiO also increased the characteristic fracture strength at higher doping amounts and higher sintering temperatures. The maximum of 296 MPa was reached at a sintering temperature of 1600 °C and a mass fraction of 1.5 % NiO. This finding was also explained by microstructural changes, namely the small grain and low porosity.

The primary influence on the ionic conductivity proved to be the microstructure. This was more important than material properties such as phase content, occupation ratio, and grain orientation. Larger grains – and thereby fewer grain boundaries to cross – enhance ionic conductivity. The presence of pores lengthens the conductive pathways through the electrolyte and hence reduces ionic conductivity. A microstructure with large grains but a small number of pores was produced by doping with a mass fraction of 1.5 % TiO_2 and applying a sintering temperature of 1500 °C. The ionic conductivity measured for this sample was 0.30 S cm^{-1} at 300 °C. In the case of Mn_3O_4 and NiO doping, the sintering temperature was more influential than the doping amount. Higher sintering temperatures

resulted in higher ionic conductivities caused by larger grains and differently shaped grains.

In conclusion, characterizing the doped Na-β″-alumina electrolytes indicates that smaller grains support the characteristic fracture strength and lowers the ionic conductivity, but larger grains increase ionic conductivity but reduce the characteristic fracture strength. The favored compromise consisted of adding small amounts of TiO_2 in combination with a sintering temperature of 1500 °C instead of the state-of-the-art temperature of 1600 °C. Electrolytes of this type had better fracture strength and ionic conductivity and the lower temperature reduced the energy consumption of sintering.

Two demonstration cases were investigated to prove the stability and workability of TiO_2 doped Na-β″-alumina electrolytes. On the one hand, the application in electrochemical cells was tested, and on the other, the possibility of synthesizing a bilayer electrolyte.

The cell testing was carried out by using two different setups. First, a Na || Na-β″-alumina || Na-symmetrical cell was tested, and afterwards a Na/NiCl$_2$-full-cell. A post-mortem analysis revealed no changes or anomalies in the electrolyte. This experiment is the first indication that the secondary phases caused by TiO_2 do not restrict the manufacturability or stability of the electrolyte.

TiO_2 addition was furthermore used to produce bilayer electrolytes. These electrolytes consisted of a porous bulk layer made from an Al_2O_3/Na-β-alumina-mixture and a dense layer made from TiO_2 doped Na-β″-alumina. The bulk layer provides the mechanical strength while the dense layer prevents shortcuts and is a separator and electrolyte. The TiO_2 addition to the dense Na-β″-alumina layer was crucial in synthesizing the electrolyte to prevent a collapse of the pore system within the bulk layer due to high sintering temperatures. The aim was to reduce the overall conductivity of the electrolyte by this technique. Unfortunately, the ionic conductivity of the bilayer electrolytes did not exceed 0.1 S cm^{-1} at 300 °C. The main reason for this low value was the low Na-content in the porous bulk. Nevertheless, this test provided proof-of-concept for this novel type of Na-β″-alumina electrolyte.

This thesis showed that 3d transition metal doping of Na-β″-alumina electrolytes is an effective method for adjusting electrolyte properties. And such adjustments enable novel bilayer-electrolyte designs. Furthermore, reducing the necessary sintering temperature to

produce highly conductive thin-walled, stable, and cheap Na-β″-alumina electrolytes greatly strengthens the competitiveness of Na/NiCl$_2$ and NaS-batteries.

5.2 Outlook

The outlook for future research regarding transition metal doping for Na-β″-alumina electrolytes is divisible into two branches.

The first branch is the implementation of a commercial product. The most promising candidate is TiO$_2$ since it not only enhances the fracture strength and the ionic conductivity but lowers the sintering temperature and hence reduces the energy consumption of the production process. Applying TiO$_2$ as a sintering aid for Na-β″-alumina electrolytes seems more likely in usual Na-β″-alumina electrolytes than in bilayer electrolytes. The transfer of the findings into commercial Na-β″-alumina electrolytes is already in preparation. The initial steps for this project were already done by producing TiO$_2$ doped Na-β″-alumina on a larger scale using a spraying tower, a large ball mill, *etc.* and applying a sintering temperature of 1500 °C instead of the 1600 °C used previously in the commercial production process of *Fraunhofer IKTS*. The very uniform microstructure of the electrolyte that results is displayed in Figure 55. In the near future, experiments on the long-term stability and the maximal current density of these electrolytes will reveal if it is possible to produce Na-β″-alumina electrolytes with lower energy consumption of the sintering process commercially.
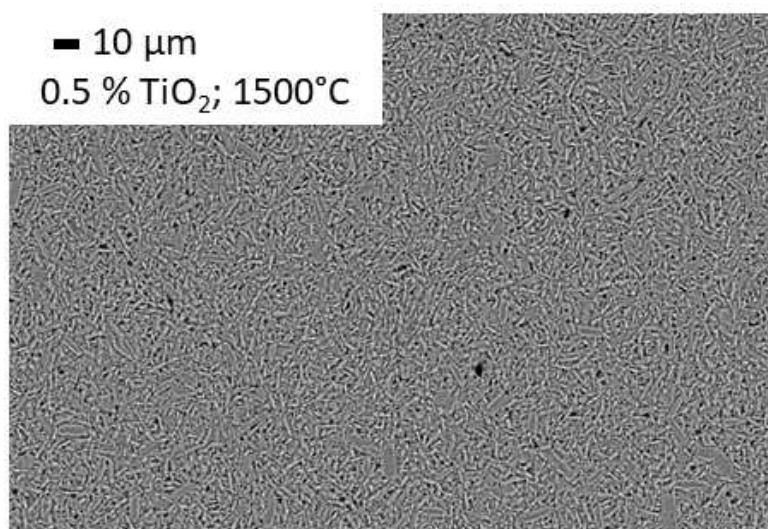
Figure 55. SEM image of a Na-β″-alumina sample, produced in a large batch, sintered at 1500 °C and doped with a mass fraction of 0.5 % TiO$_2$ after polishing and thermal etching.

In addition to commercial exploitation of the results presented here, the work also suggests some scientific topics for further research on transition metal doping of lithium stabilized Na-β″-alumina. An obvious topic for further research is to explore the effect of other metal oxides like CuO or Fe_2O_3 on Na-β″-alumina. A theoretical evaluation of the effects of different ions could help choose the most promising candidates. Another interesting topic is using mixtures of several dopants. For example, a combination of TiO_2 as a sintering aid and ZrO_2 as an inert secondary phase, that increases the characteristic fracture strength of Na-β″-alumina electrolytes. Simulation approaches using DFT (Discrete *Fourier* transformation) and finite elements might be able to provide more insights into the effects of transition metal doping of Na-β″-alumina. In addition, however, this topic also requires experiments with Na-β″-alumina single crystals. My work shows that it is hard to quantify the effects of changes in the crystal lattice because microstructural changes are the dominant factor. Characterizing single crystals circumvents this difficulty because single crystals are not subject to the microstructure effects of porosity and grain size. Single crystal studies therefore clearly separate the effects of microstructure from those of the crystal lattice. Another topic for investigation is the evaluation of the activation energy of Na^+ transportation process of the differently doped Na-β″-alumina by ^{23}Na NMR (nuclear magnetic resonance) spectroscopy. This topic is being pursued in cooperation with Prof. *Wark* from the *Carl von Ossietzky University Oldenburg*. Because the ^{23}Na NMR measurements are carried out on powders, there are no grain boundary effects to be taken into account. It is then possible to compare the activation energies calculated in this way with those calculated by substituting into the *Arrhenius equation* the ionic conductivities measured at different temperatures from solid Na-β″-alumina electrolytes. The difference between the two methods of calculation gives the extent to which microstructure influences conductivity.

6. Zusammenfassung auf Deutsch

Die vorliegende Arbeit befasst sich mit der 3d-Übergangsmetall Dotierung von keramischen, Li^+-stabilisierten Na-β″-Aluminat. Das Hauptanwendungsfeld für das natriumionenleitende Na-β″-Aluminat sind Festelektrolyte in bereits kommerziell erhältlichen $Na/NiCl_2$- und Na/S-Batterien, die ihr Einsatzgebiet vor allem in stationären Energiespeichersystemen haben. Beide Technologien nutzen jeweils eine Negativelektrode aus flüssigem Natrium und unterscheiden sich primär im Positivelektroden-Material. Beide Batterietypen haben eine Betriebstemperatur von 250 °C bis 350 °C. Diese hohe Temperatur ist unteranderem notwendig, um eine ausreichende ionische Leitfähigkeit des Na-β″-Aluminats und eine vollständige Benetzung der Elektrolytoberfläche mit Natrium zu gewährleisten. Um Druckschwankungen durch Temperaturänderungen und Zyklierung innerhalb der Einzelzellen standzuhalten, benötigen die Na-β″-aluminat-Elektrolyte eine ausreichend hohe Bruchfestigkeit. Um diese zu erreichen, werden kommerzielle, tubuläre Na-β″-aluminat-Elektrolyte mit einer Wandstärke zwischen 1.5 und 2 mm gefertigt. Dem gegenüber steht der Wunsch nach minimalen Innenwiderständen und damit möglichst dünnwandigen Elektrolyten. Eine Möglichkeit die charakteristische Bruchfeste von Na-β″-aluminat zu erhöhen und damit dünnwandigere Elektrolyte zu ermöglichen ist die Dotierung mit 3d-Übergangsmetallen. Neben der Bruchfestigkeit wirken sich die Dotierungen mitunter auch positiv auf die ionische Leitfähigkeit der Elektrolyte aus. Dennoch fanden bisher nur wenige systematische Untersuchungen bezüglich 3d-Übergangsmetall-dotiertem Na-β″-Aluminat statt, wie im Kapitel 2 der vorliegenden Arbeit dargelegt wird. Ziel der Arbeit war es diese Wissenslücken zu füllen.

Anhand des Stands der Technik wurden drei 3d-Übergangsmetalloxide hinsichtlich ihrer Auswirkung auf Na-β″-aluminat ausgewählt. Diese sind TiO_2, Mn_3O_4 und NiO. Es wurden Na-β″-Aluminat Proben mit einem Massenanteil von 0,5 %; 1,0 %; 1,5 %; 2,0 %; 2,5 % und 5,0 % des jeweiligen Metalloxids hergestellt und bei Temperaturen von 1500 °C, 1600 °C und 1700 °C gesintert. Anschließend wurden die Proben ausführlich charakterisiert.

Zunächst wurde der Phasenbestandteil von dotiertem Na-β″-aluminat in den Proben mittels XRD und anschließender *Rietveld*-Analyse bestimmt. Dabei stellte sich heraus, dass durch Dotierungen und Variation der Sintertemperatur keine große Schwankung des Phasengehalts zu verzeichnen war. Der Anteil der Hauptphase lag bei allen Proben stabil bei circa 95 % Na-β″-Aluminat. Die zwei Nebenphasen, denen die übrigen 5 %

zuzuordnen waren, waren $NaAlO_2$ und Na-β-aluminat. Erst bei hohen Sintertemperaturen von 1700 °C und einem Dotierungsgrad von einem Massenanteil von 2,0 % TiO_2 oder einem hohen Dotierungsgrad von einem Massenanteil von 5,0 % TiO_2 und einer Sintertemperatur von 1600 °C wurden außerdem die Phasen $NaLiTi_3O_7$ and $Na_{1.97}Al_{1.82}Ti_{6.15}O_{16}$ nachgewiesen. Weiterhin wurden die Gitterkonstanten des Na-β″-Aluminats bestimmt. TiO_2 dotierte Proben wiesen keine von der Dotierung abhängigen Veränderungen auf, während Mn_3O_4 und NiO dotierte Proben eine Erhöhung des Gitterparameters a (=b) und eine Absenkung des Gitterparameters c aufwiesen. Die Erhöhung des Gitterparameters a wurde auf den größeren Ionenradius der Dotierungsionen zurückgeführt, welche in das Kristallgitter eingebaut wurden. Die Absenkung des Gitterparameters c konnte mit einer Erhöhung des Besetzungsgrades von Na-Ionen in der Leitungsebene und einer damit einhergehenden verstärkten elektrostatischen Interaktion zwischen der positiv geladenen Leitungsebene und den negativen Spinellblöcken erklärt werden. Der höhere Na^+-Besetzungsgrad wurde durch das Ersetzen von Al^{3+} durch Mn^{2+} beziehungsweise Ni^{2+} bei gleichzeitig zu erhaltender Ladungsneutralität ermöglicht.

Um den Verbleib der Metallionen weiter aufzuklären, wurden EDX-Messungen angefertigt. Dabei bestätigte sich eine gleichmäßige Verteilung von Mn- und Ni im Gefüge. Ti-Peaks konnten in niedrig dotierten Proben nicht gemessen werden, während höhere Dotierungsgerade deutlich sekundäre Ti-haltige Phasen zeigten, während sich das übrige Gefüge aus Na-β″-Aluminat Ti-frei darstellte. Die quantitative Auswertung der Sekundärphasenzusammensetzung stimmte gut mit der Zusammensetzung der im XRD gemessenen Phasen überein. Aufgrund dieser Messergebnisse kann postuliert werden, dass TiO_2 als Additiv Nebenphasen bildet, während Mn_3O_4 und NiO zu einer Dotierung des Kristallgitters von Na-β″-Aluminat führen.

Es wurde weiter mittels REM überprüft, wie und ob sich die Nebenphasen und Dotierungen auf das Gefüge der Na-β″-Aluminat-Elektrolyte auswirken. Es konnte festgestellt werden, dass Mn_3O_4 und NiO Dotierungen auch bei höheren Sintertemperaturen zu kleineren Kristalliten im Elektrolytgefüge führen, während eine hohe Sintertemperatur bei undotierten Proben zu sehr großen Kristalliten und einer deutlich erhöhten Porosität führten. Die mit TiO_2 versetzten Proben zeigten schon bei niedrigen Sintertemperaturen von 1500 °C eine deutlich erhöhte Sinteraktivität und ein starkes Kristallitwachstum. Die Verschiebung hin zu niedrigen Sintertemperaturen konnte mit dem Effekt der Flüssigphasensinterung, ermöglicht durch die Nebenphasen, erklärt

werden. Diese These konnte mittels DSC-Messung, die das Entstehen einer flüssigen Phase zeigt, bestätigt werden.

Des Weiteren wurde die Auswirkung der Metalloxid-Dotierungen auf die charakteristische Bruchfestigkeit und die ionische Leitfähigkeit der Na-β''-aluminat-Elektrolyte getestet. Die Bruchfestigkeit nahm generell mit steigender Sintertemperatur ab. Dies korreliert mit der zunehmenden Kritallitgröße und der steigenden Porosität. Mn_3O_4 und NiO Dotierungen, die für eine Inhibierung des Kristallitwachstums sorgten, ließen die Bruchfeste auf bis zu 296 MPa steigen. Geringe Mengen TiO_2 sorgten für eine steigende Bruchfeste von bis zu 259 MPa durch die erhöhte Sinteraktivität, während höhere Dotierungsgeradefür ein starkes Abfallen der Bruchfestigkeit sorgte. Ursächlich hierfür waren das Kristallitwachstum und die steigende Porosität.

Die ionische Leitfähigkeit steigt – im Gegensatz zur Bruchfestigkeit – mit steigender Kristallitgröße, da weniger Korngrenzen überwunden werden müssen. Porosität wirkt sich dagegen negativ aus, da die mittlere Weglänge für den Ionentransport steigt. Diese Zusammenhänge bestimmen die gemessenen ionischen Leifähigkeiten und decken sich mit den Beobachtungen der REM-Aufnahmen. TiO_2-Dotierung führt in geringeren Konzentrationen von 1,5 % TiO_2 zu einem deutlichen Anstieg der ionischen Leitfähigkeit auf bis zu 0.30 S cm^{-1} bei 300 °C. Bei höheren Dotierungsgraden erfolgt jedoch einAbfall, welcher durch eine steigende Porosität und durch Nebenphasen, die den Leitungspfad behindern, erklärt werden kann. Die Zunahme der ionischen Leitfähigkeit im Vergleich zu undotierten Proben ist besonders bei niedrigen Sintertemepraturen zu beobachten, da durch das Flüssigphasensintern schon bei niedrigen Sintertemperaturen geringe Porositäten erreicht werden. Mn_3O_4 und NiO Dotierungen bewirken nur eine geringe Steigerung der ionischen Leitfähigkeit. Hierfür sind zwei gegenläufige Effekte verantwortlich: Ein erhöhter Besetzungsgrad in der Leitungsebene des Kristallgitters durch Na-Ionen kann die ionische Leitfähigkeit steigern, während sich die geringere Kristallitgröße negativ auf diese auswirkt. Im Fall der Mn- und Ni-Dotieren überwog der letztgenannte Aspekt.

Es lässt sich resümieren, dass geringe Mengen TiO_2 als Additiv sowohl die charakteristische Bruchfestigkeit als auch die ionische Leitfähigkeit der Na-β''-aluminat-Elektrolyte steigert. Dies konnte mit Veränderungen im Gefüge erklärt werden. Weiter ermöglichte das TiO_2 auch eine Reduktion der Sintertemperatur um 100 °C. Diese Temperatur wird benötigt, um eine ionische Leitfähigkeit von 0.30 S cm^{-1} bei 300 °C und eine charakteristische Bruchfeste von über 250 MPa zu erreichen, Mn_3O_4 und NiO

Dotierungen wirkten sich dagegen hauptsächlich auf die charakteristische Bruchfeste der Elektrolyte aus.

Um die Funktionalität der TiO_2-Beimischung zu in praktischen Anwendungen zu testen, wurden die Elektrolyte zum einen in einer symmetrischen Natrium-Natrium Halbzelle und einer Na/$NiCl_2$-Vollzelle erprobt. Zum anderem wurde sie verwendet, um einen Bilayer-Elektrolyten herzustellen.

Die Na/$NiCl_2$-Zelle mit einem Na-β″-aluminat-Elektrolyt, der mit einem Massenanteil von 1,0 % TiO_2 synthetisiert wurde, ist bei verschiedenen Entladeströmen über insgesamt 100 Zyklen betrieben worden. Bei einer sich anschließenden Post-mortem Analyse konnten keine Veränderungen am Elektrolyten festgestellt werden. Dieses Experiment lieferte erste Indizien, dass die im Elektrolyten vorhanden Ti-haltigen Nebenphasen nicht zu einer Einschränkung der elektrochemischen oder chemischen Stabilität führen.

Ein weiteres Anwendungsbeispiel für TiO_2 als wirkungsvolles Sinteradditiv für Na-β″-aluminat-Elektrolyte wurde mit der Synthese eines Bilayer-Elektrolyten dargelegt. Dabei wurde ein hoch poröse Trägerstruktur (Bulk) einseitig mit einer dünnen Schicht aus Na-β″-aluminat überzogen. Die poröse Trägerstruktur soll die notwendige mechanische Integrität des Bilayer-Elektrolyten gewährleisten. Um den porösen Träger aus einem Al_2O_3/Na-β-aluminat/Na-β″-aluminat-Gemisch mit der dünnen Schicht aus Na-β″-aluminat zu verbinden werden hohe Sintertemperaturen benötigt. Hohe Sintertemperaturen führen wiederum zu einer deutlichen Abnahme der Poren in der Trägerstruktur/Bulk. Erst durch die Dotierung mit TiO_2 in der dichten Schicht und damit einer Absenkung der Sintertemperatur auf 1400 °C konnte der Verlust der Porosität verhindert werden. Die so hergestellten Bilayer-Elektrolyte wiesen eine ionische Leitfähigkeit von 0,1 S cm^{-1} bei einer Temperatur von 300 °C auf, was deutlich unter dem Niveau eines konventionellen Na-β″-aluminat-Elektrolyten liegt. Dennoch konnte der Proof of Concept erbracht werden. Um in Zukunft höhere ionische Leitfähigkeiten zu erreichen, wurde eine Erhöhung des Na-β″-aluminat-Phasenanteils im poröser Trägerstruktur/Bulk mittels VPC diskutiert.

Es lässt sich festhalten, dass die vorliegende Arbeit die Effekte von TiO_2, Mn_3O_4 und NiO auf Li$^+$-stabilisierte Na-β″-aluminat-Elektrolyte erstmals systematisch untersucht und belegt das in der Literatur bereits postulierte, aber nicht nachgewiesene, Flüssigphasensintern durch TiO_2-Beimischung. Die charakteristische Bruchfestigkeit konnte durch alle getesteten Metalloxide erhöht werden, während die ionische

Leitfähigkeit besonders von TiO$_2$-Dotierungen profitierte. Sowohl die steigende Bruchfestigkeit als auch die steigende ionische Leitfähigkeit wurde primär auf Änderungen im Gefüge zurückgeführt. Zum Abschluss der Arbeit wurden zwei Anwendungsbeispiele für mit TiO$_2$-versetzte Na-β″-aluminat-Elektrolyte vorgestellt. Zum einem wurde die Funktionalität über 100 Zyklen in einer Na/NiCl$_2$-Zelle demonstriert und zum anderem die Möglichkeit, dünne Na-β″-aluminat Schichten bei niedrigeren Temperaturen zu sintern.

7. Theses

1. The addition of TiO_2 leads to the formation of compounds like $NaLiTi_3O_7$ or $Na_{1.97}Al_{1.82}Ti_{6.15}O_{16}$ during the sintering process of Na-β″-alumina electrolytes. Those compounds enable liquid-assisted sintering at temperatures under 1500 °C. Ti is not incorporated into the crystal lattice. Consequently, Ti acts as a sintering aid and not as a dopant.

2. Due to the liquid-assisted sintering process at lower temperatures – enabled by the addition of TiO_2 – lower sintering temperatures of only 1500 °C instead of 1600 °C at the same dwelling time are needed to obtain a Na-β″-alumina electrolyte with a sufficient density of > 95 %.

3. Addition of TiO_2 leads to microstructural changes, which, enhance the characteristic fracture strength and the ionic conductivity of Na-β″-alumina electrolytes.

4. TiO_2 addition lead not to degradation in symmetric Na|TiO_2 doped Na-β″-alumina|Na -cells nor on $Na/NiCl_2$ cells

5. Furthermore, the addition of TiO_2 reduced the sintering temperature necessary to properly join the two layers of a bilayer electrolyte. Only by this temperature reduction, the high porosity of the bulk layer stayed intact.

6. The addition of Mn_3O_4 and NiO does not result in additional phases that enable low temperature liquid-assisted sintering of Na-β″-alumina electrolytes. Both transition metals are incorporated into the Na-β″-alumina crystal lattice.

7. Mn_3O_4 or NiO addition inhibits excessive grain growth in Na-β″-alumina electrolytes, thereby increases the characteristic fracture strength. The addition barely influences the electrolytes' ionic conductivity and the Na-β″-alumina phase content

8. Appendix

8.1 Additional Figures and tables
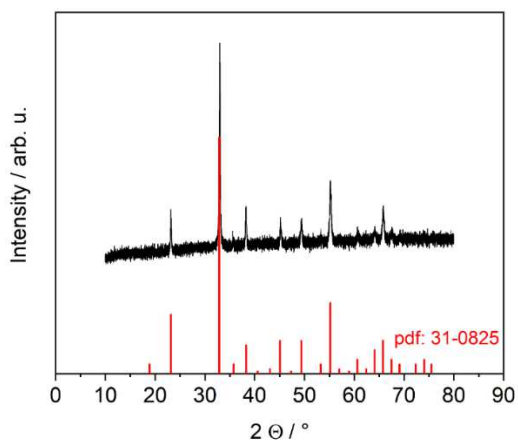
Figure 56. XRD pattern of Mn_3O_4 and literature peaks (bottom).
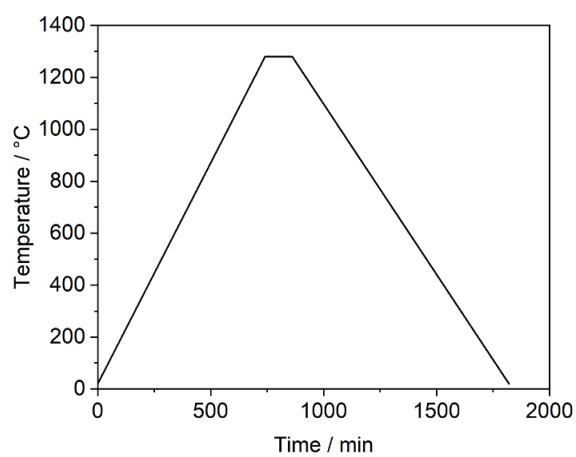
Figure 57. Calcination temperature regime to produce Na-β''-alumina powder.
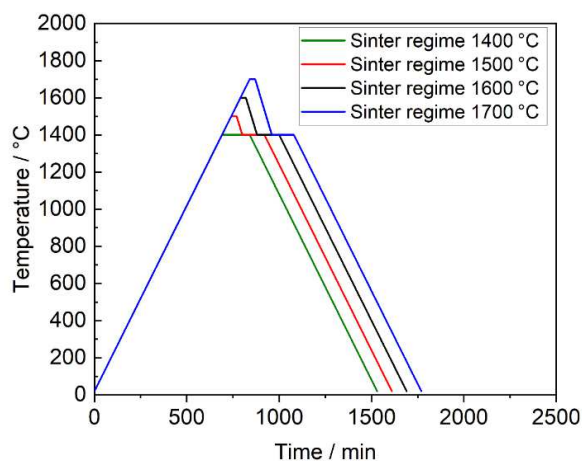
Figure 58. Sinter regimes for sintering Na-β″-alumina electrolytes at 1400, 1500, 1600, or 1700 °C. The temperature peak is held for 30 min. 1400 °C is held for 120 min. The samples sintered at 1400 °C were held at 1400 °C for 150 minutes. All temperature ramps are 2 K min^{-1}.
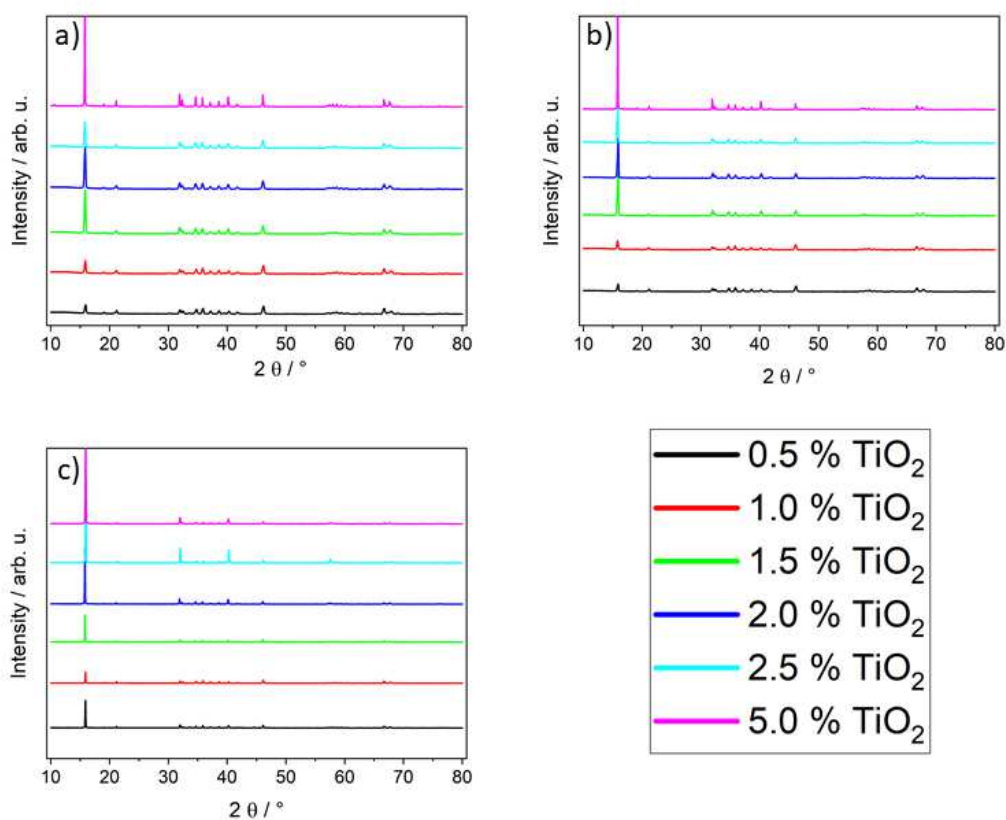
Figure 59. Diffraction patters of TiO_2 doped Na-β″-alumina at a) 1500 °C; b) 1600 °C; c) 1700 °C. The peak 006 (15.8 °) is clipped off at mass fractions of 5.0 % TiO_2.
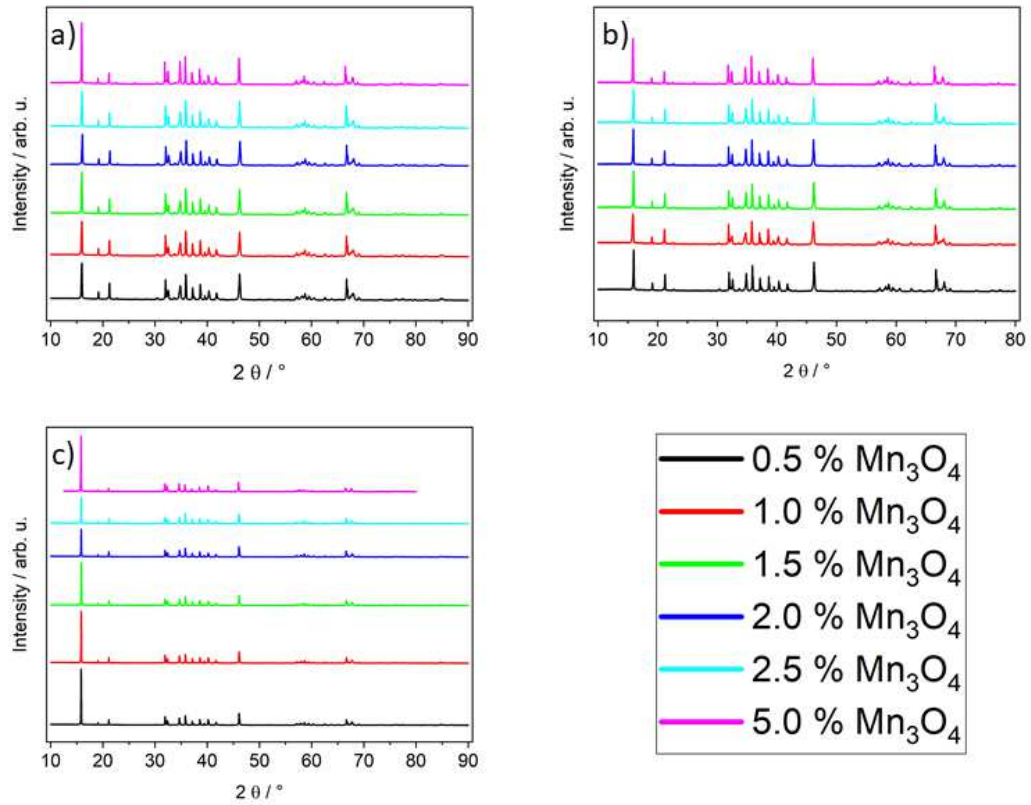
Figure 60. Diffraction patters of Mn_3O_4 doped Na-β"-alumina at a) 1500 °C; b) 1600 °C; c) 1700 °C.
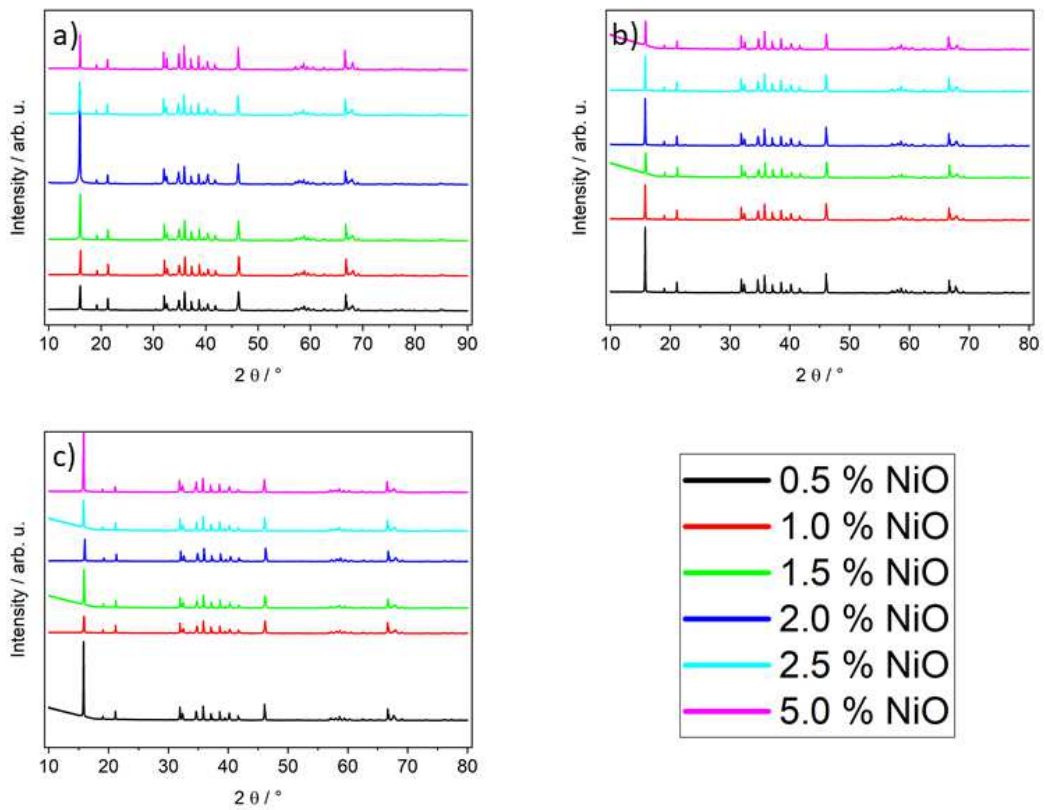
Figure 61. Diffraction patters of NiO doped Na-β"-alumina at a) 1500 °C; b) 1600 °C; c) 1700 °C.
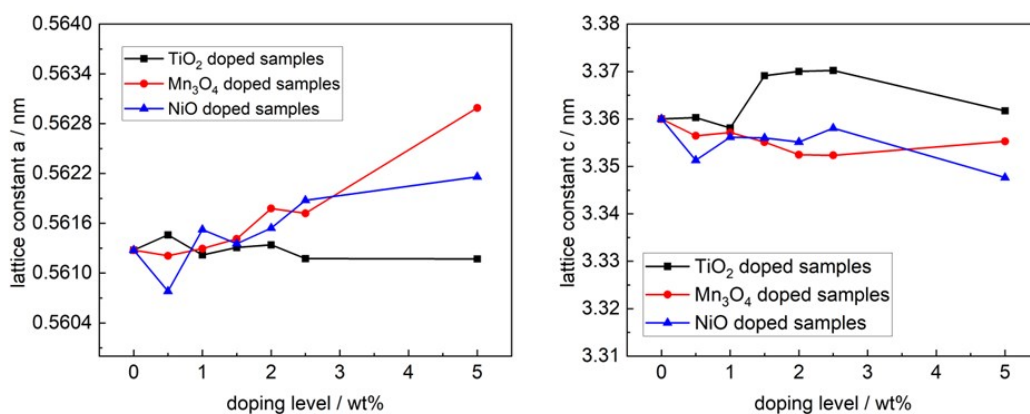
Figure 62. Crystallographic lattice parameters a (=b) and c of Na-β″-alumina samples sintered at 1500 °C. Percentages indicate mass fractions.
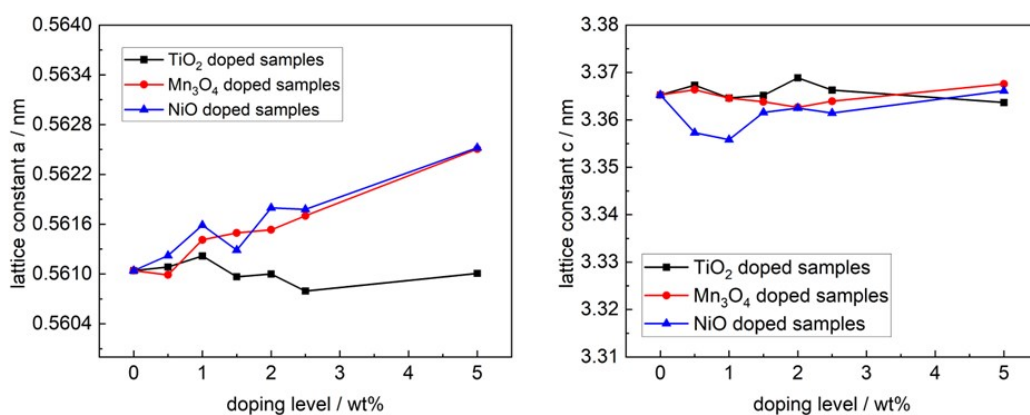
Figure 63. Crystallographic lattice parameters a (=b) and c of Na-β″-alumina samples sintered at 1700 °C. Percentages indicate mass fractions.
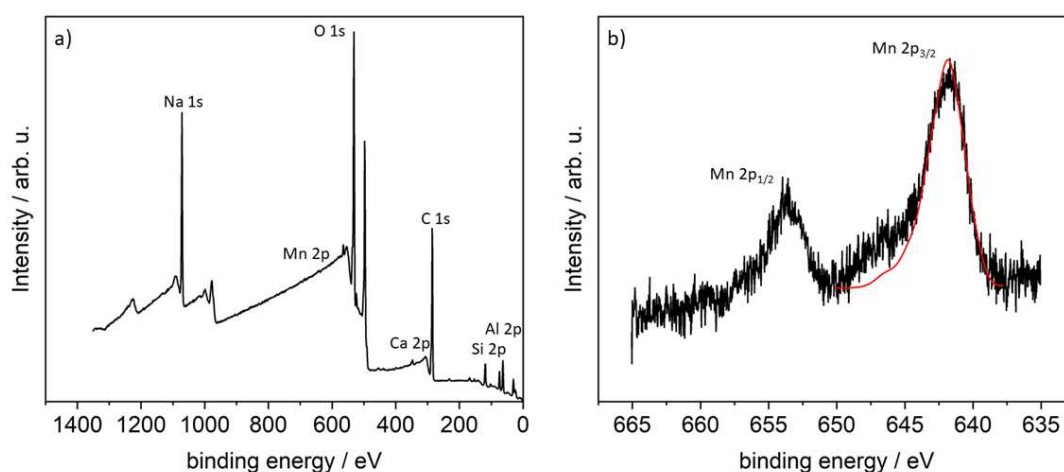
Figure 64. XPS-spectra of a polished, Mn_3O_4 doped Na-β″-alumina electrolyte (Mass fraction of 5 %; sintered at 1600 °C). a) overview spectrum b) black line: detail spectrum; red line: fit to estimate the amount of Mn^{2+} and Mn^{3+}.

106
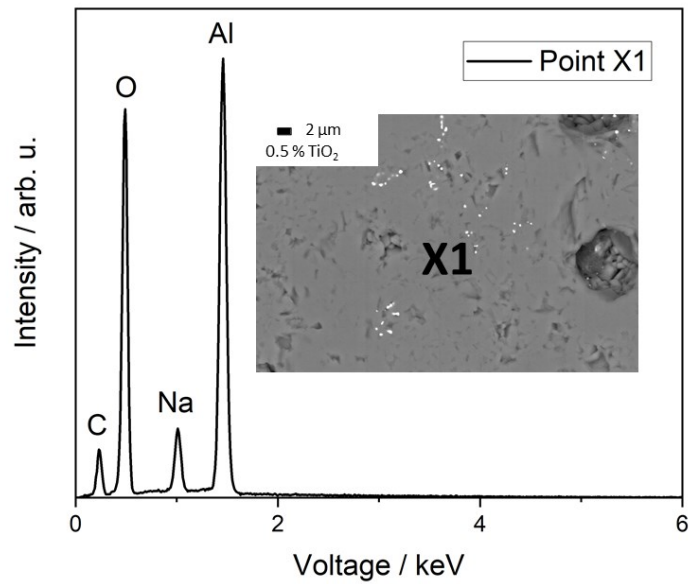
Figure 65. EDX point analysis of a Na-β''-alumina sample doped with a mass fraction of 0.5 % TiO_2 (sintered at 1600 °C). The measuring point is marked in the backscattering-SEM image. The measured composition on point X1 is $Na_{1.42}Al_{10.86}O_{17}$. Ti was undetected. The bright phase is ZrO_2 originating from milling gear.
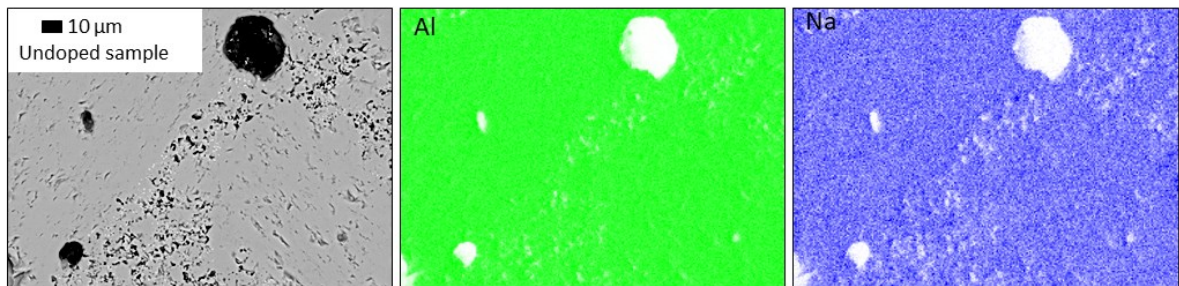
Figure 66. EDX mapping and backscattering SEM image of an undoped, polished Na-β''-alumina sample (sintered at 1600 °C). Al is labeled green; Na is labeled blue.
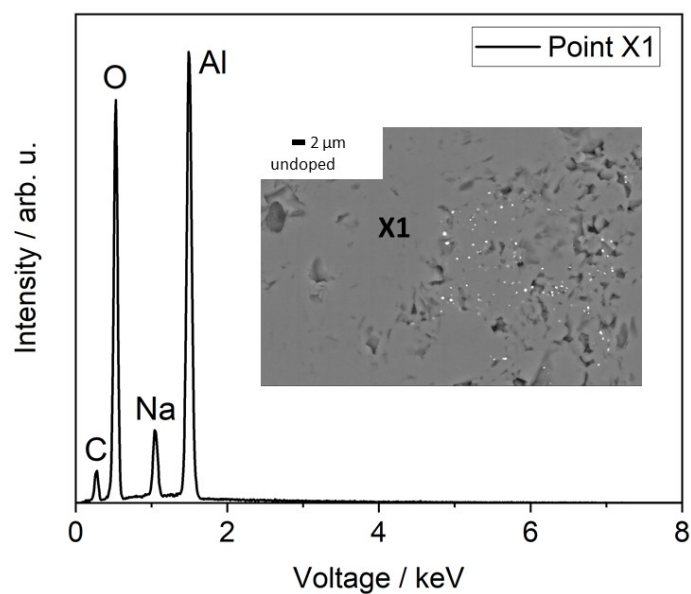
Figure 67. EDX point analysis of an undoped Na-β''-alumina sample (sintered at 1600 °C). The measuring point is marked in the backscattering-SEM image. The measured composition on point X1 was $Na_{1.47}Al_{10.84}O_{17}$. ZrO_2 causes the bright points within the SEM image.
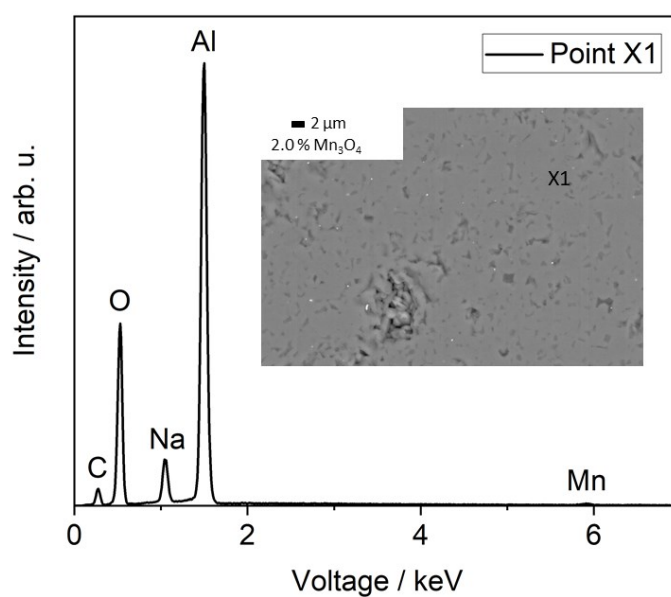
Figure 68. EDX point analysis of a Na-β''-alumina sample doped with a mass fraction of 2.0 % Mn_3O_4 (sintered at 1600 °C). The measuring point is marked in the backscattering-SEM image. The measured composition on point X1 is $Na_{1.34}Mn_{0.13}Al_{10.75}O_{17}$.
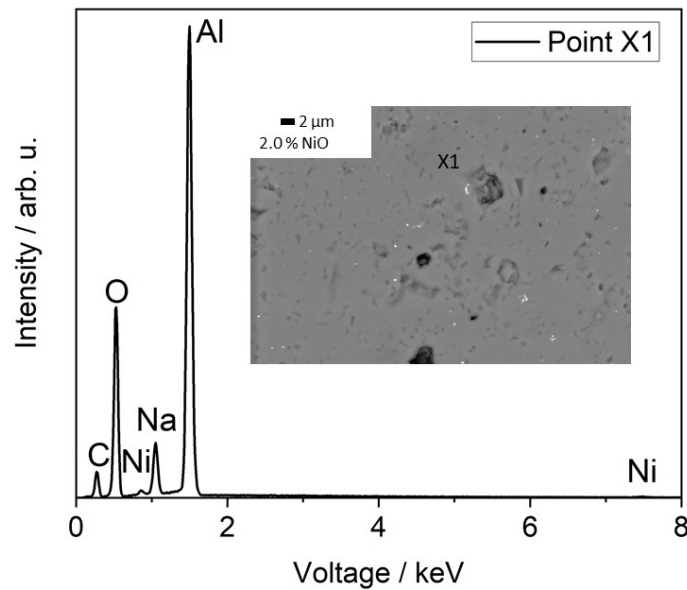
Figure 69. EDX point analysis of a Na-β″-alumina sample doped with a mass fraction of 2.0 % NiO (sintered at 1600 °C). The measuring point is marked in the backscattering-SEM image. The measured composition on point X1 is $Na_{1.41}Ni_{0.15}Al_{10.77}O_{17}$.
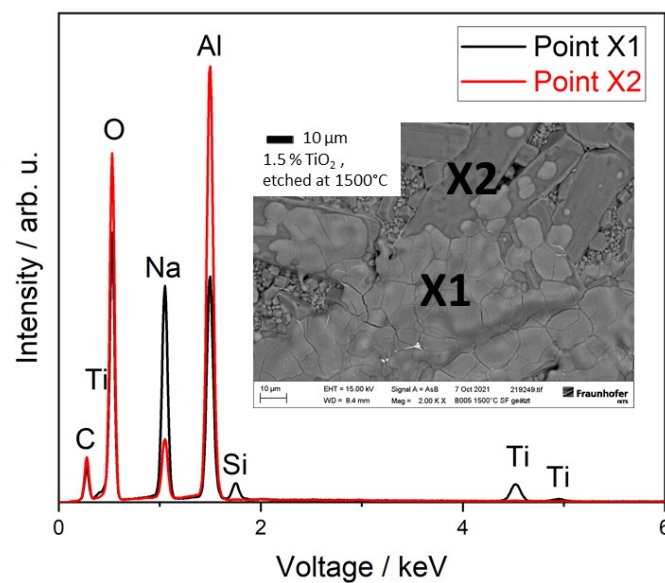
Figure 70. EDX point analysis of a Na-β″-alumina sample doped with a mass fraction of 1.5 % TiO_2 (sintered at 1600 °C). The surface was furthermore polished and thermally etched at 1500 °C. The measuring point is marked in the SEM image. The measured composition on point X1 is $Na_{7.2}Ti_{1.0}Al_{6.9}Si_{0.6}O_{17,}$ and X2 is $Na_{1.9}Al_{10.7}O_{17}$. The Si-peak was most certainly caused by polishing.
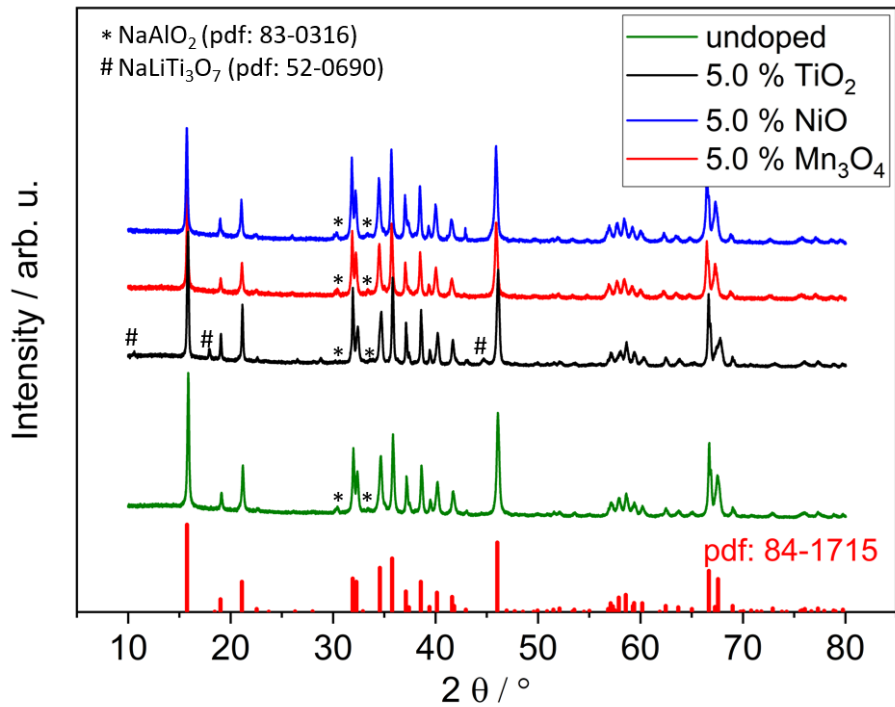
Figure 71. Diffraction patterns of Na-β″-alumina sample undoped or doped with a mass fraction of 5.0 % TiO$_2$, Mn$_3$O$_4$ or NiO. The sample were removed at a temperature of 1200 °C from the oven to quench the crystal phases.
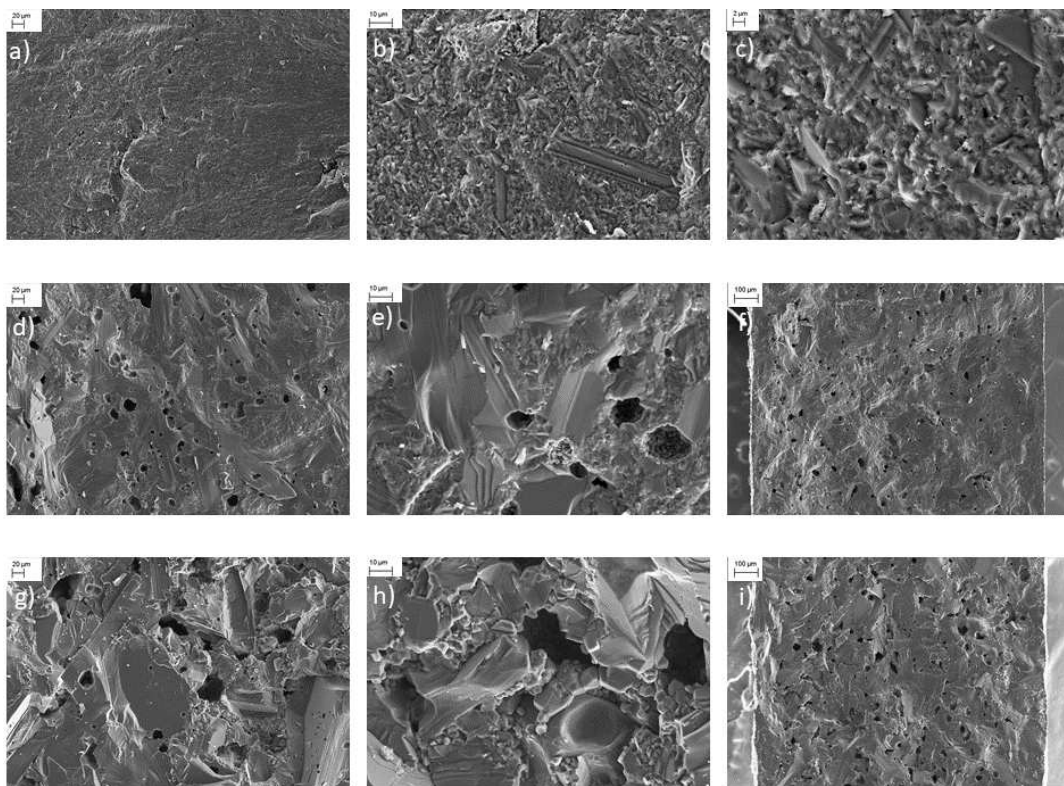
Figure 72. SEM images of undoped Na-β″-alumina a)-c) sintered at 1500 °C; d)-f) sintered at 1600 °C; g)-i) sintered at 1700 °C.
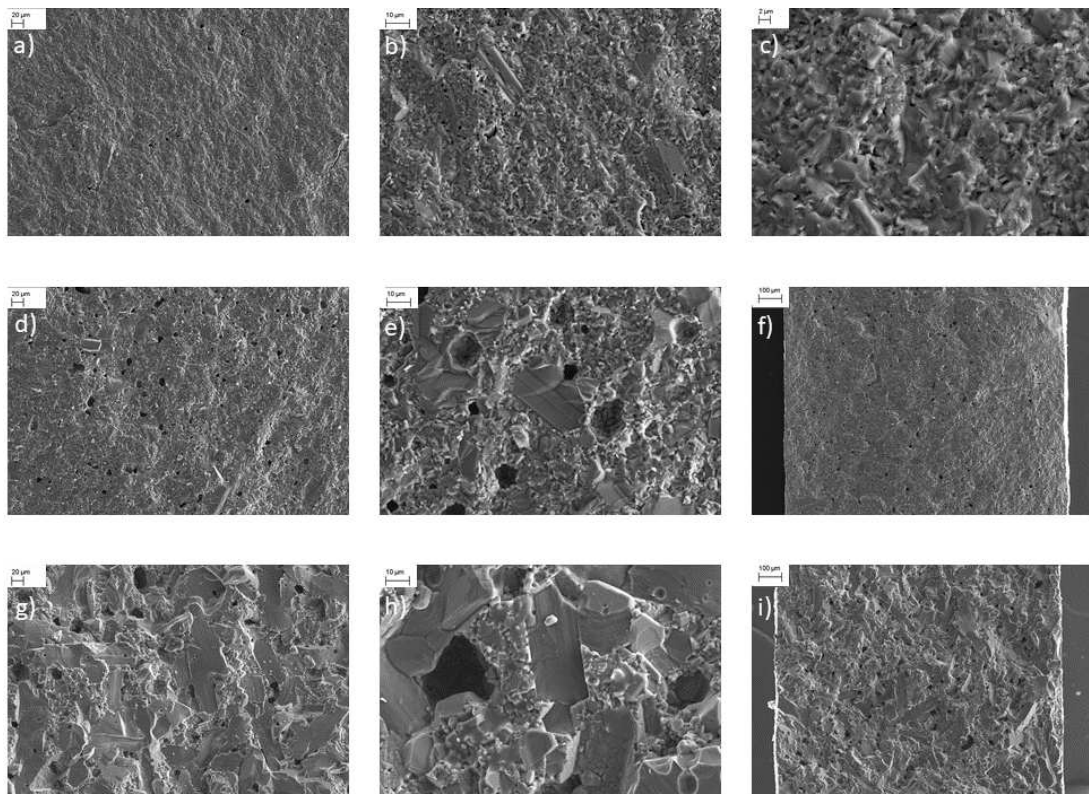
Figure 73. SEM images of Na-β″-alumina doped with a mass fraction of 0.5 % TiO$_2$ a)-c) sintered at 1500 °C; d)-f) sintered at 1600 °C; g)-i) sintered at 1700 °C.
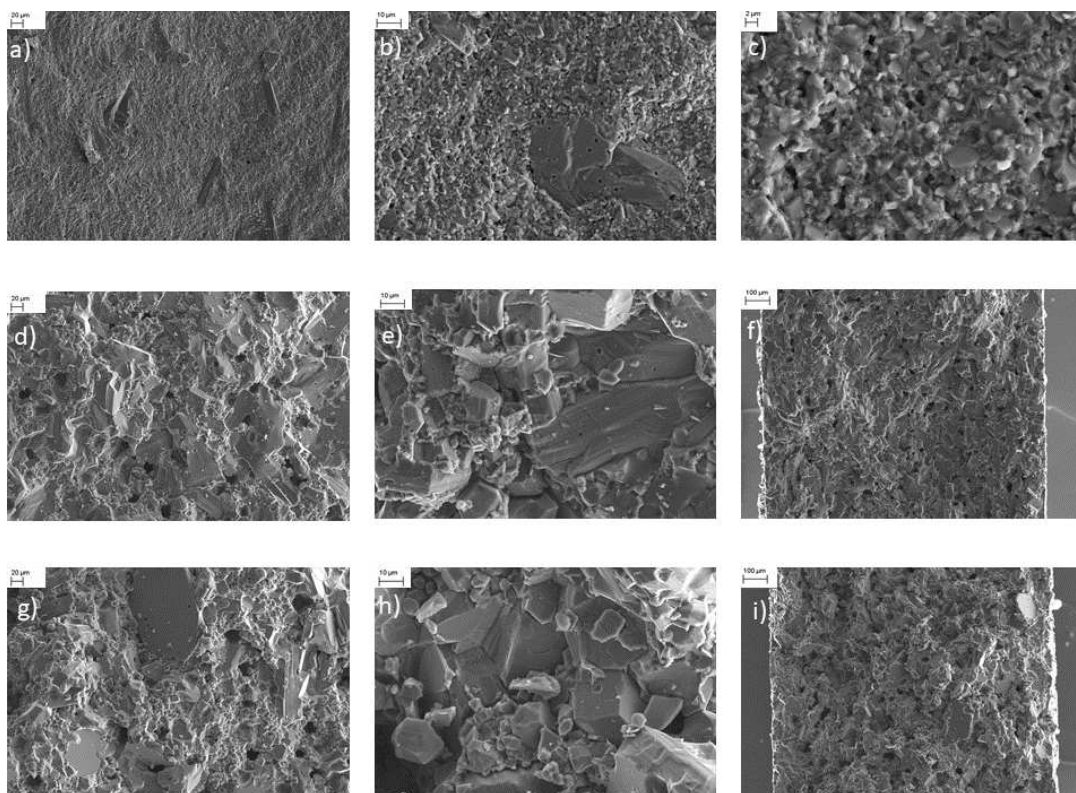
Figure 74. SEM images of Na-β″-alumina doped with a mass fraction of 1.0 % TiO$_2$ a)-c) sintered at 1500 °C; d)-f) sintered at 1600 °C; g)-i) sintered at 1700 °C.
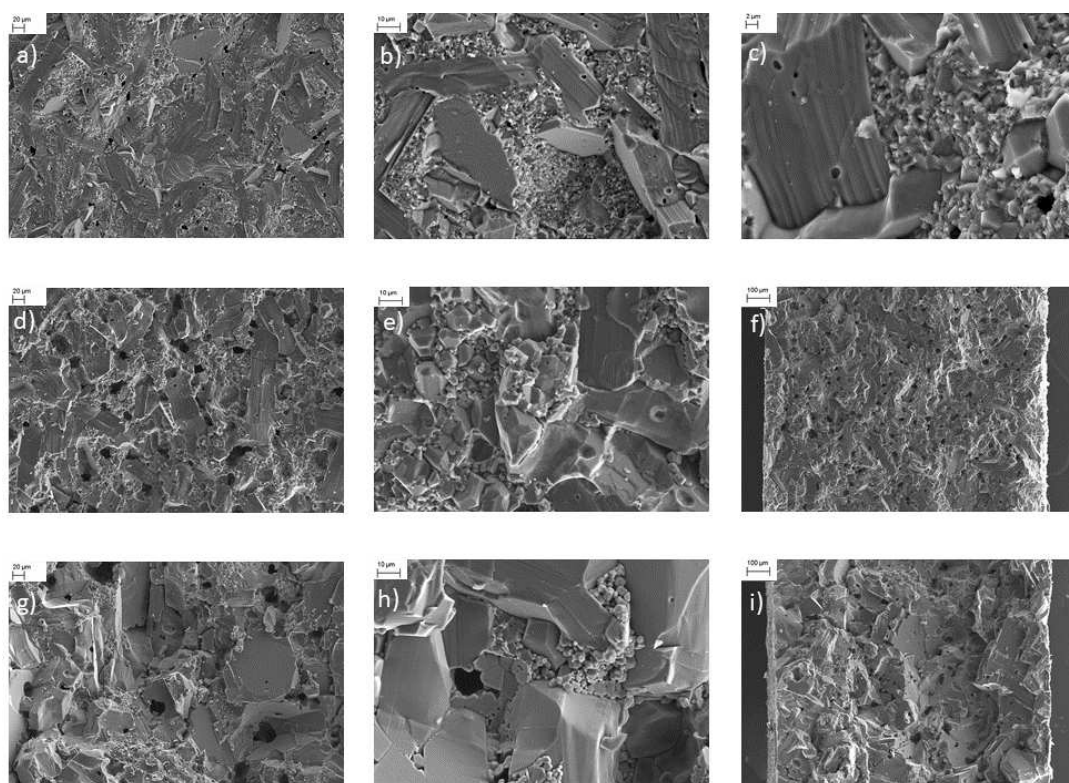
Figure 75. SEM images of Na-β″-alumina doped with a mass fraction of 1.5 % TiO₂ a)-c) sintered at 1500 °C; d)-f) sintered at 1600 °C; g)-i) sintered at 1700 °C.
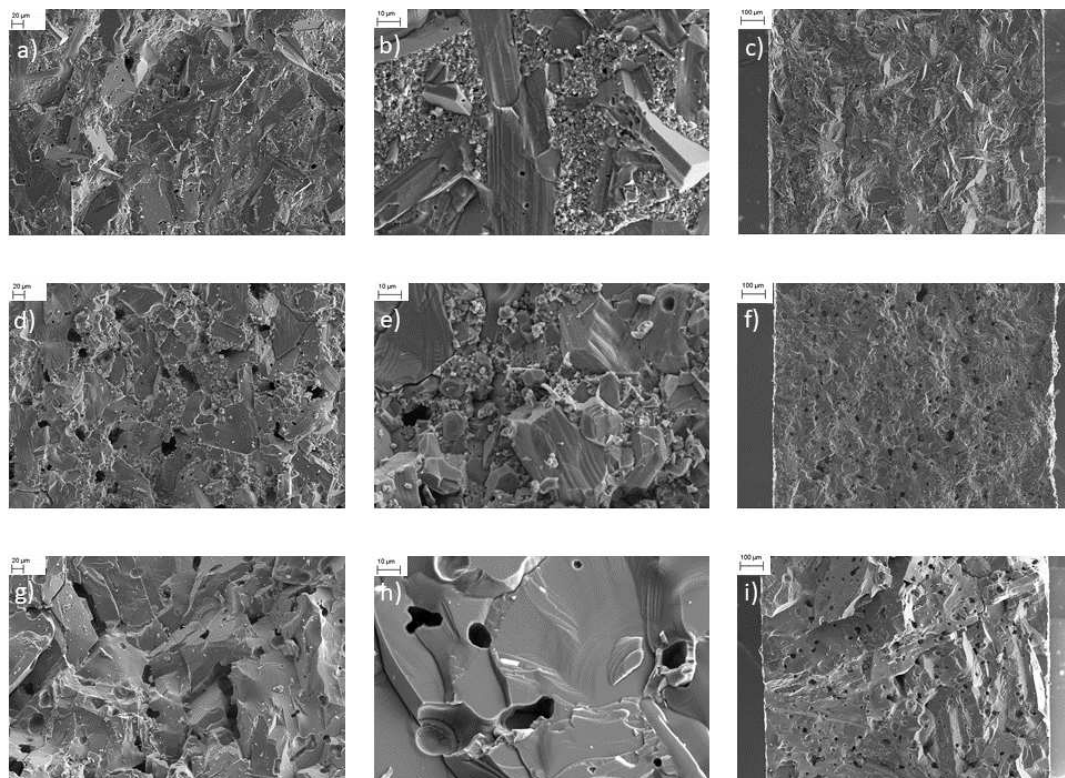
Figure 76. SEM images of Na-β″-alumina doped with a mass fraction of 2.0 % TiO₂ a)-c) sintered at 1500 °C; d)-f) sintered at 1600 °C; g)-i) sintered at 1700 °C.
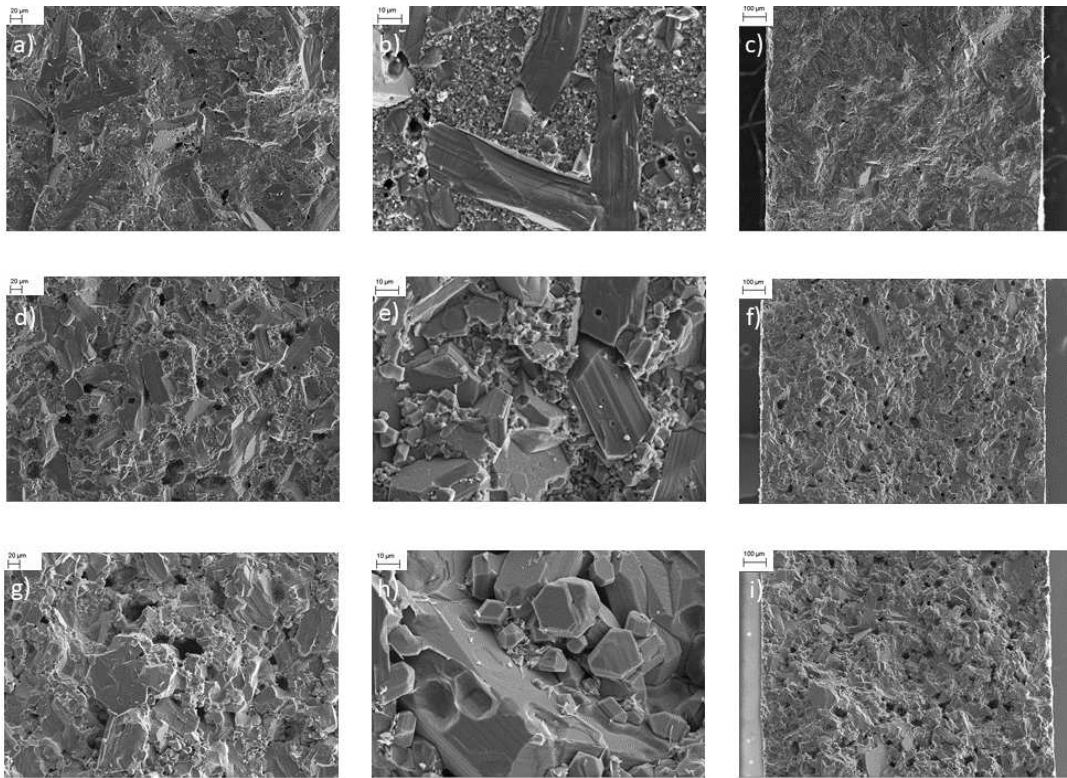
Figure 77. SEM images of Na-β″-alumina doped with a mass fraction of 2.5 % TiO$_2$ a)-c) sintered at 1500 °C; d)-f) sintered at 1600 °C; g)-i) sintered at 1700 °C.
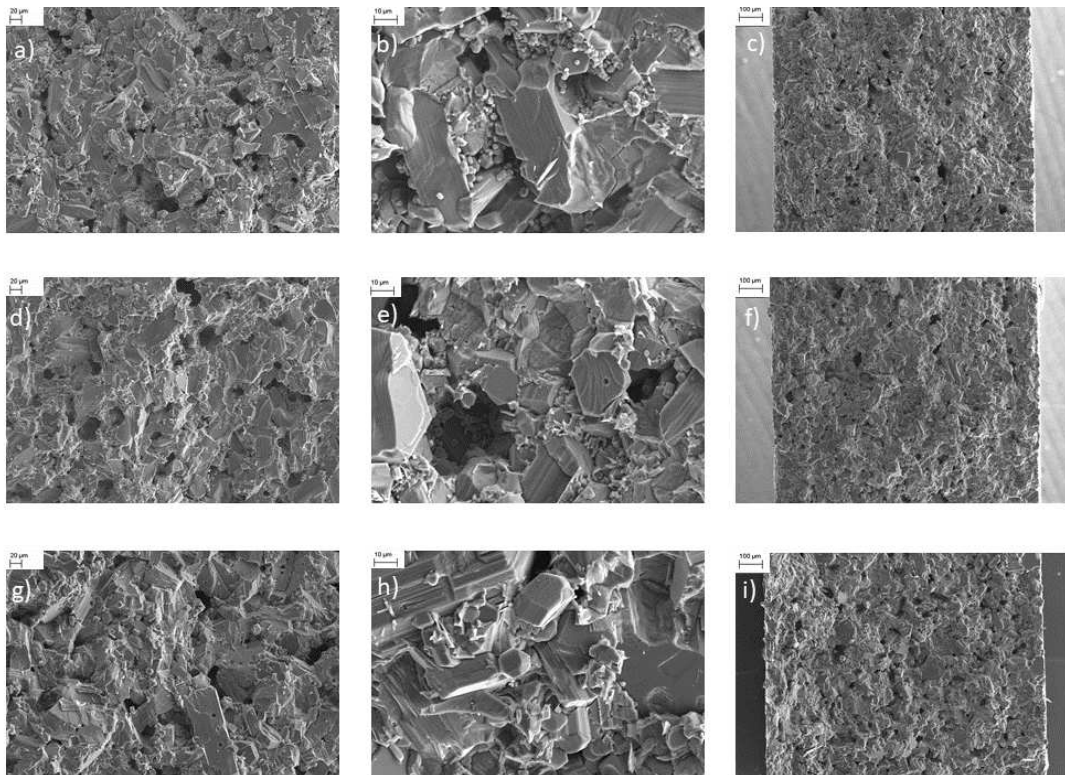
Figure 78. SEM images of Na-β″-alumina doped with a mass fraction of 5.0 % TiO$_2$ a)-c) sintered at 1500 °C; d)-f) sintered at 1600 °C; g)-i) sintered at 1700 °C.
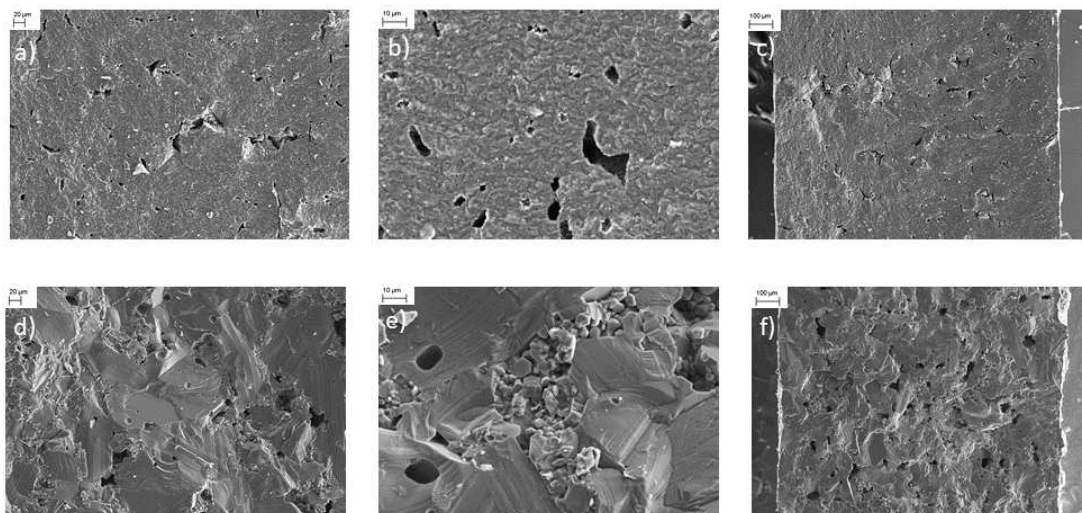
Figure 79. SEM images of Na-β''-alumina doped with a mass fraction of 0.5 % Mn_3O_4 a)-c) sintered at 1600 °C; d)-f) sintered at 1700 °C.
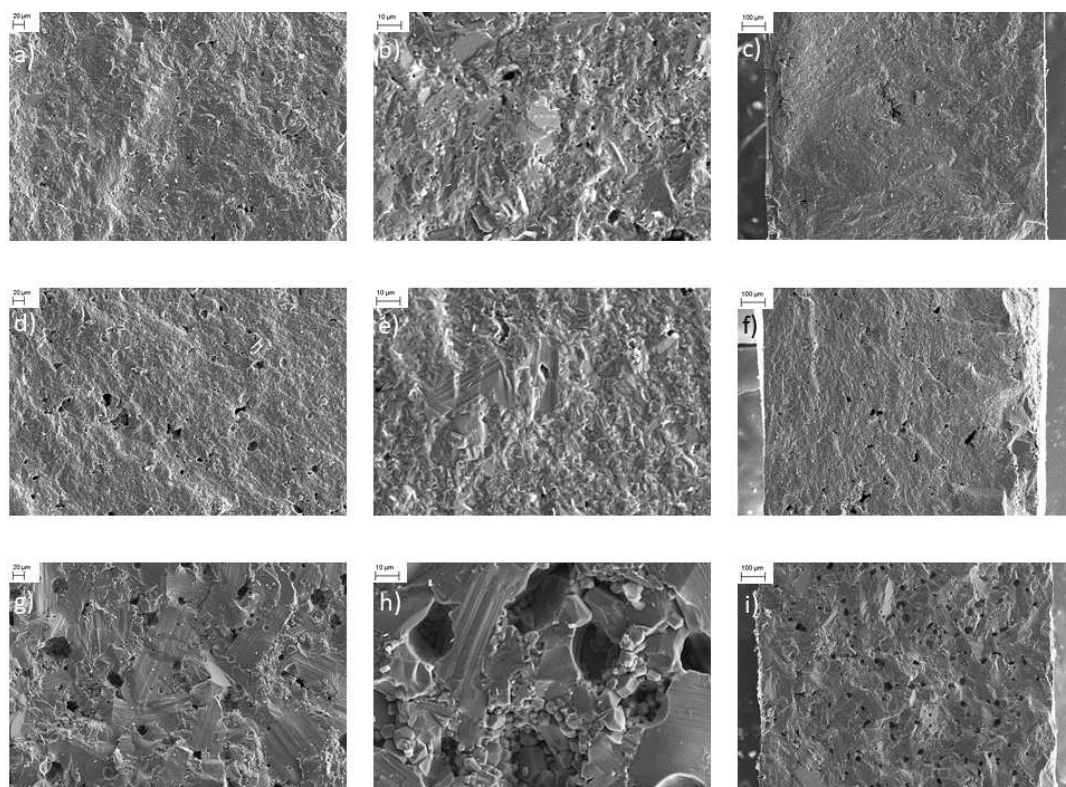
Figure 80. SEM images of Na-β''-alumina doped with a mass fraction of 1.0 % Mn_3O_4 a)-c) sintered at 1500 °C; d)-f) sintered at 1600 °C; g)-i) sintered at 1700 °C.
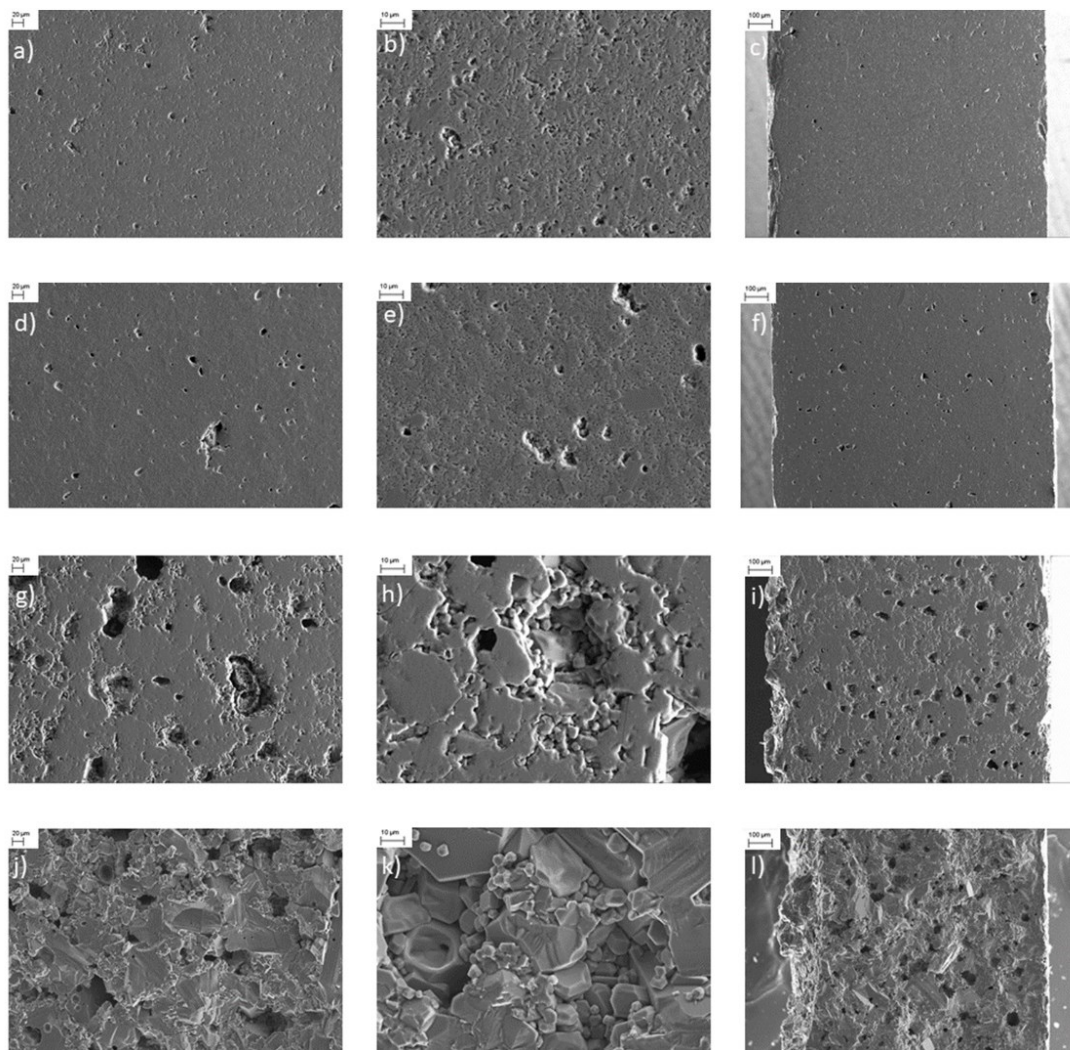
Figure 81. SEM images of Na-β″-alumina doped with a mass fraction of 1.5 % Mn$_3$O$_4$ a)-c) sintered at 1500 °C, polished and thermally etched; d)-f) sintered at 1600 °C polished and thermally etched; g)-i) sintered at 1700 °C, polished and thermally etched; j)-l) sintered at 1700 °C.
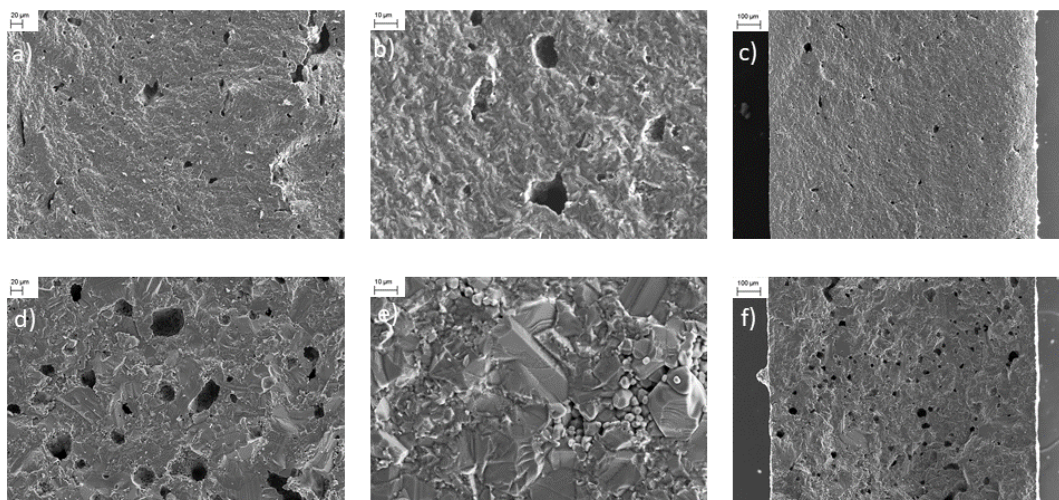
Figure 82. SEM images of Na-β″-alumina doped with a mass fraction of 2.0 % Mn$_3$O$_4$ a)-c) sintered at 1600 °C; d)-f) sintered at 1700 °C.
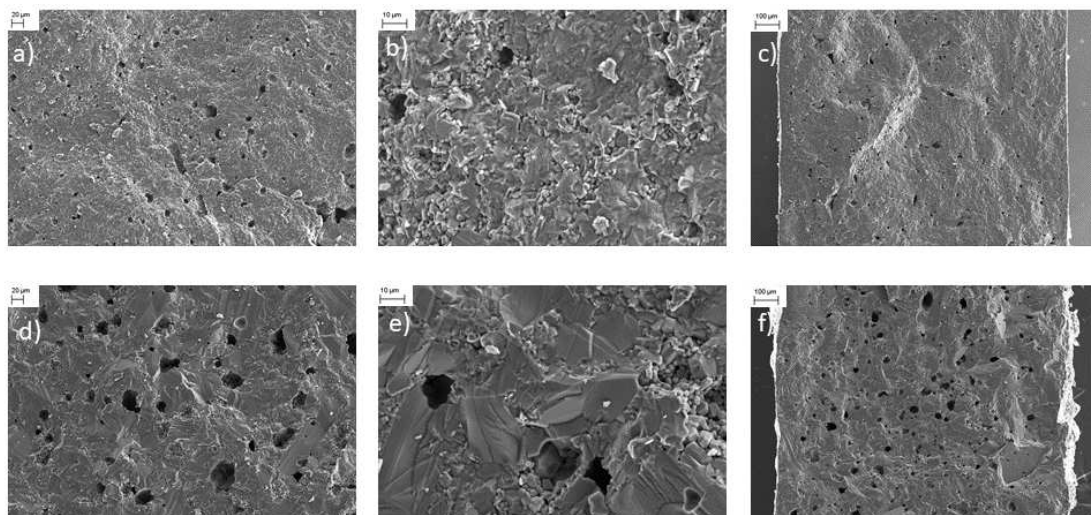
Figure 83. SEM images of Na-β″-alumina doped with a mass fraction of 2.5 % Mn$_3$O$_4$ a)-c) sintered at 1600 °C; d)-f) sintered at 1700 °C.
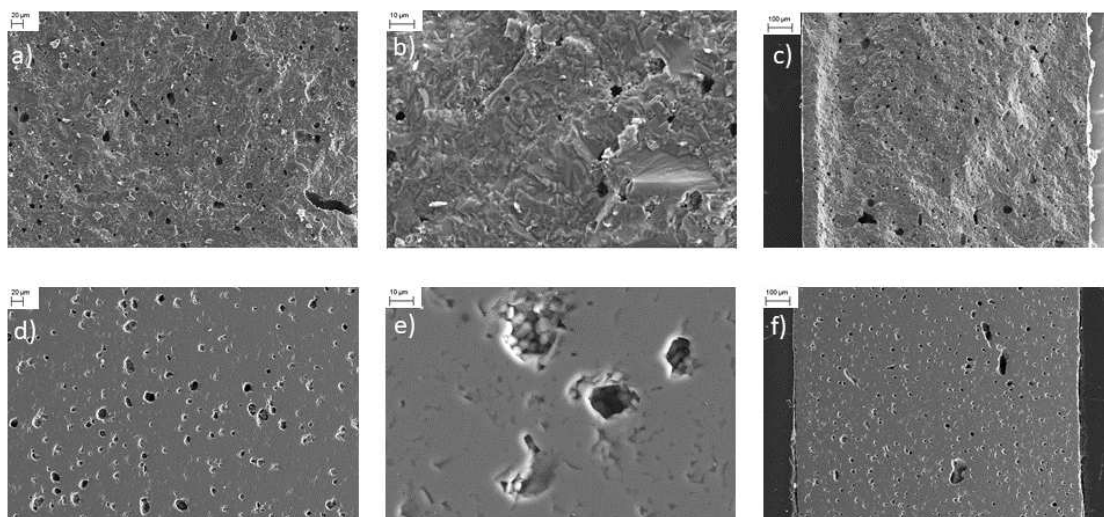
Figure 84. SEM images of Na-β″-alumina doped with a mass fraction of 5.0 % Mn$_3$O$_4$ a)-c) sintered at 1600 °C; d)-f) sintered at 1600 °C polished and thermally etched.
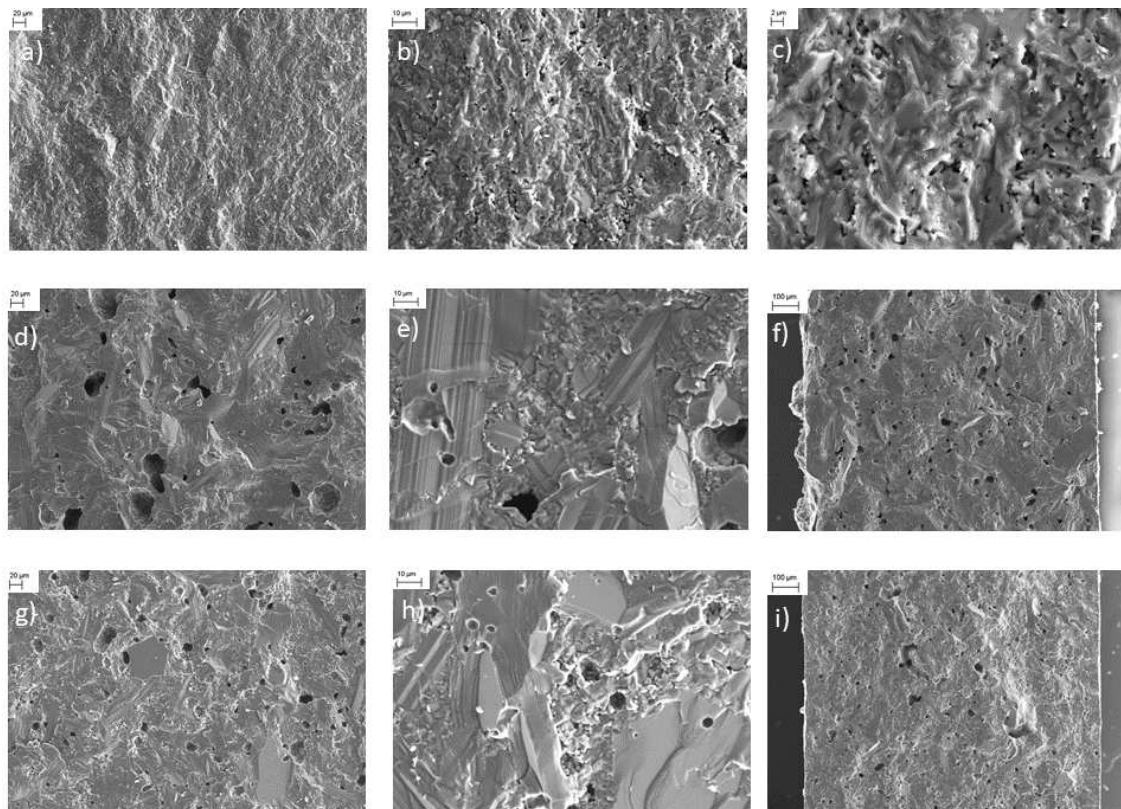
Figure 85. SEM images of Na-β″-alumina doped with a mass fraction of 0.5 % NiO a)-c) sintered at 1500 °C, d)-f) sintered at 1600 °C g)-i) sintered at 1700 °C.
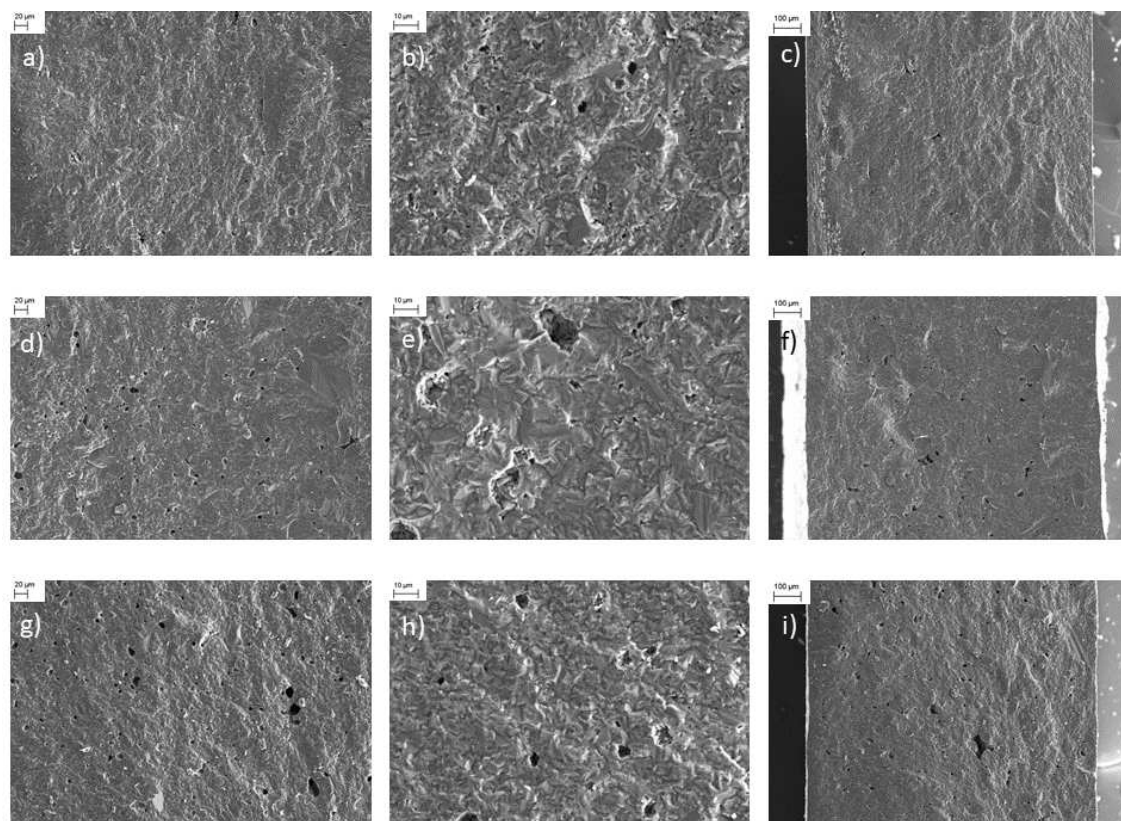
Figure 86. SEM images of Na-β″-alumina doped with a mass fraction of 1.0 % NiO a)-c) sintered at 1500 °C, d)-f) sintered at 1600 °C g)-i) sintered at 1700 °C.
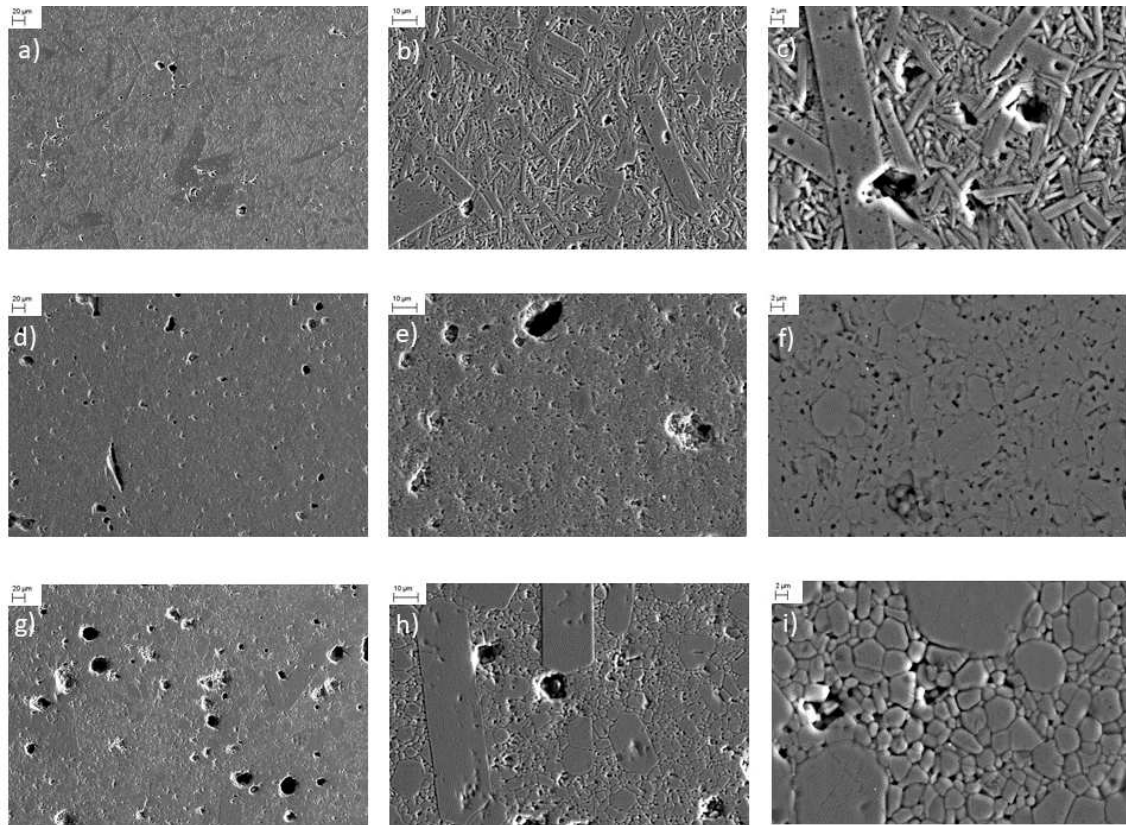
Figure 87. SEM images of Na-β″-alumina doped with a mass fraction of 1.5 % NiO a)-c) sintered at 1500 °C, polished and thermally etched; d)-f) sintered at 1600 °C polished and thermally etched; g)-i) sintered at 1700 °C, polished and thermally etched.
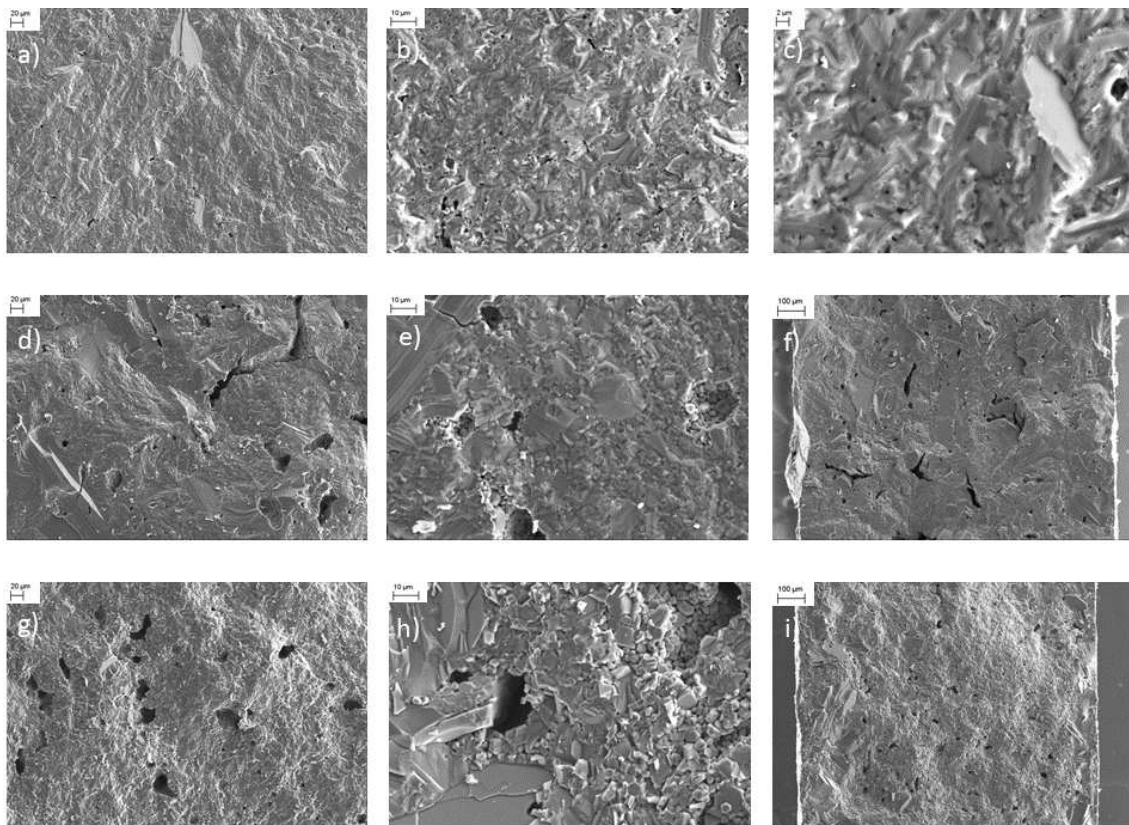
Figure 88. SEM images of Na-β″-alumina doped with a mass fraction of 2.0 % NiO a)-c) sintered at 1500 °C, d)-f) sintered at 1600 °C g)-i) sintered at 1700 °C.
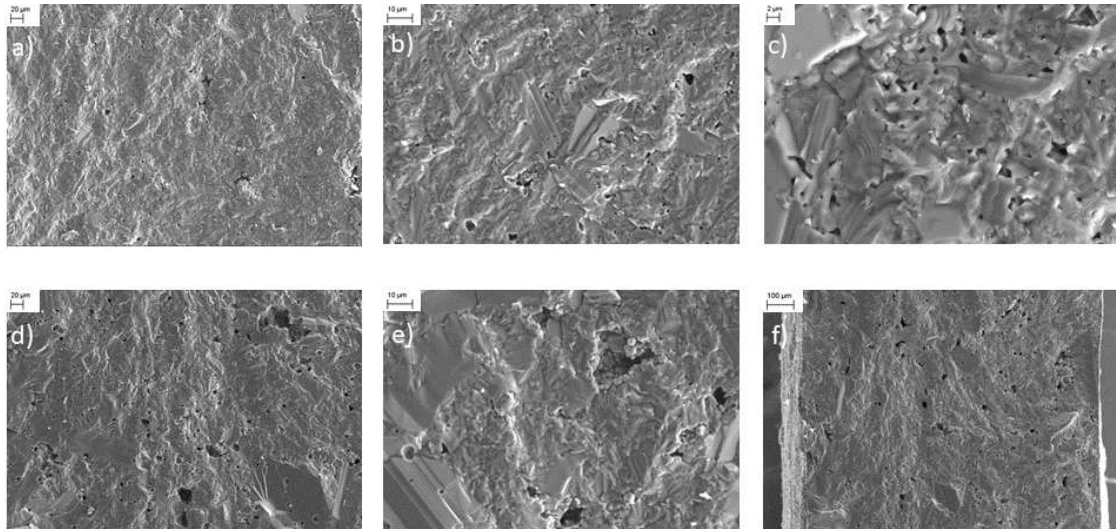
Figure 89. SEM images of Na-β″-alumina doped with a mass fraction of 2.5 % NiO a)-c) sintered at 1500 °C, d)-f) sintered at 1600 °C.
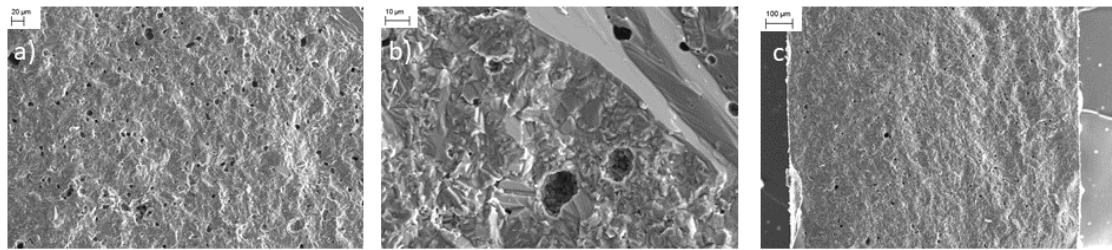
Figure 90. SEM images of Na-β″-alumina doped with a mass fraction of 5.0 % NiO a)-c) sintered at 1600 °C,

Table 8. Characteristic fracture σ_0 and distribution parameter m of TiO_2 doped Na-β″-alumina sintered at different temperatures. Percentages indicate mass fractions. The values are reprinted from *Dirksen et al.* [86]

TiO_2 doping amount / %	σ_0 (Sintered at 1500 °C) / MPa	m	σ_0 (Sintered at 1600 °C) / MPa	m	σ_0 (Sintered at 1700 °C) / MPa	m
0.0	193	13	162	4.2	125	5.5
0.5	259	9.7	192	5.7	130	12
1.0	249	5.1	191	9.3	202	8.4
1.5	175	14	141	12	196	7.1
2.0	164	12	134	17	72.0	3.3
2.5	165	20	137	16	81.6	5.0

Table 9. Characteristic fracture σ_0 and distribution parameter m of Mn_3O_4 doped Na-β″-alumina sintered at different temperatures. Percentages indicate mass fractions. The values for 1600 °C and 1700 °C are reprinted from *Dirksen et al.* [86]

Mn_3O_4 doping amount / %	σ_0 (Sintered at 1500 °C) / MPa	m	σ_0 (Sintered at 1600 °C) / MPa	m	σ_0 (Sintered at 1700 °C) / MPa	m
0.0	193	13	162	4.2	125	5.5
0.5	197	24	174	8.6	110	11
1.0	246	7.5	228	8.8	122	13
1.5	243	12	290	10	120	7.4
2.0	269	14	281	12	103	5.8
2.5	242	11	231	15	93.4	10

Table 10. Characteristic fracture σ_0 and distribution parameter m of NiO doped Na-β″-alumina sintered at different temperatures. Percentages indicate mass fractions. The values for 1600 °C and 1700 °C are reprinted from *Dirksen et al.* [86]

NiO doping amount / %	σ_0 (Sintered at 1500 °C) / MPa	m	σ_0 (Sintered at 1600 °C) / MPa	m	σ_0 (Sintered at 1700 °C) / MPa	m
0.0	193	13	162	4.2	125	5.5
0.5	276	9.4	193	10	158	5.8
1.0	263	8.2	270	4.4	196	6.6
1.5	223	19	296	6.1	258	6.1
2.0	199	6.0	259	7.0	198	18
2.5	235	11	197	4.5	189	6.3

Table 11. R_b, R_{gb} values and the geometric factor (L A^{-1} / cm^{-1}) of undoped and TiO$_2$ doped Na-β″-alumina samples at 300 °C. The resulting ionic conductivities and specific grain boundary resistances are displayed in chapter 4.2.4.

	1500 °C			1600 °C			1700 °C		
	R_b / Ω	R_{gb} / Ω	L A$_{cs}^{-1}$ / cm^{-1}	R_b / Ω	R_{gb} / Ω	L A$_{cs}^{-1}$ / cm^{-1}	R_b / Ω	R_{gb} / Ω	L A$_{cs}^{-1}$ / cm^{-1}
Pristine first sample	50.9	2.4	8.47	41.1	1.7	8.15	23.8	1.0	6.34
Pristine second sample	39.6	3.0	6.39	33.6	2.0	8.18	22.0	0.9	5.73
0.5 % TiO$_2$ first sample	35.4	2.1	7.82	37.4	2.0	8.50	21.5	1.0	6.48
0.5 % TiO$_2$ second sample	34.9	3.2	7.71	33.3	0.8	8.39	21.7	0.9	6.72
1.0 % TiO$_2$ first sample	28.7	1.9	7.13	28.7	2.1	7.98	20.5	0.9	7.17
1.0 % TiO$_2$ second sample	31.1	1.2	8.01	25.6	1.7	7.92	21.5	0.8	6.53
1.5 % TiO$_2$ first sample	24.3	1.7	8.16	25.5	1.4	7.13	30.5	1.4	7.86
1.5 % TiO$_2$ second sample	22.1	1.7	7.09	24.9	2.1	7.69	26.7	1.6	6.29
2.0 % TiO$_2$ first sample	23.7	1.4	6.57	24.6	1.5	7.13	26.7	1.2	6.38
2.0 % TiO$_2$ second sample	24.7	1.8	6.44	23.5	1.4	7.04	23.2	1.0	5.79
2.5 % TiO$_2$ first sample	26.4	1.6	6.10	21.9	1.3	6.23	29.4	1.4	6.70
2.5 % TiO$_2$ second sample	25.9	0.9	6.86	23.6	1.6	6.68	27.5	1.4	6.71

Table 12. R_b, R_{gb} values and the geometric factor (L A^{-1} / cm^{-1}) of Mn$_3$O$_4$ doped Na-β″-alumina samples at 300 °C. The resulting ionic conductivities and specific grain boundary resistances are displayed in chapter 4.2.4.

	1500 °C			1600 °C			1700 °C		
	R_b / Ω	R_{gb} / Ω	L A$_{cs}^{-1}$ / cm^{-1}	R_b / Ω	R_{gb} / Ω	L A$_{cs}^{-1}$ / cm^{-1}	R_b / Ω	R_{gb} / Ω	L A$_{cs}^{-1}$ / cm^{-1}
0.5 % Mn$_3$O$_4$ first sample	38.5	1.9	6.3	27.7	2.2	6.3	23.4	0.4	6.6
0.5 % Mn$_3$O$_4$ second sample	38.3	1.9	5.9	30.5	1.4	7.0	24.1	1.4	6.6
1.0 % Mn$_3$O$_4$ first sample	38.4	3.0	7.1	27.8	1.7	6.8	22.4	0.5	6.3
1.0 % Mn$_3$O$_4$ second sample	27.1	1.9	5.9	28.9	1.2	7.0	23.4	1.9	6.5
1.5 % Mn$_3$O$_4$ first sample	29.7	1.0	5.6	25.7	2.0	6.7	23.4	1.3	6.7
1.5 % Mn$_3$O$_4$ second sample	30.1	2.0	6.0	28.7	1.5	6.7	24.8	1.0	6.8
2.0 % Mn$_3$O$_4$ first sample	38.1	3.0	6.7	26.1	1.9	6.4	24.7	1.0	6.5
2.0 % Mn$_3$O$_4$ second sample	38.1	1.4	6.9	25.8	1.0	5.7	25.0	0.8	6.6
2.5 % Mn$_3$O$_4$ first sample	38.6	2.3	6.7	28.0	1.7	6.3	24.8	0.5	6.4
2.5 % Mn$_3$O$_4$ second sample	34.7	1.0	6.9	27.4	1.2	6.3	24.2	1.2	6.4

Table 13. R_b, R_{gb} values and the geometric factor (L A^{-1} / cm^{-1}) of NiO doped Na-β''-alumina samples at 300 °C. The resulting ionic conductivities and specific grain boundary resistances are displayed in chapter 4.2.4.

	1500 °C			1600 °C			1700 °C		
	R_b / Ω	R_{gb} / Ω	L A_{cs}^{-1} / cm^{-1}	R_b / Ω	R_{gb} / Ω	L A_{cs}^{-1} / cm^{-1}	R_b / Ω	R_{gb} / Ω	L A_{cs}^{-1} / cm^{-1}
0.5 % NiO first sample	45.2	1.6	9.90	28.9	1.2	6.82	24.1	1.5	6.64
0.5 % NiO second sample	41.6	2.2	9.15	25.9	1.1	5.94	23.4	1.6	6.35
1.0 % NiO first sample	39.8	1.7	8.87	28.1	1.6	6.65	23.8	1.9	6.22
1.0 % NiO second sample	46.4	1.8	10.25	27.6	0.7	6.28	23.4	0.5	6.31
1.5 % NiO first sample	35.8	1.3	7.97	27.3	1.0	6.66	24.3	1.4	6.88
1.5 % NiO second sample	35.2	2.2	8.06	32.5	1.3	6.40	24.0	1.4	6.42
2.0 % NiO first sample	39.1	2.2	10.04	31.5	0.9	7.09	25.9	1.3	6.86
2.0 % NiO second sample	35.4	2.8	9.30	26.7	1.0	6.24	26.1	1.2	6.09
2.5 % NiO first sample	33.7	2.1	7.63	35.8	0.7	7.39	23.4	1.3	6.42
2.5 % NiO second sample	48,6	1.6	9.60	28.0	1.6	6.42	27.1	2.1	6.79
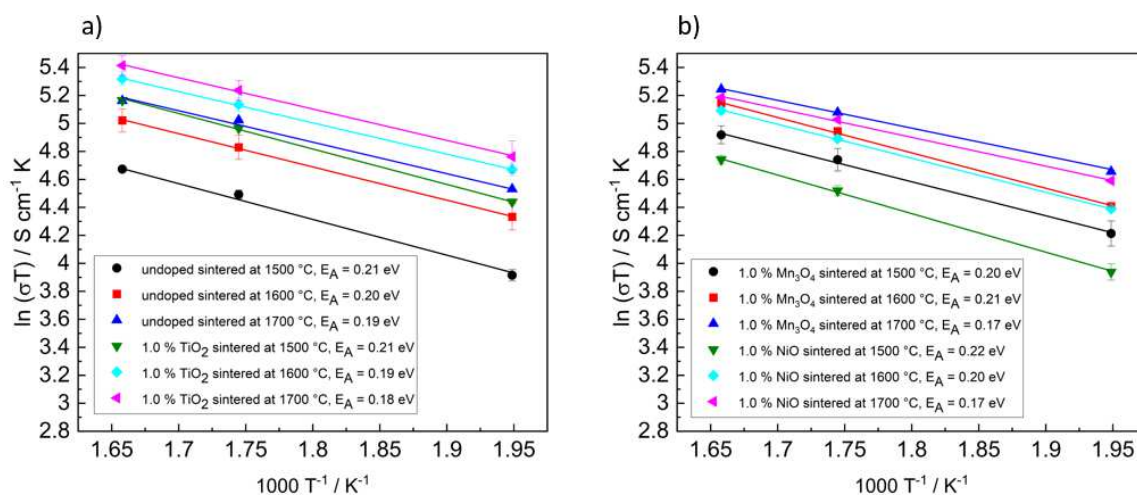
Figure 91. Relationship of the temperature and the ionic conductivity of a) undoped and samples doped with a mass fraction of 1.0 % TiO_2 b) samples doped with a mass fraction of 1.0 % Mn_3O_4 or NiO. The corresponding activation energies were calculated with equation (14).
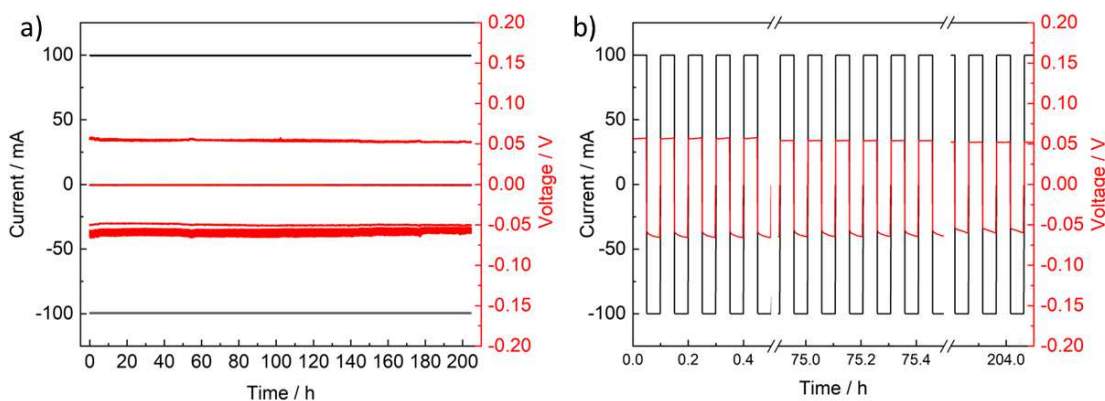
Figure 92. Longer term measurement of an Na|TiO_2 doped Na-β″-alumina|Na cell. A current of 100 mA was applied in each direction for 3 min. The experiment was repeated about 2000 times. a) All data points b) Selection of data points for better visibility.

124
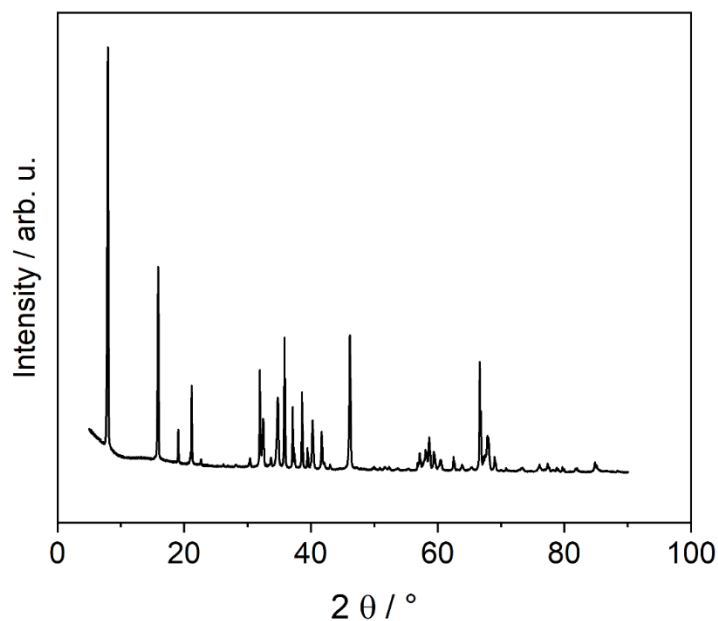
Figure 93. XRD pattern of Na-β″-alumina electrolyte doped with TiO_2 after using it in a Na/$NiCl_2$-cell.
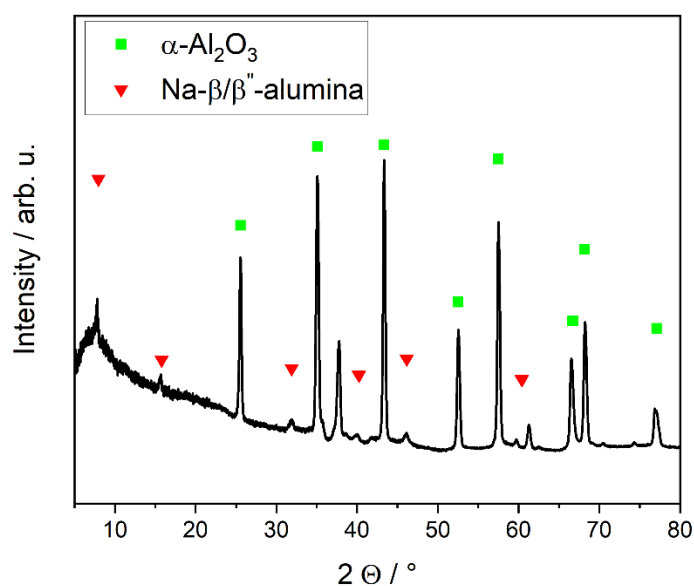
Figure 94. XRD pattern of a porous bulk sintered at 1400 °C. The data are reprinted with permission from *Hoppe, Dirksen, et al.* [143]

8.2 Degradation of Na/$NiCl_2$-cells

For a deeper evaluation of possible cell degradation effects, the voltage profiles of the charge/discharge cycles were also recorded. The profile of the second, the 50[th,] and the 100th cycle (each charged/discharged with 10 mA/0.125 C) are shown in Figure 95. The second cycle showed a nearly stable voltage for the complete charging process, but the end-of-charge voltage (for 100 % SoC) increased to over 2.7 V at the 50th and over 2.8 V at the 100th cycle. The end-of-discharge voltage also dropped slightly with increasing cycle

number. This indicates increasing internal cell resistance and aging. Since the cathode material is well established at Fraunhofer IKTS and has proven stable performance, the observed aging cannot be attributed to the cathode material.
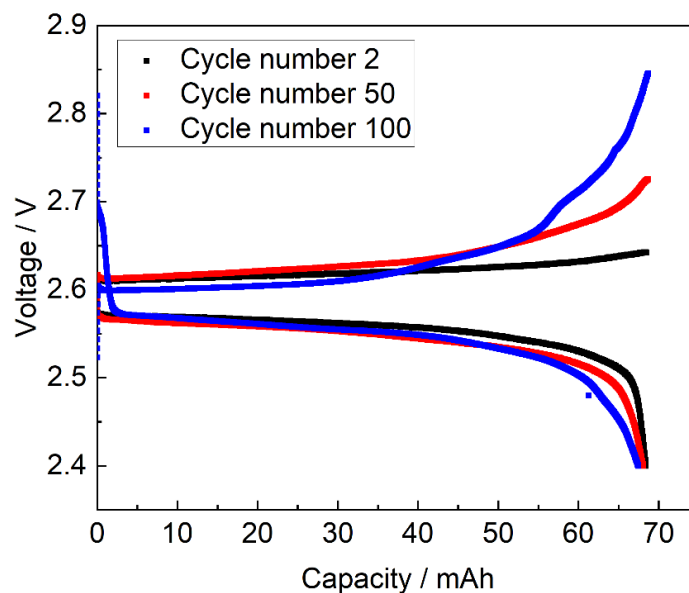
Figure 95. Galvanostatic (10 mA / 0.125 C) voltage profile of a Na/NiCl$_2$-cell with a TiO$_2$ doped Na-β″-alumina electrolyte during 2nd, 50th, and 100th cycle.

A subsequent post-mortem analysis of the cell gave another explanation. Figure 96 a) to d) shows the different cell components after disassembly. The pictures reveal that the PTFE-sealing was discolored (Figure 96 b), and the whole of the fluted seal was covered in NaAlCl$_4$ (Figure 96 b) and c). It seems likely that a loss of NaAlCl$_4$ cause a steady increase of the load resistance. An insufficient amount of NaAlCl$_4$ reduces mass transportation between the granules of the active material and degrades the connection between cathode and current collector.

In contrast, the anode seemed intact as the unchanged C-sealing, and the metallic gloss in Figure 96 d) indicates. There are two general ways of fixing the problem of the PTFE-sealing in future experiments. One way is to reduce the cell operating temperature. The current operating temperature of 300 °C softens the PTFE and this softening reduces its ability to act as a seal. The other way is to use a different kind of seal. A direct substitute for PTFE has not yet been found because most polymers are corroded by the high temperature and the presence of NaAlCl$_4$. The metal seals tested were also unsuccessful. They are resistant to corrosion but the pressure applied by the cell housing was insufficient to cut into the metal and therefore did not make a suitable seal. It might be necessary therefore, to solve the sealing problem, to adopt a more complex solution. A suitable

method is to solder the Al_2O_3-ring directly to the metal housing. The soldering procedures to seal a $Na/NiCl_2$ cell are known [163–166] but require complex machinery. Such machinery was unavailable so I was unable to test this soldering solution.

Figure 96. Post-mortem images of a $Na/NiCl_2$-cell with a TiO_2 doped Na-β″-alumina electrolyte. a) Cathode-side of the electrolyte b) Teflon-sealing of the cathode side c) metal inlay of the cathode side d) anode side of the electrolyte.

9. List of Figures

10.   List of Tables

11.   References

1.   Liu, B.; Lund, J.R.; Liao, S.; Jin, X.; Liu, L.; Cheng, C. Optimal power peak shaving using hydropower to complement wind and solar power uncertainty. *Energy Conversion and Management* **2020**, *209*, 112628, doi:10.1016/j.enconman.2020.112628.

2.   Sovacool, B.K. The intermittency of wind, solar, and renewable electricity generators: Technical barrier or rhetorical excuse? *Utilities Policy* **2009**, *17*, 288–296, doi:10.1016/j.jup.2008.07.001.

3.   Ren, G.; Liu, J.; Wan, J.; Guo, Y.; Yu, D. Overview of wind power intermittency: Impacts, measurements, and mitigation solutions. *(1) Green Energy; Special Section from papers presented at the 2nd International Energy Conf* **2017**, *204*, 47–65, doi:10.1016/j.apenergy.2017.06.098.

4.   Martins, R.; Hesse, H.; Jungbauer, J.; Vorbuchner, T.; Musilek, P. Optimal Component Sizing for Peak Shaving in Battery Energy Storage System for Industrial Applications. *Energies* **2018**, *11*, 2048, doi:10.3390/en11082048.

5.   Pimm, A.J.; Cockerill, T.T.; Taylor, P.G. The potential for peak shaving on low voltage distribution networks using electricity storage. *Journal of Energy Storage* **2018**, *16*, 231–242, doi:10.1016/j.est.2018.02.002.

6.   Shi, Y.; Xu, B.; Di Wang; Zhang, B. Using Battery Storage for Peak Shaving and Frequency Regulation: Joint Optimization for Superlinear Gains. *IEEE Trans. Power Syst.* **2018**, *33*, 2882–2894, doi:10.1109/TPWRS.2017.2749512.

7.   Spoerke, E.D.; Gross, M.M.; Small, L.J.; Percival Stephen J. *U.S. DOE Energy Storage Handbook*: *CHAPTER 4. Sodium-based battery technologies;* U.S. Department of Energy: Washington D.C., 2020.

8.   Benato, R.; Cosciani, N.; Crugnola, G.; Dambone Sessa, S.; Lodi, G.; Parmeggiani, C.; Todeschini, M. Sodium nickel chloride battery technology for large-scale stationary storage in the high voltage network. *J. Power Sources* **2015**, *293*, 127–136, doi:10.1016/j.jpowsour.2015.05.037.

9.   Soloveichik, G.L. Battery Technologies for Large-Scale Stationary Energy Storage. *Annu. Rev. Chem. Biomol. Eng.* **2011**, *2*, 503–527, doi:10.1146/annurev-chembioeng-061010-114116.

10.   Rankin, G.A.; Merwin, H.E. The ternary system CaO-Al2O3-MgO. *J. Am. Chem. Soc* **1916**, *38*, 568–588, doi:10.1021/ja02260a006.

11.   Kummer, J.T.; Weber, N. *A Sodium-Sulfur Secondary Battery;* SAE International: Warrendale, PA, 1967.

12.   Dustmann, C.-H. Advances in ZEBRA batteries. *Journal of Power Sources* **2004**, *127*, 85–92, doi:10.1016/j.jpowsour.2003.09.039.

13.   Ormrod, S.E.; Kirk, D.L. The conduction properties of polycrystalline β"-alumina. *J. Phys. D: Appl. Phys.* **1977**, *10*, 1769–1780, doi:10.1088/0022-3727/10/13/012.

14.   Tan, S.R.; May, G.J. The dependence of the fracture stress of beta-alumina on microstructural defects. *J Mater Sci* **1977**, *12*, 1058–1061, doi:10.1007/BF00540994.

15.   Baukal, W.; Knödler, R.; Kuhn, W. Überblick über die Anwendungsmöglichkeiten von Festelektrolyten. *Chemie Ingenieur Technik* **1978**, *50*, 245–249, doi:10.1002/cite.330500402.

16. May, G.J.; Hooper, A. The effect of microstructure and phase composition on the ionic conductivity of magnesium-doped sodium-beta-alumina. *J Mater Sci* **1978**, *13*, 1480–1486, doi:10.1007/BF00553202.

17. McDonough, W.J.; Flinn, D.R.; Stern, K.H.; Rice, R.W. Hot pressing and physical properties of Na beta alumina. *J Mater Sci* **1978**, *13*, 2403–2412, doi:10.1007/BF00808055.

18. Rivier, M.; Pelton, A.D. A new slip-casting technique for the laboratory fabrication of beta alumina and other ceramics. *Ceramic Bulletin* **1978**, *57*, 183–185.

19. Bovin, J.-O.; O'Keeffe, M. The formation and structure of atomic scale cracks in β-alumina ceramics. *Naturwissenschaften* **1979**, *66*, 576–578, doi:10.1007/BF00368818.

20. Takikawa, O.; Imai, A.; Harata, M. Characteristics of the Na/beta-alumina/Na cell as a sodium vapor pressure sensor. *Solid State Ionics* **1982**, *7*, 101–107, doi:10.1016/0167-2738(82)90002-9.

21. Hodge, J.D. Kinetics of the β″-to-β Transformation in the System Na2O-A12O3. *Journal of the American Ceramic Society* **1983**, *66*, 166–169, doi:10.1111/j.1151-2916.1983.tb10009.x.

22. Stevens, R.; Binner, J.G. Structure, properties and production of β-alumina. *J Mater Sci* **1984**, *19*, 695–715.

23. Fukui, K.; Suzuki, Y. Reactive sintering and particle morphology control of β″-alumina-based water purification filters. *Journal of Materials Science* **2018**, *53*, 1005–1013, doi:10.1007/s10853-017-1599-z.

24. Williams, R.M. The thermal stability of sodium b"-alumina solid electrolyte ceramic in AMTEC cells. *space technology and applications forum 1999* **1999**.

25. Heinz, M.V.; Graeber, G.; Landmann, D.; Battaglia, C. Pressure management and cell design in solid-electrolyte batteries, at the example of a sodium-nickel chloride battery. *Journal of Power Sources* **2020**, 228268, doi:10.1016/j.jpowsour.2020.228268.

26. Ghadbeigi, L.; Szendrei, A.; Moreno, P.; Sparks, T.D.; Virkar, A.V. Synthesis of iron-doped Na-β″-alumina + yttria-stabilized zirconia composite electrolytes by a vapor phase process. *Solid State Ionics* **2016**, *290*, 77–82, doi:10.1016/j.ssi.2016.04.006.

27. Yang, L.-P.; Shan, S.; Wei, X.; Liu, X.; Yang, H.; Shen, X. The mechanical and electrical properties of ZrO2–TiO2–Na-β/β″-alumina composite electrolyte synthesized via a citrate sol–gel method. *Ceramics International* **2014**, *40*, 9055–9060, doi:10.1016/j.ceramint.2014.01.118.

28. Wei, X.; Cao, Y.; Lu, L.; Yang, H.; Shen, X. Synthesis and characterization of titanium doped sodium beta″-alumina. *Journal of Alloys and Compounds* **2011**, *509*, 6222–6226.

29. Bettman, M.; Terner, L.L. Structure of sodium oxide-4 magnesium oxide-15 aluminum oxide, a variant of .beta.-alumina. *Inorg. Chem.* **1971**, *10*, 1442–1446, doi:10.1021/ic50101a025.

30. Wang, Y.; Zhou, D.; Palomares, V.; Shanmukaraj, D.; Sun, B.; Tang, X.; Wang, C.; Armand, M.; Rojo, T.; Wang, G. Revitalising sodium–sulfur batteries for non-high-temperature operation: a crucial review. *Energy Environ. Sci* **2020**, *13*, 3848–3879, doi:10.1039/d0ee02203a.

31. Hueso, K.B.; Armand, M.; Rojo, T. High temperature sodium batteries: status, challenges and future trends. *Energy Environ. Sci.* **2013**, *6*, 734–749, doi:10.1039/c3ee24086j.

32. Hou, W.; Guo, X.; Shen, X.; Amine, K.; Yu, H.; Lu, J. Solid electrolytes and interfaces in all-solid-state sodium batteries: Progress and perspective. *Nano Energy* **2018**, *52*, 279–291, doi:10.1016/j.nanoen.2018.07.036.

33. Bay, M.-C.; Heinz, M.V.; Danilewsky, A.N.; Battaglia, C.; Vogt, U.F. Analysis of c-lattice parameters to evaluate Na2O loss from and Na2O content in β"-alumina ceramics. *Ceramics International* **2021**, *47*, 13402–13408, doi:10.1016/j.ceramint.2021.01.197.

34. Hodge, J.D. Phase Relations in the System Na2O-Li2O-Al2O3. *J American Ceramic Society* **1984**, *67*, 183–185, doi:10.1111/j.1151-2916.1984.tb19738.x.

35. Zhu, C.; Xue, J.; Ji, G. Effect of Na2O content on properties of beta alumina solid electrolytes. *Materials Science in Semiconductor Processing* **2015**, *31*, 487–492, doi:10.1016/j.mssp.2014.12.038.

36. Baffier, N.; Badot, J.C.; Colomban, P. Conductivity of ion rich β and β″ alumina: Sodium and potassium compounds. *Materials Research Bulletin* **1981**, *16*, 259–265, doi:10.1016/0025-5408(81)90040-4.

37. Sudworth, J.L.; Tilley, A.R. *The sodium sulfur battery;* Chapman and Hall: London, 1985, ISBN 0-412-16490-6.

38. Briant, J.L.; Farrington, G.C. Ionic conductivity in Na+, K+, and Ag+ β″-alumina. *Journal of Solid State Chemistry* **1980**, *33*, 385–390, doi:10.1016/0022-4596(80)90161-9.

39. Engstrom, H.; Bates, J.; Brundage, W.; Wang, J.C. Ionic conductivity of sodium beta″-alumina. *Solid State Ionics* **1981**, *2*, 265–276, doi:10.1016/0167-2738(81)90027-8.

40. Underweiser, O.; Dunn, A. Electrical transport of mixed (Na+,Ba2+) beta "-alumina. *Phys. Rev. B* **1991**, *43*, 11999–12003, doi:10.1103/physrevb.43.11999.

41. Agustina, A.I.; Skadell, K.; Dirksen, C.L.; Schulz, M.; Kusumocahyo, S.P. Sol-gel method for synthesis of Li+-stabilized Na-β"-alumina for solid electrolytes in sodium-based batteries **2019**, 20070, doi:10.1063/1.5134634.

42. Park, H.; Jung, K.; Nezafati, M.; Kim, C.-S.; Kang, B. Sodium Ion Diffusion in Nasicon (Na3Zr2Si2PO12) Solid Electrolytes: Effects of Excess Sodium. *ACS Appl. Mater. Interfaces* **2016**, *8*, 27814–27824, doi:10.1021/acsami.6b09992.

43. Chen, S.; Wu, C.; Shen, L.; Zhu, C.; Huang, Y.; Xi, K.; Maier, J.; Yu, Y. Challenges and Perspectives for NASICON-Type Electrode Materials for Advanced Sodium-Ion Batteries. *Adv. Mater.* **2017**, *29*, doi:10.1002/adma.201700431.

44. Fabry, P.; Gros, J.P.; Million-Brodaz, J.F.; Kleitz, M. Nasicon, an ionic conductor for solid-state Na+-selective electrode. *Sensors and Actuators* **1988**, *15*, 33–49, doi:10.1016/0250-6874(88)85016-9.

45. Hartmann, P.; Leichtweiss, T.; Busche, M.R.; Schneider, M.; Reich, M.; Sann, J.; Adelhelm, P.; Janek, J. Degradation of NASICON-Type Materials in Contact with Lithium Metal: Formation of Mixed Conducting Interphases (MCI) on Solid Electrolytes. *J. Phys. Chem. C* **2013**, *117*, 21064–21074, doi:10.1021/jp4051275.

46. Kim, J.; Jo, S.H.; Kim, J.-S.; BHAVARAJU, S.; Kang, S.O. Investigation of manufacturing parameters for NaCl–Ni granule type cathodes used in low temperature NaSICON sodium-metal chloride batteries. *Journal of Alloys and Compounds* **2016**, *665*, 288–293, doi:10.1016/j.jallcom.2016.01.001.

47. Kim, J.; Jo, S.H.; Bhavaraju, S.; Eccelstone, A.; Kang, S.O. Low temperature performance of sodium–nickel chloride batteries with NaSICON solid electrolyte.

Journal of Electroanalytical Chemistry **2015**, *759*, 201–206, doi:10.1016/j.jelechem.2015.11.022.

48. Shannon, R.D.; Taylor, B.E.; Gier, T.E.; Chen, H.Y.; Berzins, T. Ionic conductivity in sodium yttrium silicon oxide (Na5YSi4O12)-type silicates. *Inorg. Chem.* **1978**, *17*, 958–964, doi:10.1021/ic50182a033.

49. Fergus, J.W. Ion transport in sodium ion conducting solid electrolytes. *Solid State Ionics* **2012**, *227*, 102–112, doi:10.1016/j.ssi.2012.09.019.

50. Nakayama, S.; Watanabe, T.; Asahi, T.; Kiyono, H.; Aung, Y.L.; Sakamoto, M. Influence of rare earth additives and boron component on electrical conductivity of sodium rare earth borate glasses. *Ceramics International* **2010**, *36*, 2323–2327, doi:10.1016/j.ceramint.2010.07.026.

51. Sudworth, J.L. Zebra batteries. *J. Power Sources* **1994**, *51*, 105–114, doi:10.1016/0378-7753(94)01967-3.

52. Sudworth, J. The sodium/nickel chloride (ZEBRA) battery. *Journal of Power Sources* **2001**, *100*, 149–163, doi:10.1016/S0378-7753(01)00891-6.

53. Nikiforidis, G.; van de Sanden, M.C.M.; Tsampas, M.N. High and intermediate temperature sodium–sulfur batteries for energy storage: development, challenges and perspectives. *RSC Adv.* **2019**, *9*, 5649–5673, doi:10.1039/C8RA08658C.

54. Yang, Z.; Zhang, J.; Kintner-Meyer, M.C.W.; Lu, X.; Choi, D.; Lemmon, J.P. Electrochemical Energy Storage for Green Grid: Status and Challenges. *ECS Meeting Abstracts* **2011**, *1102*, 155.

55. Doughty, D.H.; Butler, P.C.; Akhil, A.A.; Clark, N.H.; Boyes, J.D. Batteries for Large-Scale Stationary Electrical Energy Storage. *Interface* **2010**, *19*, 49–53.

56. F. G. Will. Effect of Water on Beta Alumina Conductivity. *J. Electrochem. Soc* **1976**, *123*, 834–836, doi:10.1149/1.2132943.

57. Flor, G.; Marini, A.; Massarotti, V.; Villa, M. Reactivity of ß-Aluminas with Water. *Solid State Ionics* **1981**, *2*, 195–204, doi:10.1016/0167-2738(81)90179-X.

58. Dunn, B. Effect of Air Exposure on the Resistivity of Sodium Beta and Beta Aluminas. *Journal of the American Ceramic Society* **1981**, *64*, 125–128, doi:10.1111/j.1151-2916.1981.tb10241.x.

59. Ansell, R.O. The Chemical and Electrochemical Stability of Beta-Alumina. *J Mater Sci* **1986**, 365–379.

60. Evstigneeva, M.A.; Nalbandyan, V.B.; Petrenko, A.A.; Medvedev, B.S.; Kataev, A.A. A New Family of Fast Sodium Ion Conductors: Na 2 M 2 TeO 6 (M = Ni, Co, Zn, Mg). *Chem. Mater.* **2011**, *23*, 1174–1181, doi:10.1021/cm102629g.

61. Takeuchi, S.; Suzuki, K.; Hirayama, M.; Kanno, R. Sodium superionic conduction in tetragonal Na3PS4. *Journal of Solid State Chemistry* **2018**, *265*, 353–358, doi:10.1016/j.jssc.2018.06.023.

62. Ma, Q.; Guin, M.; Naqash, S.; Tsai, C.-L.; Tietz, F.; Guillon, O. Scandium-Substituted Na3Zr2 (SiO4)2(PO4) Prepared by a Solution-Assisted Solid-State Reaction Method as Sodium-Ion Conductors. *Chem. Mater.* **2016**, *28*, 4821–4828, doi:10.1021/acs.chemmater.6b02059.

63. Guin, M.; Tietz, F.; Guillon, O. New promising NASICON material as solid electrolyte for sodium-ion batteries: Correlation between composition, crystal structure and ionic conductivity of Na3+xSc2SixP3−xO12. *Proceedings of the International Conference on Fast Ionic Transport in Solids* **2016**, *293*, 18–26, doi:10.1016/j.ssi.2016.06.005.

64. Dirksen, C.L.; Skadell, K.; Schulz, M.; Stelter, M. Effects of TiO2 doping on Li+-stabilized Na-β″-alumina for energy storage applications. *Separation and Purification Technology* **2019**, *213*, 88–92, doi:10.1016/j.seppur.2018.12.028.

65. Fertig, M.P.; Skadell, K.; Schulz, M.; Dirksen, C.; Adelhelm, P.; Stelter, M. From High- to Low-Temperature: The Revival of Sodium-Beta Alumina for Sodium Solid-State Batteries. *Batteries & Supercaps* **2022**, doi:10.1002/batt.202100131.

66. Yamaguchi, S.; Terabe, K.; Iguchi, Y.; Imai, A. Formation and crystallization of beta-alumina from precursor prepared by sol-gel method using metal alkoxides. *Solid State Ionics* **1987**, *25*, 171–176, doi:10.1016/0167-2738(87)90117-2.

67. Sartori, S.; Martucci, A.; Muffato, A.; Guglielmi, M. Sol-gel synthesis of Na$^+$ beta-Al$_2$O$_3$ powders. *J. Eur. Ceram. Soc.* **2004**, *24*, 911–914, doi:10.1016/S0955-2219(03)00513-2.

68. Jayaraman, V.; Gnanasekaran, T.; Periaswami, G. Low-temperature synthesis of β-aluminas by a sol-gel technique. *Materials Letters* **1997**, *30*, 157–162, doi:10.1016/S0167-577X(96)00193-0.

69. Salmang, H.; Scholze, H.; Telle, R. *Keramik (German Edition);* Springer: Dordrecht, 2007, ISBN 978-3-540-63273-3.

70. Lu, X.; Xia, G.-G.; Lemmon, J.P.; Yang, Z. Advanced materials for sodium-beta alumina batteries: Status, challenges and perspectives. *J. Power Sources* **2010**, *195*, 2431–2442.

71. Li, H.; Fan, H.; Zhang, J.; Wen, Y.; Chen, G.; Zhu, Y.; Lu, J.; Jiang, X.; Hu, B.; Ning, L. Sintering behavior and properties of lithium stabilized sodium β″ - alumina ceramics with YSZ addition. *Ceramics International* **2019**, *45*, 6744–6752, doi:10.1016/j.ceramint.2018.12.165.

72. Kvachkov, R.; Yanakiev, A.; Poulieff, C.N.; Balkanov, I.; Yankulov, P.D.; Budevski, E. Effect of the starting Al2O3 and of the method of preparation on the characteristics of Li-stabilized beta-Al2O3 ceramics. *J Mater Sci* **1981**, *16*, 2710–2716, doi:10.1007/BF00552953.

73. Lu, X.; Lemmon, J.P.; Sprenkle, V.L.; Yang, Z. Sodium-beta alumina batteries: Status and challenges. *JOM Journal of the Minerals, Metals and Materials Society* **2010**, *62*, 31–36, doi:10.1007/s11837-010-0132-5.

74. Byckalo, W.; Rosenblatt, G.; Lam, J.; Nicholson, P.S. Slip casting of beta-Al203 for alkali probes in molten metals. *Ceramic Bulletin* **1976**, *55*, 286–288.

75. Li, N.; Wen, Z.; Liu, Y.; Xu, X.; Lin, J.; Gu, Z. Preparation of Na-beta″-alumina film by tape casting process. *J. Eur. Ceram. Soc.* **2009**, *29*, 3031–3037, doi:10.1016/j.jeurceramsoc.2009.04.019.

76. Ligon, S.C.; Bay, M.-C.; Heinz, M.V.F.; Battaglia, C.; Graule, T.; Blugan, G. Large Planar Na-β″-Al2O3 Solid Electrolytes for Next Generation Na-Batteries. *Materials (Basel)* **2020**, *13*, 433, doi:10.3390/ma13020433.

77. Hofacker, M.; Kiesel, L. Extrusion methods and extrusion device for producing a closed ceramic tube with a base. WO2017DE100183, September 3, 2017.

78. Kennedy, J.H.; Foissy, A. Fabrication of Beta-Alumina Tubes by Electrophoretic Deposition from Suspensions in Dichloromethane. *J. Electrochem. Soc.* **1975**, *122*, 482–486, doi:10.1149/1.2134244.

79. Wei, X.-L.; Xia, Y.; Liu, X.-M.; Yang, H.; Shen, X.-D. Preparation of sodium beta″-alumina electrolyte thin film by electrophoretic deposition using Taguchi experimental design approach. *Electrochim. Acta* **2014**, *136*, 250–256.

80. Harbach, F.; Nienburg, H. Homogeneous functional ceramic components through electrophoretic deposition from stable colloidal suspensions—II. Beta-alumina and concepts for industrial production. *J. Eur. Ceram. Soc.* **1998**, *18*, 685–692, doi:10.1016/S0955-2219(97)00174-X.

81. Parthasarathy, P.; Virkar, A.V. Vapor Phase Conversion of Alumina + Zirconia Composites into Sodium Ion Conducting Na-b "-Alumina + Zirconia Solid Electrolytes. *J. Electrochem. Soc* **2013**, *160*, A2268-A2280, doi:10.1149/2.095311jes.

82. Jung, K.; Chang, H.-J.; Bonnett, J.F.; Canfield, N.L.; Sprenkle, V.L.; Li, G. An advanced Na-NiCl 2 battery using bi-layer (dense/micro-porous) β″-alumina solid-state electrolytes. *Journal of Power Sources* **2018**, *396*, 297–303, doi:10.1016/j.jpowsour.2018.06.039.

83. Vries, R.C.; Roth, W.L. Critical Evaluation of the Literature Data on B Alumina and Related Phases: I, Phase Equilibria and Characterization of B Alumina Phases. *J American Ceramic Society* **1969**, *52*, 364, doi:10.1111/j.1151-2916.1969.tb11956.x.

84. *Ternary alloys*: *A comprehensive compendium of evaluated constitutional data and phase diagrams;* Materials Science International Services; VCH: Weinheim, 1993, ISBN 3527283706.

85. Lu, Y.; Li, L.; Zhang, Q.; Niu, Z.; Chen, J. Electrolyte and Interface Engineering for Solid-State Sodium Batteries. *Joule* **2018**, *2*, 1747–1770, doi:10.1016/j.joule.2018.07.028.

86. Dirksen, C.L.; Skadell, K.; Schulz, M.; Fertig, M.P.; Stelter, M. Influence of 3d Transition Metal Doping on Lithium Stabilized Na-β″-Alumina Solid Electrolytes. *Materials (Basel)* **2021**, *14*, 5389, doi:10.3390/ma14185389.

87. Imai, A.; Harata, M. Ionic Conduction of Impurity-Doped β-Alumina Ceramics. *Japanese Journal of Applied Physics* **1972**, *11*, 180–185, doi:10.1143/jjap.11.180.

88. Youngblood, G.E.; Virkar, A.V.; Cannon, W.R.; Gordon, R.S. Sintering Processes and Heat Treatment Schedules for Conductive, Lithia-Stabilized Beta Double Prime-Al2O3. *American Ceramic Society Bulletin* **1977**, 206–212.

89. Jorgensen, J.D.; Rotella, F.J.; Roth, W.L. Conduction plane and structure of Li-stabilized Na+ β″-alumina: A powder neutron diffraction study. *Proceedings of the International Conference on Fast Ionic Transport in Solids* **1981**, *5*, 143–146, doi:10.1016/0167-2738(81)90212-5.

90. van Zyl, A.; Thackeray, M.M.; Duncan, G.K.; Kingon, A.I.; Heckroodt, R.O. The synthesis of beta alumina from aluminium hydroxide and oxyhydroxide precursors. *Materials Research Bulletin* **1993**, *28*, 145–157, doi:10.1016/0025-5408(93)90083-P.

91. Zhang, C.; Zhang, L.; Zhang, X.; Zheng, P.; Li, F. Synthesis of lithium-doped Na-β″-alumina composite electrolytes by a vapor phase process. *Ceramics International* **2020**, *46*, 3009–3014, doi:10.1016/j.ceramint.2019.09.300.

92. Barison, S.; Fasolin, S.; Mortalò, C.; Boldrini, S.; Fabrizio, M. Effect of precursors on β-alumina electrolyte preparation. *J. Eur. Ceram. Soc.* **2015**, *35*, 2099–2107, doi:10.1016/j.jeurceramsoc.2015.01.006.

93. Thackeray, M.M.; David, W.; Bruce, P.G.; Goodenough, J.B. Lithium insertion into manganese spinels. *Materials Research Bulletin* **1983**, *18*, 461–472, doi:10.1016/0025-5408(83)90138-1.

94. Yasui, I. Effects of Calcium, Potassium, and Iron Ions on Degradation of β″-Alumina. *J. Electrochem. Soc.* **1978**, *125*, 1007, doi:10.1149/1.2131612.

95. Yasui, I.; Hattori, T. Effect of K+ and Ca2+ ions on grain-boundary and bulk conductivity in ß,ß″-alumina. *Solid State Ionics* **1981**, *3–4*, 401–404, doi:10.1016/0167-2738(81)90121-1.

96. Atsuo, I.; Mituo, H. Ionic Conduction of Impurity-Doped beta-Alumina Ceramics. *Japanese Journal of Applied Physics* **1972**, doi:10.1143/JJAP.11.180.

97. Hsieh, M.Y.; Jonghe, L.C. De. Silicate-Containing Sodium Beta-Alumina Solid Electrolytes. *Journal of the American Ceramic Society* **1978**, *61*, 186–191, doi:10.1111/j.1151-2916.1978.tb09275.x.

98. Boilot, J.P.; Théry, J. Influence de l'addition d'ions etrangers sur la stabilite relative et la conductivite electrique des phases de type alumine β et β″. *Materials Research Bulletin* **1976**, *11*, 407–413, doi:10.1016/0025-5408(76)90089-1.

99. Wynne-Lord, J.; L. J., M. Production of β-aluminum oxide electrolyte. *proc. br. ceram. soc* **1971**, 161.

100. Boilot, J.P.; Kahn, A.; Thery, J.; Collongues, R.; Antoine, J.; Vivien, D.; Chevrette, C.; Gourier, D. Influence of foreign ions addition on relative stability and electrical conductivity of β and β″ alumina type phases localization of impurities. *Electrochimica Acta* **1977**, *22*, 741–745, doi:10.1016/0013-4686(77)80029-7.

101. Wasiucionek, M. Electrical properties of CoO, NiO, CuO and ZnO doped beta″-alumina. *Solid State Ionics* **1982**, *7*, 283–286, doi:10.1016/0167-2738(82)90024-8.

102. L. Viswanathan, Y. Ikuma, A. V. Virkar. Transfomation toughening of ß″-alumina by incorporation of zirconia. *J Mater Sci* **1983**, *18*, 109–113, doi:10.1007/BF00543815.

103. Heavens, S.N. Strength improvement in β″ alumina by incorporation of zirconia. *J Mater Sci* **1988**, *23*, 3515–3518, doi:10.1007/BF00540489.

104. Reed, D.; Coffey, G.; Mast, E.; Canfield, N.; Mansurov, J.; Lu, X.; Sprenkle, V.L. Wetting of sodium on β″-Al2O3/YSZ composites for low temperature planar sodium-metal halide batteries. *J. Power Sources* **2013**, *227*, 94–100, doi:10.1016/j.jpowsour.2012.11.034.

105. Li, H.; Fan, H.; Chen, G.; Zhang, J.; Wang, B.; Lu, J.; Jiang, X. Performance of Nano-3YSZ toughened β''-Alumina solid electrolyte prepared by EDTA-Zr(IV)/Y(III) complex as surface modifier. *Journal of Alloys and Compounds* **2020**, *817*, 152717, doi:10.1016/j.jallcom.2019.152717.

106. Lee, D.-H.; Han, S.-S.; Kim, Y.-H.; Lim, S.-K. Analysis of crystal phases of Na+-β/β″-alumina/YSZ composite prepared by vapor-phase synthesis from YSZ-toughened α-alumina. *Journal of Industrial and Engineering Chemistry* **2019**, *76*, 366–373, doi:10.1016/j.jiec.2019.04.002.

107. Ghadbeigi, L.; Sparks, T.D.; Virkar, A.V. Electrochemical Studies on Na-β″-Alumina + Yttria-Stabilized Zirconia (YSZ) Composite Mixed Na + -Ion-O 2− -Ion Conductors. *J. Electrochem. Soc.* **2019**, *166*, F679-F686, doi:10.1149/2.0161912jes.

108. Ligon, S.C.; Blugan, G.; Bay, M.-C.; Battaglia, C.; Heinz, M.V.; Graule, T. Performance analysis of Na-β″-Al2O3/YSZ solid electrolytes produced by conventional sintering and by vapor conversion of α-Al2O3/YSZ. *Proceedings of the International Conference on Fast Ionic Transport in Solids* **2020**, *345*, 115169, doi:10.1016/j.ssi.2019.115169.

109. Sparks, T.D.; Ghadbeigi, L. Anisotropic properties of Na-β″-alumina + YSZ composite synthesized by vapor phase method. *J. Mater. Res.* **2018**, *33*, 81–89, doi:10.1557/jmr.2017.436.

110. Lee, D.-H.; Lee, S.-T.; Kim, J.-S.; Lim, S.-K. Analysis of properties of partially stabilized zirconia-doped Na + -beta-alumina prepared by calcining-cum-sintering process. *Materials Research Bulletin* **2017**, doi:10.1016/j.materresbull.2017.05.003.

111. Zhang, C.; Zhang, L.; Chang, Y. an; Liu, J.H. Preparation of β"-Alumina with η Type Nanometer Alumina Powder via Solid Phase Synthesis. *SSP* **2018**, *281*, 84–89, doi:10.4028/www.scientific.net/SSP.281.84.

112. Adelhelm, P. Alternative Natrium. *Nachr. Chem.* **2014**, *62*, 1163–1168, doi:10.1002/nadc.201490415.

113. Adelhelm, P.; Hartmann, P.; Bender, C.L.; Busche, M.; Eufinger, C.; Janek, J. From lithium to sodium: cell chemistry of room temperature sodium-air and sodium-sulfur batteries. *Beilstein J. Nanotechnol.* **2015**, *6*, 1016–1055, doi:10.3762/bjnano.6.105.

114. Shan, S.; Yang, L.-P.; Liu, X.; Wei, X.; Yang, H.; Shen, X. Preparation and characterization of TiO2 doped and MgO stabilized Na–β″-Al2O3 electrolyte via a citrate sol–gel method. *Journal of Alloys and Compounds* **2013**, *563*, 176–179, doi:10.1016/j.jallcom.2013.02.092.

115. Shi, J.; Hong, Y.; Zhu, C. Effect of Chromium on Electrochemical and Mechanical Properties of Beta-Al2O3 Solid Electrolyte Synthesized Via a Citrate-Nitrate Combustion Method. *Crystals* **2020**, *10*, 987, doi:10.3390/cryst10110987.

116. Zhu, C.; Hong, Y.; Huang, P. Synthesis and characterization of NiO doped beta-Al 2 O 3 solid electrolyte. *Journal of Alloys and Compounds* **2016**, *688*, 746–751, doi:10.1016/j.jallcom.2016.07.264.

117. Erkalfa, H.; Misirli, Z.; Baykara, T. The effect of TiO2 and MnO2 on densification and microstructural development of alumina. *Ceramics International* **1998**, *24*, 81–90, doi:10.1016/S0272-8842(97)00082-5.

118. Lu, X.; Li, G.; Kim, J.Y.; Meinhardt, K.D.; Sprenkle, V.L. Enhanced sintering of β″-Al2O3/YSZ with the sintering aids of TiO2 and MnO2. *J. Power Sources* **2015**, *295*, 167–174, doi:10.1016/j.jpowsour.2015.06.147.

119. Zhao, K.; Liu, Y.; Zeng, S.M.; Yang, J.H.; Liu, Y.W.; Zhan, Z.L.; Song, L. Preparation and characterization of a ZrO 2 –TiO 2 -co-doped Na-β″-Al 2 O 3 ceramic thin film. *Ceramics International* **2016**, *42*, 8990–8996, doi:10.1016/j.ceramint.2016.02.091.

120. Yi, E.; Temeche, E.; Laine, R.M. Superionically conducting β″-Al 2 O 3 thin films processed using flame synthesized nanopowders. *J. Mater. Chem. A* **2018**, *6*, 12411–12419, doi:10.1039/c8ta02907e.

121. Chen, G.; Lu, J.; Li, L.; Chen, L.; Jiang, X. Microstructure control and properties of β″-Al2O3 solid electrolyte. *Journal of Alloys and Compounds* **2016**, *673*, 295–301, doi:10.1016/j.jallcom.2016.03.009.

122. Wu, J.; Shi, J.; Hong, Y.; Zhu, C. Effect of Chromium on electrochemical and mechanical properties of beta-Al 2 O 3 solid electrolyte. *Mater. Res. Express* **2020**, *7*, 105502, doi:10.1088/2053-1591/abafd0.

123. Kennedy, J.H.; Akridge, J.R.; Kleitz, M. Complex plane analysis of the impedance and admittance of polycrystalline sodium-β-alumina doped with transition metal ions. *Electrochim. Acta* **1979**, *24*, 781–787, doi:10.1016/0013-4686(79)80009-2.

124. Lee, S.-T.; Lee, D.-H.; Kim, J.-S.; Lim, S.-K. Influence of Fe and Ti addition on properties of Na+-β/β″-alumina solid electrolytes. *Met. Mater. Int.* **2017**, *23*, 246–253, doi:10.1007/s12540-017-6120-3.

125. Butts, D.; Schoiber, J.; Choi, C.; Redhammer, G.J.; Hüsing, N.; Donne, S.; Dunn, B. Fe-Substituted Sodium β″-Al 2 O 3 as a High-Rate Na-Ion Electrode. *Chem. Mater.* **2021**, *33*, 6136–6145, doi:10.1021/acs.chemmater.1c01680.

126. Moghadam, H.H.; Paydar, M.H. The Effect of Nano CuO as Sintering Aid on Phase Formation, Microstructure and Properties of Li2O-Stabilized b″-Alumina Ceramics. *J. Ceram. Sci. Tech.* **2016**, 441–446.

127. Javadi-Doodran, T. Microstructure and conductivity of the sodium nickel chloride (zebra) battery cathode; McMaster University, Hamilton, Ontario, Canada, 2012.

128. Ahn, C.-W.; Kim, M.; Hahn, B.-D.; Hong, I.; Kim, W.; Moon, G.; Lee, H.; Jung, K.; Park, Y.-C.; Choi, J.-H. Microstructure design of metal composite for active material in sodium nickel-iron chloride battery. *Journal of Power Sources* **2016**, *329*, 50–56, doi:10.1016/j.jpowsour.2016.08.068.

129. Adendorff, K.T. The Crystal Chemistry of the Na∕FeCl2 Battery. *J. Electrochem. Soc.* **1988**, *135*, 2121, doi:10.1149/1.2096226.

130. Coetzer, J.; Wald, G.D.; Orchard, S.W. Mechanism of the cathode reaction in sodium-ferrous chloride secondary cells. *J Appl Electrochem* **1993**, *23*, 790–800, doi:10.1007/BF00249951.

131. Li, G.; Lu, X.; Kim, J.Y.; Viswanathan, V.V.; Meinhardt, K.D.; Engelhard, M.H.; Sprenkle, V.L. An Advanced Na–FeCl2 ZEBRA Battery for Stationary Energy Storage Application. *Adv. Energy Mater* **2015**, *5*, 1500357, doi:10.1002/aenm.201500357.

132. Li, G.; Lu, X.; Kim, J.Y.; Engelhard, M.H.; Lemmon, J.P.; Sprenkle, V.L. The role of FeS in initial activation and performance degradation of Na–NiCl2 batteries. *J. Power Sources* **2014**, *272*, 398–403, doi:10.1016/j.jpowsour.2014.08.106.

133. Galloway, R.C.; Haslam, S. The ZEBRA electric vehicle battery: power and energy improvements. *Journal of Power Sources* **1999**, 164–170, doi:10.1016/S0378-7753(98)00259-6.

134. Prakash, J. Effect of chemical additives on the performance of Na/NiCl2 cells. *Ionics* **2000**, *6*, 210–217, doi:10.1007/BF02374068.

135. Prakash, J.; Redey, L.; Vissers, D.R.; DeGruson, J. Effect of sodium iodide additive on the electrochemical performance of sodium/nickel chloride cells. *J Appl Electrochem* **2000**, *30*, 1229–1233.

136. Chang, H.-J.; Lu, X.; Bonnett, J.F.; Canfield, N.L.; Han, K.; Engelhard, M.H.; Jung, K.; Sprenkle, V.L.; Li, G. Decorating β″-alumina solid-state electrolytes with micron Pb spherical particles for improving Na wettability at lower temperatures. *J. Mater. Chem. A* **2018**, *6*, 19703–19711, doi:10.1039/C8TA06745G.

137. Ahlbrecht, K.; Bucharsky, C.; Holzapfel, M.; Tübke, J.; Hoffmann, M.J. Investigation of the wetting behavior of Na and Na alloys on uncoated and coated Na-β-alumina at temperatures below 150°C. *Ionics* **2017**, *23*, 1319–1327, doi:10.1007/s11581-017-2017-x.

138. Hu, Y.; Wen, Z.; Wu, X. Porous iron oxide coating on β″-alumina ceramics for Na-based batteries. *Solid State Ionics 19 Proceedings of the 19th International Conference on Solid State Ionics* **2014**, *262*, 133–137, doi:10.1016/j.ssi.2013.08.033.

139. Wen, Z.; Hu, Y.; Wu, X.W.; Han, J.; Gu, Z. Main Challenges for High Performance NAS Battery: Materials and Interfaces. *Adv. Funct. Mater.* **2012**, doi:10.1002/adfm.201200473.

140. Danzer, R.; Supancic, P.; Pascual, J.; Lube, T. Fracture statistics of ceramics – Weibull statistics and deviations from Weibull statistics. *Engineering Fracture Mechanics* **2007**, *74*, 2919–2932, doi:10.1016/j.engfracmech.2006.05.028.

141. Lin, J.; Wen, Z.; Wang, X.; Song, S.; Liu, Y. Mechanochemical synthesis of Na-β/β″-Al_2O_3. *J Solid State Electrochem* **2010**, *14*, 1821–1827.

142. Doerffel, D.; Sharkh, S.A. A critical review of using the Peukert equation for determining the remaining capacity of lead-acid and lithium-ion batteries. *Journal of Power Sources* **2006**, *155*, 395–400, doi:10.1016/j.jpowsour.2005.04.030.

143. Hoppe, A.; Dirksen, C.; Skadell, K.; Stelter, M.; Schulz, M.; Carstens, S.; Enke, D.; Koppka, S. Sodium Solid Electrolytes: NaxAlOy Bilayer-System Based on Macroporous Bulk Material and Dense Thin-Film. *Materials (Basel)* **2021**, *14*, doi:10.3390/ma14040854.

144. Duncan, G. Polytypism in the β-aluminas. *Proceedings of the 15th International Conference on Solid State Ionics* **1989**, *36*, 109–112, doi:10.1016/0167-2738(89)90068-4.

145. Tel'nova, G.B.; Solntsev, K.A. Structure and ionic conductivity of a beta-alumina-based solid electrolyte prepared from sodium polyaluminate nanopowders. *Inorg Mater* **2015**, *51*, 257–266, doi:10.1134/S0020168515030176.

146. Shannon, R.D. Revised effective ionic radii and systematic studies of interatomic distances in halides and chalcogenides. *Acta Cryst A* **1976**, *32*, 751–767, doi:10.1107/S0567739476001551.

147. Holleman, A.F.; Wiberg, E.; Wiberg, N. *Lehrbuch der anorganischen Chemie*, 102., stark umgearb. u. verb; de Gruyter: Berlin, 2007, ISBN 9783110177701.

148. Morgan, P.E.D.; Koutsoutis, M.S. Phase Studies Concerning Sintering in Aluminas Doped with Ti4+. *Journal of the American Ceramic Society* **1985**, *68*, C-156-C-156, doi:10.1111/j.1151-2916.1985.tb15226.x.

149. Bay, M.-C.; Heinz, M.V.F.; Figi, R.; Schreiner, C.; Basso, D.; Zanon, N.; Vogt, U.F.; Battaglia, C. Impact of Liquid Phase Formation on Microstructure and Conductivity of Li-Stabilized Na-β″-alumina Ceramics. *ACS Appl. Energy Mater.* **2019**, *2*, 687–693, doi:10.1021/acsaem.8b01715.

150. Kleebe, H.-J.; Pezzotti, G.; Ziegler, G. Microstructure and Fracture Toughness of Si 3 N 4 Ceramics: Combined Roles of Grain Morphology and Secondary Phase Chemistry. *Journal of the American Ceramic Society* **1999**, *82*, 1857–1867, doi:10.1111/j.1151-2916.1999.tb02009.x.

151. Claussen, N. Fracture Toughness of Al2O3 with an Unstabilized ZrO2 Dispersed Phase. *Journal of the American Ceramic Society* **1976**, *59*, 49–51, doi:10.1111/j.1151-2916.1976.tb09386.x.

152. Lohbauer, U.; Petschelt, A.; Greil, P. Lifetime prediction of CAD/CAM dental ceramics. *J. Biomed. Mater. Res.* **2002**, *63*, 780–785, doi:10.1002/jbm.10468.

153. Thind, B.S.; Reddy, G.N.; Thomas, A.J.; Reddy, C.C. Modified Damage Equalization Method for Lifetime Estimation of Dielectrics. *IEEE Trans. Dielect. Electr. Insul.* **2021**, *28*, 1118–1126, doi:10.1109/TDEI.2021.009403.

154. Heinz, M.V.; Bay, M.-C.; Vogt, U.F.; Battaglia, C. Grain size effects on activation energy and conductivity: Na- β ″-alumina ceramics and ion conductors with highly resistive grain boundary phases. *Acta Materialia* **2021**, *213*, 116940, doi:10.1016/j.actamat.2021.116940.

155. Bay, M.-C.; Heinz, M.V.; Linte, C.; German, A.; Blugan, G.; Battaglia, C.; Vogt, U.F. Impact of sintering conditions and zirconia addition on flexural strength and ion conductivity of Na-β"-alumina ceramics. *Materials Today Communications* **2020**, *23*, 101118, doi:10.1016/j.mtcomm.2020.101118.

156. Miller, G.R.; Paquette, D.G. *Physical Properties Data Compilations Relevant to Energy Storage*: III. *Engineering Properties of Single and Polycrystalline Properties of Sodium Beta and Beta" -Alumina*. NSRDS 61 Part 3; U.S. Government Printing Office: Washington, 1979.

157. Kishimoto, A.; Shimokawa, K.; Jung, S.-J. Effect of sodium content on the mechanical and electrical properties of preferentially oriented Naβ-alumina ceramics. *J Mater Sci Lett* **2003**, *22*, 1083–1085, doi:10.1023/A:1024934807879.

158. Bracco, S.; Delfino, F.; Trucco, A.; Zin, S. Electrical storage systems based on Sodium/Nickel chloride batteries: A mathematical model for the cell electrical parameter evaluation validated on a real smart microgrid application. *J. Power Sources* **2018**, *399*, 372–382, doi:10.1016/j.jpowsour.2018.07.115.

159. Wang, S.; Pan, Z.; Zhao, J.; Huang, Q.; Shapiro, A.; Sarrafi-Nour, R.; Guillermo, Z. Study of Discharge Characteristics of Sodium/NiCl2 Cell Using Electrochemical Impedance Spectroscopy. *J. Electrochem. Soc* **2013**, *160*, A458-A463, doi:10.1149/2.041303jes.

160. Mulder, G.; Omar, N.; Pauwels, S.; Meeus, M.; Leemans, F.; Verbrugge, B.; Nijs, W. de; van den Bossche, P.; Six, D.; van Mierlo, J. Comparison of commercial battery cells in relation to material properties. *Advances in electrochemical materialsience and manufactoring. Selection of papers from the 13th ISE Topical Meeting, Pretoria, South Africa* **2013**, *87*, 473–488, doi:10.1016/j.electacta.2012.09.042.

161. Cooper, S.J.; Bertei, A.; Finegan, D.P.; Brandon, N.P. Simulated impedance of diffusion in porous media. *Electrochimica Acta* **2017**, *251*, 681–689, doi:10.1016/j.electacta.2017.07.152.

162. Cai, J.; Wei, W.; Hu, X.; Wood, D.A. Electrical conductivity models in saturated porous media: A review. *Earth-Science Reviews* **2017**, *171*, 419–433, doi:10.1016/j.earscirev.2017.06.013.

163. Stackpole, M.F.; MacLachlan, S. Corrosion resistant materials for sodium-sulphur cells. In *Power sources 12*: *Research and development in non-mechanical electrical power sources* Proceedings of the 16th International Power Sources Symposium held at Bornemouth, September 1988; Keily, T., Baxter, B.W., Eds.; Taylor & Francis: Great Britain, 1989, ISBN 0951232010.

164. Zhang, Y.; Chen, Y.; Zhou, J.; Sun, D.; Li, H. Laser welding-brazing of alumina to 304 stainless steel with an Ag-based filler material. *Metall. Res. Technol.* **2021**, *118*, 104, doi:10.1051/metal/2020086.

165. Heo, H.; Kim, G.; Park, Y.-C.; Jung, K.; Kang, C.-Y. Effect of Bonding Temperature on Crack Occurrences in Al2O3/SS 430 Joints Using Cu-Based Brazing Alloys. *Metals* **2018**, *8*, 752, doi:10.3390/met8100752.

166. Heo, H.; Joung, H.; Jung, K.; Kang, C.-Y. Formation of Interfacial Reaction Layers in Al2O3/SS 430 Brazed Joints Using Cu-7Al-3.5Zr Alloys. *Metals* **2018**, *8*, 990, doi:10.3390/met8120990.

12.   Selbstständigkeitserklärung

Ich erkläre hiermit, dass ich die vorliegende Dissertation selbstständig und unter Verwendung der angegebenen Hilfsmittel, persönlichen Mittelungen und Quellen verfasst habe.

Jena, den

_____

Cornelius L. Dirksen

13.   Liste von wissenschaftlichen Beiträgen

Publikationen

C. L. Dirksen, K. Skadell, M. Schulz, M. Stelter, Effects of TiO_2 doping on Li^+-stabilized Na-β″-alumina for energy storage applications. Separation and Purification Technology 213 (**2019**) 88.

A.I. Agustina, K. Skadell, C. L. Dirksen, M. Schulz, S. P. Kusumocahyo, Sol-gel method for synthesis of Li^+-stabilized Na-β″-alumina for solid electrolytes in sodium-based batteries, AIP Conference Proceedings 2175 (**2019**) 02007-01.

L. Medenbach, P. Hartmann, J. Janek, T. Stettner, A. Balducci, C. Dirksen, M. Schulz, M. Stelter, P. Adelhelm, A sodium polysulfide battery with liquid/solid electrolyte: Improving sulfur utilization using P_2S_5 as additive and tetramethylurea as catholyte solvent, Energy Technology 8 (**2020**) 1901200.

A. Hoppe, C. Dirksen, K. Skadell, M. Stelter, M. Schulz, S. Carstens, D. Enke, S. Koppka, Sodium Solid Electrolytes: Na_xAlO_y Bilayer-System Based on Macroporous Bulk Material and Dense Thin-Film. Materials 14 (**2021**) 848.

M. P. Fertig, K. Skadell, M. Schulz, C. Dirksen, P. Adelhelm, M. Stelter, From High- to Low-Temperature: The Revival of Sodium-Beta Alumina for Sodium Solid- State Batteries. Batteries and Supercaps 5 (**2021**) e202100131.

C. L. Dirksen, K. Skadell, M. Schulz, M. P. Fertig, M. Stelter, Influence of 3d transition metal doping on lithium stabilized Na- β″-alumina solid electrolytes. Materials 14 (**2021**) 5389.

M. P. Fertig, C. Dirksen, M. Schulz, M. Stelter, Humidity-Induced Degradation of Lithium-Stabilized Sodium-Beta Alumina Solid Electrolytes. Batteries. 8 (**2022**) 103.

Vorträge

<u>C. L. Dirksen</u>, M. Schulz, M. Stelter, Effects of TiO_2 doping on Li^+-stabilized Na-β″-alumina for energy storage applications, ICIM **2018**, Dresden.

<u>C. Dirksen</u>, A. Hoppe, K. Skadell, S. Koppka, M. Stelter, M. Schulz, D. Enke, Sodium Solid Electrolytes: Na_xAlO_y Bilayer-System of Macroporous Bulk Material and Dense Thin-Film, Cellmat **2020**, Erlangen (online).

<u>C. Dirksen</u>, M. Schulz, M. Fertig, K. Skadell, M. Stelter, Na-β″-alumina – exploring the next steps for the most applied solid electrolyte, Electrochemistry **2022**, Berlin

Posterbeiträge

<u>C. L. Dirksen</u>, M. Schulz, M. Stelter, Effects of TiO_2 doping on Li^+-stabilized Na-β″-alumina for energy storage applications, ICIM **2018**, Dresden.

<u>C. Dirksen</u>, A. I. Agustina, M. Schulz, M. Stelter, Characterization of Mn-doped Li^+-stabilized Na-β″-alumina electrolytes, Electrochemistry **2018**, Ulm.

<u>C. Dirksen</u>, A. I. Agustina, M. Schulz, M. Stelter, Characterization of transition metal doped Li^+-stabilized Na-β″-alumina solid electrolytes, Bunsentagung **2019**, Jena.

<u>C. Dirksen</u>, K. Skadell, M. Schulz, M. Stelter, Na-β″-alumina – The next steps for the most applied solid electrolyte, 2nd International Sodium Battery Symposium **2021**, Dresden.

Patent

<u>C. Dirksen</u>, M. Schulz, R. Weidl, J. Rösler, Herstellung von Grünkörpern aus Na-β-aluminat; Manufacture of green compacts from Na-β-alumina. DE-Patentnummer: DE 102019129869, PCT-Patentnummer: WO 2021089481. (noch nicht erteilt)